AN ABSTRACT OF THE DISSERTATION OF

Rebecca R. Grollman for the degree of Doctor of Philosophy in Physics presented on June 13, 2017.

Title: Photophysics of Organic Semiconductors at the Nanoscale

Abstract approved: _____

Oksana Ostroverkhova

Organic semiconductors are used in a wide variety of applications including transistors, solar cells, and light emitting diodes. These materials are solution-processable, low cost, and tunable. Many successful organic optoelectronic materials utilize blends of several types of molecules (such as donors and acceptors) in order to promote charge generation. As blends are an inherently heterogeneous system, nanoscale morphology plays a critical role to determine the optoelectronic properties of the blend. The work presented in this dissertation aims to develop novel methods of probing the local nanoenvironment in organic semiconductors as well as establish the relations between the nanoscale environment of the molecules and their photophysics.

First, several experiments were performed via single molecule fluorescence microscopy to study energy transfer (FRET) and photo-oxidation in blends contain-

ing donor and acceptor molecules. Donor molecules were imaged with increasing acceptor molecule concentration to determine the change in their photophysical properties due to acceptor-modified morphology and donor-acceptor energy transfer. As the concentration of acceptor molecules reaches a critical concentration such that the average donor-acceptor distance is below the FRET radius, fluorescence of donor molecules is quenched. This enables single-molecule-level microscopy at relatively high donor concentrations, thus creating a new super-resolution tool to image donor molecules in a modified local environment. As the concentration of acceptors increased, the number of photons a donor emits over its lifetime decreased, and fluorescence intermittency increased. These observations were quantified using statistical analysis and complementary cumulative distribution functions. The findings were attributed to the acceptor-modified morphology which reduced the donor molecule protection from photo-oxidation reactions; however, the presence of the acceptors also enhanced the reversibility of the photo-oxidation process by quenching the highly reactive singlet oxygen. Such reversibility is important for organic semiconductors as their photodegradation is one of the key drawbacks for applications.

Next, molecular packing and photostability changes are presented as a function of different host matrices and different molecular side groups, again via single molecule fluorescence spectroscopy. Molecules embedded in a crystalline organic semiconductor host matrix exhibited higher photostability than a polymer matrix. In addition, larger side groups lead to higher photostability, indicating the larger side groups provide better protection from reactions with oxygen. Orienta-

tional constraints for guest molecules in a crystalline host were also observed and quantified.

Lastly, a novel method to study photoinduced charge transfer between organic semiconductors utilizing optical tweezers is presented. A silica microsphere is coated with an organic semiconductor (e.g. donor) film and suspended in a liquid with varying dielectric permittivity and containing other organic semiconductor molecules (e.g. acceptors). The time-resolved surface charge of this sphere is measured by trapping the sphere using optical tweezers and applying a sinusoidal electric field across the sphere. (Dis)charging dynamics are measurable by photoexciting the coating of the sphere and observing the dynamics of excitons by monitoring the photoluminescence of the trapped sphere while simultaneously measuring surface charge with optical tweezers.

Photophysics of Organic Semiconductors at the Nanoscale

by

Rebecca R. Grollman

A DISSERTATION

submitted to

Oregon State University

in partial fulfillment of
the requirements for the
degree of

Doctor of Philosophy

Presented June 13, 2017
Commencement June 2017

Doctor of Philosophy dissertation of Rebecca R. Grollman presented on June 13, 2017.

APPROVED:

Major Professor, representing Physics

Chair of the Department of Physics

Dean of the Graduate School

I understand that my dissertation will become part of the permanent collection of Oregon State University libraries. My signature below authorizes release of my dissertation to any reader upon request.

Rebecca R. Grollman, Author

ACKNOWLEDGEMENTS

First of all, I would like to thank my advisor, Dr. Oksana Ostroverkhova, for all of her support and guidance. Her enthusiasm is contagious and drives me to be a better scientist. I would also like to thank my other committee members, Dr. David McIntyre, Dr. Guenter Schneider, Dr. Bo Sun, and Dr. David Hamby, for their constructive feedback and advice.

I would like to thank my lab members, both past and present, for their help with experimental work and making the lab a fun place to be. In particular, I would like to thank Dr. Brian Johnson and Dr. Keshab Paudel for their help around the lab and conversations. Kati Bilty Bartlein and Alex Robertson were great partners in learning the ropes for single molecule experiments (especially learning how to focus a microscope on nothing). Kyle Peters, Jake Busche, Graham Founds, and Rick Wallace not only made fantastic sample holders, but also asked great questions and helped with the optical tweezers chapter. The new generation of lab members, Nicole Quist, Novela Auparay, and Robert Harrison, have continued to make working in this lab a joy. Other graduate students including Dr. Emily Smith, Dr. Andrew Stickel, and Dr. Zack Thompson provided needed motivational speeches and support.

In addition to the physics department, the music department has been another home. I would like to thank Dr. Jill Pauls, Dr. Chris Chapman, and Dr. Marlan Carlson for welcoming me in to the Wind Ensemble and Corvallis-OSU

Symphony Orchestra. Continuing to play the flute while working on my dissertation was essential to my sanity. I would like to thank my fellow blutes, especially Grace D'Angelo, Sage Gustafson, Claire McMorris, and Rachel Soo Hoo for their encouragement and providing stress relief in the form of flute duets and quintets.

I would like to thank Grace Foster for being a great friend and encouraging listener. Her motivational cheers were important while doing homework and performing experiments. I would like to thank Chris Reidy for being a great partner for studying for the comprehensive exam all summer through preparing for my final defense. In addition to our physics discussions and coffee adventures, his support, understanding, encouragement, and popcorn have made all the difference. Lastly, I would like to thank my parents, Marsha and Jonathan. Their support and encouragement has been essential in getting here today.

TABLE OF CONTENTS

TABLE OF CONTENTS (Continued)

TABLE OF CONTENTS (Continued)

TABLE OF CONTENTS (Continued)

LIST OF FIGURES

LIST OF FIGURES (Continued)

Figure Page

LIST OF FIGURES (Continued)

LIST OF FIGURES (Continued)

LIST OF FIGURES (Continued)

LIST OF FIGURES (Continued)

LIST OF TABLES

LIST OF TABLES (Continued)

Chapter 1 Introduction

1.1 Introduction to Organic Semiconductors

While organic semiconductors were first discovered in 1910 with anthacene crystals,[9] it was not until electroluminescence was discovered in the 1960s[10] that they were considered for devices. Up until then, inorganic semicondutors, including silicon and germanium, were replacing vacuum tubes in solid state devices.[9] At first, organic semiconductor current densities were too low, not enough light was produced, and stability was too poor for devices.[9] The improvement of synthesis and controlled doping in the 1970s[11] improved these materials for devices. Over the past decade, the development of material design, fabrication, and processing have led to a better understanding of change transport and more efficient devices.[12] Mobilities in organic transistors alone have improved by two orders of magnitude in the past ten years.[12,13]

Today, organic semiconductors (both low molecular weight, or small molecule, and polymers) are used in a wide variety of applications ranging from transistors (both thin film and field effect) to photovoltaics (OPVs) to light emitting diodes (OLEDs).[9] There are many benefits to organics including their low cost, flexibility, and tunable properties. They are also solution processable.[12] Applications that

rely on charge carrier photogeneration, such as solar cells, utilize composites (or blends) to improve charge carrier mobilities and reduce trap densities. These blends are composed of donor (D) and acceptor (A) molecules that can transfer photoinduced electrons from D to A at the junction.[14]

The local nanoenvironment affects charge and energy transfer in devices. In blends, the addition of another material makes the local nanoenvironment more complicated. The packing of materials and dielectric properties of the environment also affects the processes and efficiency of charge transfer. Typically, these properties are averaged when studied at the macroscopic level. While averaging these properties helps to characterize these films, in reality, they are heterogeneous. The ability to study the local nanoenvironment is then crucial to understand the characteristics of the entire film. Studying these materials at the nanoscale enables a better understanding of the heterogeneity of the local nanoenvironment and how this heterogeneity affects the properties important for devices.

The focus of this dissertation will be on the properties of small molecule organic semiconductors studied from the microscopic level to the single molecule level. Specifically, I investigate the interaction between D and A materials through single molecule fluorescence spectroscopy and novel optical tweezer techniques. By understanding the basic physics behind these processes, I aim to contribute to the expanding knowledge of these materials such that they can be used in efficient and innovative devices in the future.

This introduction will first discuss properties important to organic semiconduc-

tors and devices. Then, experimental techniques used throughout this dissertation will be introduced including single molecule fluorescence spectroscopy and optical tweezers.

1.2 Optical and Electronic Properties

Optical and electronic properties are important for deciding how organic semiconductors can be utilized in a variety of applications and devices. For example, light absorption is an important feature for solar cells while emission is important for OLEDs. Charge photogeneration is important for solar cells while charge transport is important for all devices.

Many of these properties are dependent on molecular packing, molecular structure, morphology at interfaces, material defect, applied electric field, and temperature. All of these properties will be discussed below briefly, but more in depth discussions of particular properties will be addressed in each of the following chapters. Chapter 2 focuses on morphology at D/A interfaces, Chapter 3 studies molecular packing, and Chapter 4 describes a technique to study applied electric field and D/A blends.

1.2.1 Absorption and Photoluminescence

Understanding absorption and photoluminescence (PL) are important for both building devices and experimental decisions made in the next few chapters. Fluorescence and phosphorescence are types of luminescence, which describes the emission of light from a substance. Fluorescence has a lifetime ∼10 ns where a photon is emitted during the transition from the first excited state (S_1) to the ground state (S_0). Phosphorescence describes the transition from the triplet state (T_1) to S_0. Since this is a forbidden transition, the lifetime is much slower than fluorescence (on the order of microseconds to seconds).[15] The absorption and PL of solids is similar for gas and solution of the same material, but as the material gets more ordered (ie transitions from gas to solid), the PL becomes red shifted. Absorption and PL allow us to resolve intramolecular vibrations at room temperature.[9]

Jablonski diagrams can be used to illustrate the absorption and emission of light by indicating transitions between different energy levels. It is clear to see that the energy of emitted light is always less than the energy of absorbed light.[15] The maximum absorption or PL provides a good estimate for the energy between the highest occupied molecular orbital (HOMO) and lowest unoccupied molecular orbital (LUMO) levels. To get a more exact measurement, HOMO and LUMO levels are measured with differential pulse voltammetry or cyclic voltammetry.[14,16,17]

One of the advantages of organic semiconductors are that their optical properties are tunable. By changing the end groups of a particular molecular backbone,

absorption and PL can be tuned. By making the molecule longer, the optical properties become red-shifted.

1.2.2 Charge Carrier Photogeneration

Charge carrier photogeneration is important for many optoelectronic applications, especially for solar cells. Understanding the conditions needed to generate mobile charge carriers is crucial to building new devices and improving their efficiency. Some methods for charge carrier photogeneration include band-to-band excitation or separating a bound exciton (electron-hole pair) that has been created. The binding energy between two charges is the Coloumb potential V

$$V = \frac{e^2}{4\pi\epsilon_0\epsilon r} \tag{1.1}$$

where e is the charge of an electron, ϵ_0 is the dielectric permittivity of vacuum, ϵ is the dielectric constant of the organic medium, and r is the distance between the electron and hole. This binding energy must be overcome to create mobile charge carriers.[12]

There are many ways to overcome the exciton binding energy. For example, an electric field can be applied for exciton dissociation. Donor (D) and acceptor (A) materials can be combined to create a D/A heterojunction. This boundary creates a driving force from the energy offset between the two materials. As photons

are absorbed by one material, they create an exciton, which diffuses to the D/A interface where the exciton can dissociate. With this method, morphology of the donor and acceptor domains and interfaces are important as well as the molecular structures of each material.[12]

1.2.3 Charge Transport in Organic Semiconductors

All devices rely on charge transport and a material's ability to conduct charges. Charge carrier mobility quantifies a material's ability to conduct charge. A material's mobility is dependent on many factors including molecular packing, molecular structure, material defects and concentration, applied electric field strength, and temperature.[12] There are two types of charge carrier transport mechanisms: band and hopping transport. Band transport occurs in highly purified molecular crystals leading to high charge carrier mobilites μ of $\sim 1 - 10\ cm^2/(Vs)$ while hopping transport occurs in amorphous organic solids leading to mobilities μ of $\sim 10^{-3}\ cm^2/(Vs)$. Many methods are used to increase charge carrier densities including electro-chemical doping, carrier injection from contacts, photogeneration of carriers, and field-effect doping.[9]

1.3 Single Molecule Overview

Single molecule fluorescence spectroscopy (SMFS) is used to study the behavior of individual molecules and look beyond the ensemble average. SMFS probes a population of well-spaced (ie greater than the diffraction limit) molecules with a high signal to noise ratio (SNR). SMFS allows the study of nanoscale molecular behavior and its nanoscale environment.[1]

By looking beyond the ensemble average, the distribution of parameters can be determined for a population of molecules.[18] This representation is advantageous since all molecules are not identical. Each single molecule serves as a local reporter of its nanoenvironment, which can be influenced by functional groups, atoms, ions, electrostatic charges,[1] polarity, and viscosity.[12,19–21] Looking at individual molecules also allows one to study a particular conformation of a molecule at a given time[22] or study many molecules going through a time-dependent process without the need to synchronize all molecules to take the measurement. It is also possible to measure rare intermediate states, orientation of a molecular transition dipole, and study molecules at the nanoscale.[1]

SMFS began in 1989 with Kador and Moerner detecting the absorption signal of a dye molecule.[23] Orrit and Bernard then followed in 1990 with fluorescence excitation, which produced a better signal to noise ratio.[24] Betzig performed single molecule microscopy at room temperature in 1993.[22,25] In 2014, Betzig, Hell, and Moerner were awarded the Nobel Prize in Chemistry "for the development of

super-resolved fluorescence microscopy" and in particular for developing stimulated emission depletion (STED) microscopy and for single-molecule microscopy.[26]

Some applications of SMFS include using fluorescent molecules as labels for tracking to help understand different biological and physical processes. SMFS can determine the polarization of single molecules, orientation of molecular transition dipoles, and conformational changes of biological molecules via Förster Resonance Energy Transfer (FRET). Fluorescence lifetime measurements can also be extracted by probing a sample with short pulses from a modelocked laser where only one molecule is pumped at a time. It is then possible to measure the time delays between the pumped photon and emitted photon to get an excited state lifetime.[1]

There are important requirements for detection of a single molecule. First of all, the molecules need to be efficient fluorophores having a large absorption cross section and quantum yield.[18] Molecules must be stable where photobleaching quantum yields are small ($\Phi_B < 10^{-6}$) and a high number of photons are emitted over a molecule's lifetime (or duration of data collection) where $N_{tot} > 10^6$ photons.[12] These requirements restrict the number of guest-host samples that can be studied via SMFS.[18] Therefore, it is exciting to use SMFS as a tool for a particular set of organic semiconductors at this level.

Chapter 2 explores how the nanoscale environment of blends changes the photophysics of organic semiconductor materials using SMFS. Blends are important for devices when extracting mobile charge carriers, and SMFS allows us to study the

heterogeneity of these blends at the nanoscale. In this particular study, the change in the local environment is studied from the added acceptor molecules as well as the change in distributions of photophysical parameters of the donor molecules. Chapter 3 investigates how the host matrix and side groups of molecules affects the orientation and photostability of molecules in a film. Again, these properties are important for creating more reliable and efficient devices.

1.4 Optical Tweezers Overview

Described over twenty years ago as "the 'tractor beams' of today's technology,"[27] optical tweezers are instruments that use a highly focused laser beam to optically trap micron-sized particles or trap and cool atoms.[28] Optical tweezers have been utilized in many applications including biology, chemistry, engineering, and physics.[29]

Recently, an optical tweezer-based technique that enabled measurement of a surface charge density of microscopic particles suspended in non-polar liquids was reported, and resolution of a single electron charge e was demonstrated.[30] Further development of this technique led to measurements of single (dis)charging events on a 1 μm PMMA sphere in the same non-polar liquid (dodecane).[31]

Experiments measuring the surface charge of microspheres in polar solutions (dionized water) have also been reported. Pesce, et al. demonstrated the surface charge polystyrene spheres in water could be measured two different ways. One

method applied a step-wise electric field (DC) across the trapped sphere while the other method applied a sinusoidal electric field (AC). They found the method using an AC electric field was much more accurate (within 3%) while the DC method was less reliable (within 30%). Once charge of these spheres was determined, they were used as probes to study local electric fields from arbitrary electrode geometries.[32] They took this method one step further to determine electrophoretic and dielectrophoretic forces, which are useful in biology and medicine applications for positioning cells to study.[33]

I have extended these measurement techniques to trap and measure the surface charge of silica microspheres, coated with organic semiconductor material. These spheres are suspended in water. Using this technique, I have developed a novel method to study the (dis)charging of organic semiconductor molecules in various environments and under different applied electric fields with simultaneous photoexcitation. These charging events are also monitored by PL detection.

This method is novel for both optical tweezers and studying (dis)charging of organic semiconductor molecules. These charge measurements have never been performed on spheres coated with organic semiconductor molecules and charge measurements are typically performed in non-polar environments (and rarely in water). For organic semiconductors, this method provides a non-contact technique to measure (dis)charging dynamics as well. The development of this technique will be the focus of Chapter 4.

Chapter 2 Single Molecule Spectroscopy: Energy Transfer and Photo-oxidation in Blends

2.1 Introduction

2.1.1 Basic Principles of Single Molecule Spectroscopy

To probe a single molecule, the molecule is excited with a light source (usually a laser) at a resonant wavelength to get electronic transitions. Absorption is then detected directly or through fluorescence excitation. Here, single molecule fluorescence spectroscopy (SMFS) will be utilized. There are two requirements for SMFS. The first is that only one molecule can be in resonance in the volume probed by the laser. In other words, if more than one molecule is within a diffraction limited spot, only one molecule can be probed by the laser at a time. Secondly, there must be a high SNR. In order to fulfill the first requirement, the molecules need to be in a very clean host matrix at very low concentrations ($\sim 10^{-10}$ M). A large absorption cross section, high photostability (indicated by a large N_{tot} on the order of $\sim 10^6$ photons), and having as few molecules in triplet states as possible lead to a higher SNR.[1]

A single molecule is probed when it is excited with light $h\nu$ where h is the Planck

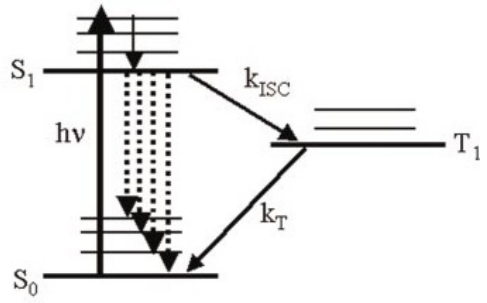

Figure 2.1: Jablonski energy level diagram for SMFS where S_0, S_1, and T_1 are the ground state, first excited state, and triplet state respectively. k_{ISC} and k_T are the intersystem crossing rate and the triplet decay rate. The molecule is pumped at $h\nu$. Figure from Ref. 1.

constant and ν is the optical frequency of excitation. The molecule absorbs the photon, creating an electron-hole pair. The electron can then relax from higher vibrational modes to the first excited singlet electronic state S_1. When the electron and hole recombine, the molecules emits a photon between the S_1 to S_0 (ground state) tranisition. Occasionally, some electrons transition to the triplet state T_1 as an intermediate step before transitioning back to the ground state (see Fig. 2.1). This process is known as intersystem crossing (ISC). During the relaxation step, there is a redshift between the absorption and emission bands due to an energy loss. This redshift is known as the Stokes shift. The probability that a single molecule absorbs a photon from the laser is proportional to $\frac{\sigma_p}{A}$ where σ_p is the effective absorption cross section of the molecule and A is the cross section of the laser beam.[1]

ISC can limit single molecule studies with saturation by creating a bottleneck

when emission and absorption stop because charges are stuck in the triplet state.[34] Photobleaching can also limit single molecule studies. Photobleaching is a photochemical process that causes molecules to stop absorbing or emitting photons at a particular excitation wavelength because the fluorophore oxidizes.[1] For example, when acenes oxidize, a new species is formed called an endoperoxide (EPO). In some cases, this photooxidation is reversible.[35] This interaction will be discussed in greater detail in Chapters 2 and 3.

In SMFS, the only signal that matters is the fluorescence from the molecule; other photons detected are considered part of the "background." Background signals come from residual fluorescence from optics or the laser. The sample also provides background signals from scattering off the sample itself and redshifted photons from other impurities. Noise is due to Poisson statistics of detected photons, or detector dark counts. Filters are used as a technique to lessen the background.[1] There are other techniques as well depending on the detection method used.

2.1.2 Types of Detection

There are two types of detectors for single molecule experiments: single-element detectors for a confocal microscope configuration and two-dimensional array detectors for a wide-field microscope configuration. The first single-element detectors were microchannel plate photomultiplier tubes (PMTs). For example, they have

been used to observe dyed single molecules in a laser focus.[36] PMTs have good temporal resolution, low dark current, and a large detection area. Unfortunately, PMTs have low quantum efficiencies for visible light and the electronics used with PMTs must have low noise levels.[1]

Another type of single-element detector is a single photon avalanche photodiode (SPAD). Both SPADs and PMTs have a low operating voltage and good temporal response. However, SPADs are better than PMTs because they have low dark counts and a much higher quantum efficiency. While SPADs have many advantages over PMTs, they are expensive. They also have a large "dead time" between counts, limiting their maximum count rate.[1]

A two-dimensional array uses a camera, such as a charge coupled device (CCD) detector array, to detect fluorescence. The human eye, if well adjusted to the dark, can also detect fluorescence through a microscope.[1] The following single molecule chapters use an electron multiplying CCD (EMCCD) to detect single molecules. While data collection is much faster (ie scanning is not needed over the entire sample), a longer integration time is needed to collect more photons and improve SNR.

2.1.3 Historical Experiments

Early experiments began in 1989 starting with the detection of the absorption signal of a single molecule. A year later, it was shown that it is possible to de-

tect fluorescence excitation of a single molecule. The first two single molecule experiments will be discussed in greater detail.

In 1989, W. E. Moerner and L. Kador published the first single molecule paper entitled "Optical Detection and Spectroscopy of Single Molecules in a Solid." They observed the optical absorption spectrum of single dopant molecules of pentacene in a p-Terphenyl host at liquid Helium temperatures of 1.6 K. They used samples with concentrations of 1×10^{-6} to 2×10^{-7} mol/mol with a thickness of 100 to 200 μm per sample. They were able to measure the statistical fine structure with laser frequency modulation spectroscopy on a frequency scale less than the modulating frequency. It was difficult to detect a signal from a single molecule due to Rayleigh scattering and Raman background signals from the host matrix. To overcome this noise, they used two methods of frequency modulation including the Stark double modulation (FMS) and ultrasound double modulation (FMUS).[23]

M. Orrit and J. Bernard published "Single Pentacene Molecules Detected by Fluorescence Excitation in a p-Terphenyl Crystal" a year after Moerner and Kador. Orrit and Bernard used fluorescence excitation to probe the same single molecules as Moerner and Kador for the first time by measuring the emitted intensity of a single molecule as a function of excitation frequency. In order to get the best signal, they used a large absorption cross section and the rate of emitted photons detected was also larger than the dark count of the detector.[24]

2.1.4 Motivation and Organization for this Chapter

As discussed in the introduction, blends are important for optoelectronic applications. As nanoscale morphology influences charge and energy transfer in devices, an important consideration for organic semiconductor blends is how the nanoscale morphology evolves as molecules of other types (such as acceptors) are added to the blend. To study the evolution of the formation of bulk heterojunctions (BHJs) or in BHJs with different compositions, we gradually add acceptor molecules to donor samples in a polymer host matrix (PMMA) and monitor changes in the photophysics of the donor molecules. SMFS is used to establish how the nanoscale environment in a polymer matrix evolves with addition of acceptor molecules and how the presence of acceptors influences interactions of the donor with oxygen. This interaction results in photodegredation and its reversal.

In the following chapter, materials and sample preparation will be discussed for both single molecule and supporting bulk experiments. Experimental setups will then be explained as well as data processing. Results from bulk and single molecule experiments will be presented as well as a discussion of results. Lastly, direction for future work will be discussed.

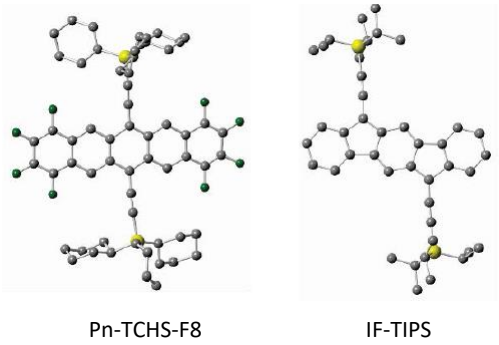

Figure 2.2: Molecular structures of Pn-TCHS-F8 and IF-TIPS.

2.2 Materials and Sample Preparation

We study a donor/acceptor (D/A) system at the single molecule level where Pn-TCHS-F8 acts as a donor with either PCBM or IF-TIPS as an acceptor as shown in Fig. 2.2. Both donor and acceptor molecules were incorporated in PMMA. These molecules were inspired by previous work done with these materials in organic donor-acceptor BHJ devices.[6,8]

The Pn-R-F8 derivatives in PMMA at ultra-low concentrations have been studied at the single molecule level using SMFS and shown to exhibit high fluorescence QY ($\sim 0.7-0.8$, depending on the side group R) and considerably higher photostability than the non-fluorinated functionalized Pn derivatives (such as Pn-TIPS).[3] As shown in the next chapter, the Pn derivatives with the bulkiest TCHS side group have demonstrated the highest photostability in air ($\Phi_B \sim 10^{-6}$, which is the probability of photobleaching upon absorption of a photon). This demonstrates

how these side groups play a protective role against reactions with oxygen. The protection also depends on the local nanoenvironment, and will be explored in this chapter.

The IF and PCBM derivatives have been chosen as acceptors because they have been used as acceptors and/or electron transporting materials in a wide variety of organic (opto)electronic devices due to their low LUMO energies (Fig. 2.3).[6,12,37–40] They also have very low fluorescence QYs due to efficient non-radiative emission. This allows for high concentrations of these molecules in PMMA without raising the fluorescence background at 633 nm excitation used in our experiments that efficiently excite Pn-TCHS-F8. The IF-TIPS acceptor was the main acceptor of choice. Detailed studies of samples with high PCBM concentrations were not carried out to minimize effects of Pn-fullerene reactions during the sample preparation.[41] Experiments were carried out at low PCBM concentrations and selected experiments at high concentrations revealed trends similar to those with IF-TIPS acceptors.

2.2.1 Single Molecule Sample Preparation

We looked at a variety of sample types at the single molecule level including (i) donor only (plain) samples of varying concentrations, (ii) single molecule donor samples with varying concentrations of added acceptor (4 to 20 nm average spacings), and (iii) average acceptor spacings of 5 nm with added donor molecules

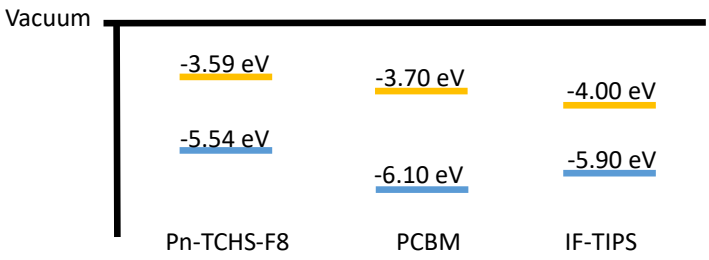

Figure 2.3: HOMO/LUMO energy levels of the donor (Pn-TCHS-F8) and acceptor (IF-TIPS and PCBM) molecules under study.

of varying concentrations (1x to 1000x) as illustrated in Fig. 2.4. All films were spin-cast, and all materials were guest molecules in a PMMA host matrix. The baseline concentration of the donor (Pn-TCHS-F8) was 3.44×10^{-10} M. All other donor concentrations were multiples of the original concentration. Average spacing between acceptor molecules R were calculated from

$$V = \frac{M}{N_A \rho_m f} \tag{2.1}$$

where V is the average volume per molecule, M is the molar mass of the host matrix (PMMA), N_A is Avogadro's number, ρ_m is the mass density of the host, and f is the molar fraction of guest to host. Assuming spherical molecules, the volume per molecule is $4\pi r^3/3$, and the average spacing between molecules R is $2r$.[7]

Samples for single molecule imaging were prepared in a 1% wt/wt solution of

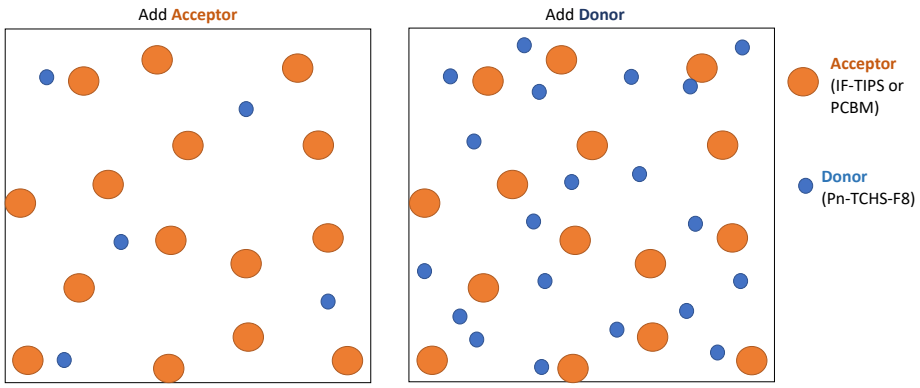

Figure 2.4: **Left:** Sample where acceptor concentration changes and donor concentration is fixed. **Right:** Sample where acceptor concentration is held constant, but donor concentration changes. Blue circles indicate donor molecules (Pn-TCHS-F8) while orange circles represent acceptor molecules (either IF-TIPS or PCBM.)

PMMA (75,000 m.w., Polysciences, Inc.) in toluene with a fluorophore (Pn-TCHS-F8) concentration of a multiple of 3.44×10^{-10} M. Acceptor (IF-TIPS or PCBM (nano-c [C60]PCBM)) were added to achieve different average spacings between molecules based on the molar fraction of the chosen acceptor and PMMA.

To minimize the presence of fluorescent contaminants, glass coverslips were soaked in a detergent and water solution overnight. They were then sonicated for 40 minutes in the detergent/water solution, rinsed thoroughly in deionized water, and dried under N_2. Cleanliness of coverslip, toluene, PMMA matrix, and chosen acceptor under the same experimental configuration used for single molecule imaging was insured before proceeding with spinning samples of interest. All films were spun at 3000 rpm for 50 seconds from 60 μL of solution.

2.2.2 Bulk Sample Preparation

Samples similar to the single molecule imaging films were prepared for bulk measurements but at higher Pn-TCHS-F8 concentrations.

Samples for FRET studies were prepared to achieve 3 and 7 nm spacing between a mixture of the guest molecules PCBM and Pn-TCHS-F8 while in PMMA. The molar fraction f was calculated for a guest and PMMA host where the guest was a mixture of equal parts PCBM and Pn-TCHS-F8. Three types of films were prepared per spacing: (i) Pn-TCHS-F8 only, (ii) PCBM only, and (iii) Pn-TCHS-F8/PCBM where the same number of molecules were added to ensure similar type sample morphology.

Samples for bulk photobleaching studies comprise of Pn-TCHS-F8 (donor) with an added acceptor (ADT-TES-F, PCBM, or IF-TIPS) spaced 5 nm apart in a PMMA host. As a control, a donor-only sample (Pn-TCHS-F8) was also made. The 5 nm spacings were calculated using Eq. 2.1. The concentration of Pn-TCHS-F8 in these sample increased to 3.0×10^{-4} M (compared to 3.44×10^{-10} M of single molecule experiments) such that the donor-to-acceptor molar ratio is 1.96.

For AFM measurements, five samples were prepared: i) PMMA only, ii) 10x Pn-TCHS-F8, iii) 100x Pn-TCHS-F8, and iv) and v) were the same as ii) and iii) with added IF-TIPS spaced 5 nm apart on average. The baseline Pn-TCHS-F8 concentrations are the same as for single molecule preparations.

2.3 Experimental Set-Up

Single molecule fluorescence imaging of Pn-TCHS-F8 molecules was performed under circularly polarized 633 nm wide-field illumination using an Olympus IX-71 inverted microscope with a 100x UPlanSApo (NA 1.4) oil objective and an Andor iXon EMCCD (DU-897) detector as shown in Fig. 2.5. The z633rdc and HQ645LP Chroma Tech filters were used for imaging. Collection efficiency was determined by

$$\eta_{coll} = \eta_Q T_{ang} T_{opt} T_{filt} \tag{2.2}$$

where η_Q is the quantum efficiency of the camera (85% in this case), T_{ang} is the angular collection factor, T_{opt} is the collection factor through the microscope optics (62.3%), and T_{filt} is the transmission through the dichroic and emission filter (59%).[3,42] For a single dipole emitter lying parallel to the surface of the cover slip, we estimated T_{ang} to be $\sim$ 34% using Ref. 43. These values give us an estimated collection efficiency of 10.6%.

2.4 Data Processing

Videos of tens of molecules imaged in a wide-field configuration are collected for 600 frames with an integration time of 0.1 seconds. When including camera settings, each frame is 0.16413 seconds. Videos are about 0.5 GB and stored by the Andor

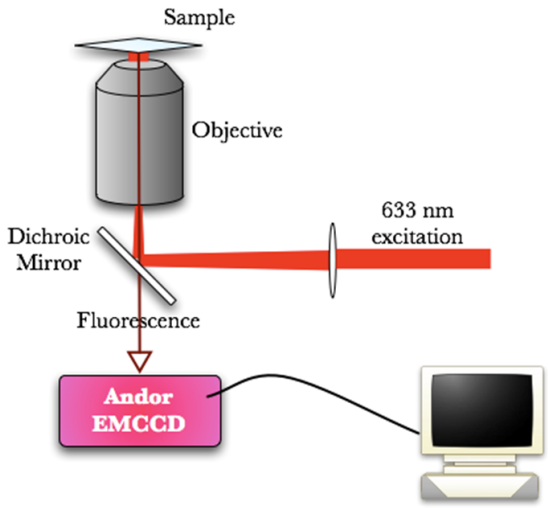

Figure 2.5: Schematic of single molecule experimental setup. The sample is excited by 633 nm light while it's fluorescence is collected by an EMCCD. From Ref. 2.

Solis software. In order to identify each individual fluorophore from the collected videos, the files are exported as raw data in an ASCII file and sent to a custom MATLAB script (SMAnalysisV2.m) to find potential fluorophores based on time traces extracted from the video. Typically, the user sets a background for the script to run such that about 200 fluorophores are found to ensure all molecules are identified. The user then chooses acceptable fluorophore time traces from the 200 found by MATLAB where an acceptable time trace is a digital, two level system as shown in Fig. 2.6. For more details on the custom MATLAB script, see Ref. 2.

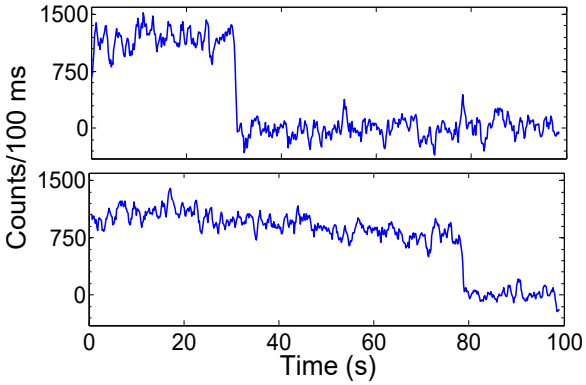

Figure 2.6: Single molecule fluorescence time traces obtained under a wide-field 633 nm excitation of Pn-TCHS-F8 in PMMA. The two traces above are examples of "non-blinker," a molecule that begins "on" and then transitions to "off" without turning back "on" for the duration of the video.[3]

.

2.4.1 N_{tot} Calculations

Photostability can be quantified by measuring the number of photons emitted over a fluorophore's lifetime, which is defined as N_{tot}. The total detected number of photons per fluorophore is calculated by integrating its time trace (with the background subtracted) over its lifetime. Histograms of the number of detected photons N were fit to a single-exponential function ($\sim \exp(-N/N_{tot,det})$) to find the mean number of detected photons $N_{tot,det}$. The number of emitted photons $N_{tot,em}$ is equivalent to

$$N_{tot,em} = \frac{N_{tot,det}}{\eta_{coll}} \tag{2.3}$$

where η_{coll} is the collection efficiency (Eq. 2.2).[3] A MATLAB script was written

to calculate $N_{tot,det}$ and from there, fits were done in Origin.[42]

2.4.2 Determining "on" and "off" times

Once fluorophore time traces are chosen for each data set, "on" and "off" times (the durations a molecule is in a bright and dark state respectively,) are extracted from each time trace. To separate "on" and "off" times, MATLAB is used to estimate an initial count threshold. This threshold is determined by

$$threshold_{initial} = \frac{1}{2}\Big(count_{max} - count_{min}\Big) + count_{min} \tag{2.4}$$

Any counts below that initial threshold are averaged to create a low count average. The new threshold is placed three standard deviations above the low count average. While this method is used extensively in the literature,[20,44,45] I noticed many of our time traces were "noisy" such that the threshold was cutting some "on" and "off" times short (see Fig. 2.7). To address the fact our small molecule time traces have a lower signal to noise ratio, a few tests were done. As shown in Fig. 2.7, the top trace shows that the signal to noise ratio isn't always a problem, but the bottom left trace shows that this is not always the case. Our original MATLAB script would show six "off" times, when there are only two. We first tested to see if moving the threshold (as shown in the bottom right trace) would make change the calculated $N_{tot,em}$, but we found the variation was within

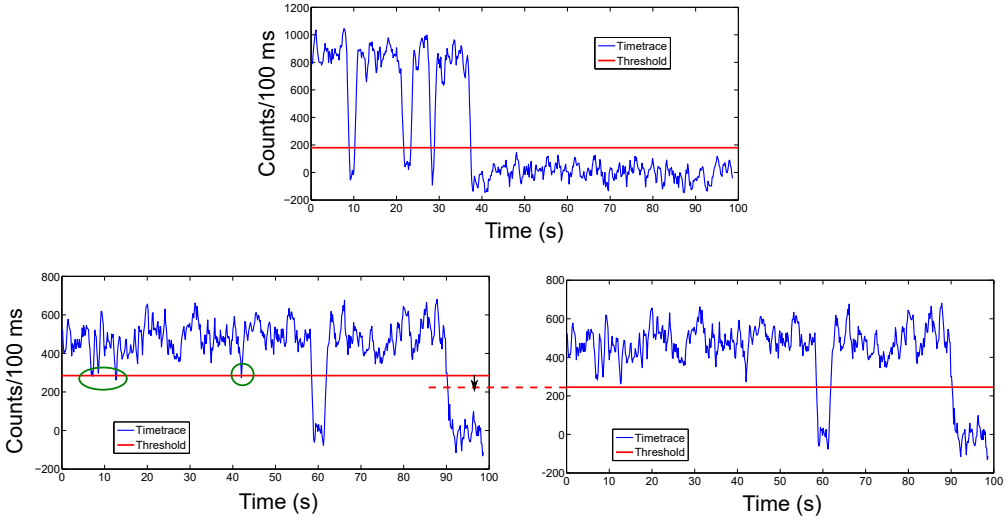

Figure 2.7: Examples of single-molecule fluorescence time traces with various thresholds that separate "on" and "off" states of the molecule. The threshold level was varied to determine how it affects data analysis. **Top:** Threshold level three standard deviations above the average "off" counts/100 ms. **Bottom** Example of threshold that has been lowered such that "on" noise does not interfere with the threshold.[4]

error bars.[4]

While $N_{tot,em}$ calculations are not affected, the analysis of "on" and "off" time distributions will be. While thresholds could be adjusted manually for each trace, this method would be very time consuming. To make analysis more efficient, a custom MATLAB script was written to eliminate noise (see Appendix A). It first uses typical thresholding described above, then identifies blinking events less than 20 (30) frames for traces with less (more) than 20 blinking events, and combines them with the adjacent "on" or "off" time.

To test the functionality of the custom MATLAB script, about 100 fluorophores

were randomly selected per sample to determine "on" and "off" times by going through each trace by hand. These times will be referred to as "handpicked" times. These time distributions were then compared to the results of the custom MATLAB script. Results from the custom MATLAB script and handpicked times were similar for multiple samples, so the custom MATLAB script is used for all noise elimination.

In addition to eliminating noise from "on" and "off" times, the average counts for "on" and "off" times were monitored as a control (Fig. 2.8). As the concentration of donor molecules increased, there was an increase in "on" counts, but that is due to high concentrations of donor molecules making the background counts higher than very low concentrations of donor molecules. Monitoring the average "on"-"off" counts allows us to subtract this higher background. The average "on" - "off" counts remained about the same indicating we were imaging the same donor molecules under similar conditions.

2.4.3 Classifying "blinkers" and "non-blinkers"

Once all noise has been eliminated from time traces, they are classified as either a "blinker" or "non-blinker" molecule. A "non-blinker" is a molecule that photobleaches (see Fig. 2.6) where it begins in the "on" state, then switches to the "off" state for the duration of the video. A "blinker" is classified as a molecule with at least one "off" to "on" transition during our observation time of 100 s, such as the

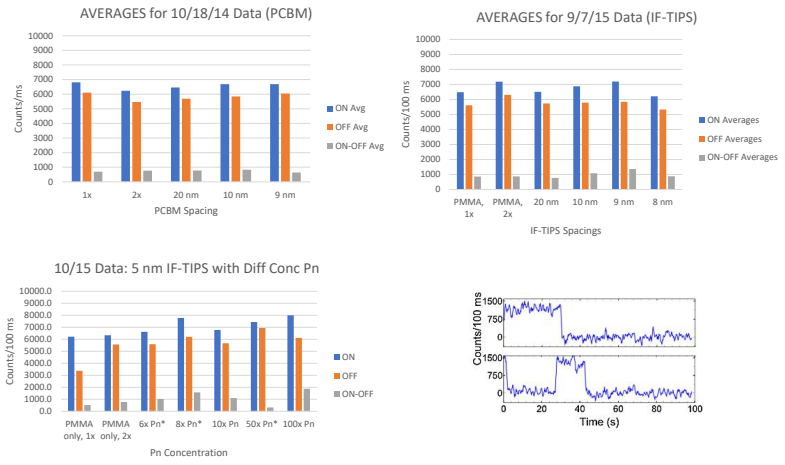

Figure 2.8: Average "on", "off", and "on"-"off" counts for a variety of samples. Samples include (a) increasing PCBM, (b) increasing IF-TIPS, and (c) increasing donor with a constant acceptor concentration (IF-TIPS, 5 nm). (d) The top time trace represents a photobleached molecule while the bottom trace represents a blinking molecule.

fluorophore in Fig. 2.7. A molecule could also begin in the "off" state and turn "on" later.

To investigate donor molecule visibility after 100 s, up to six consecutive videos were analyzed on the same spot as shown in Fig. 2.9. The number of fluophores decreased over time, indicating molecules photobleached over the duration of all six videos. The molecules that appeared in the second and third videos were different from the fluorophores that appeared in the first video, indicating they are a more stable population of molecules that did not exhibit a digital switching behavior in video 1.

2.4.4 Quantifying Time Distributions

To quantify "on" and "off" time distributions, three sets of times were investigated: (i) blinker "on" times, (ii) blinker "off" times, and (iii) nonblinker "on" times. These time distributions were fit to many known distributions to better understand their behavior. For each trace, the last "on" or "off" time was always omitted since video collection was stopped. Counts were then converted to detected photons using the manufacturer-provided analog-to-digital conversion factor (AD Conversion) and the EMCCD gain (EM Gain) as follows

$$photons_{det} = (counts) \times \frac{ADConversion}{EMGain}. \tag{2.5}$$

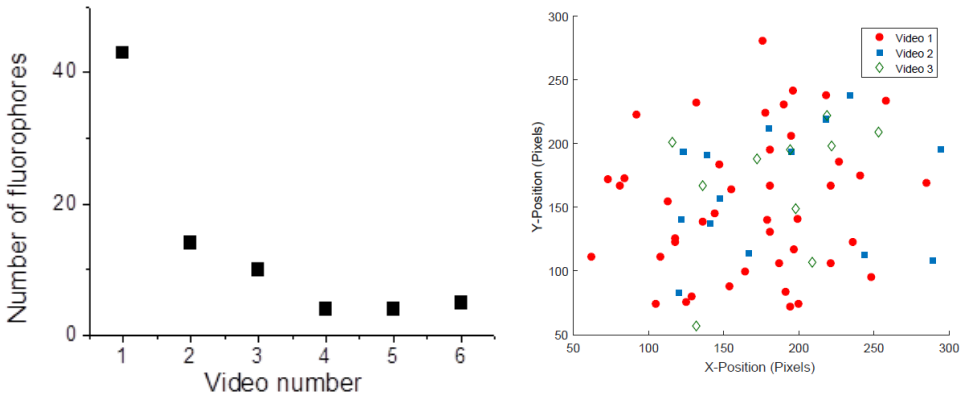

Figure 2.9: On the *left*, the number of fluorophores (with two-level time trajectories) identified in one sample area over up to 6 consecutive videos. Each video is 100 s duration. The decreasing number of fluorophores in each video demonstrates that the length of 100 s videos used in our experiments captures most of the important features of the fluorophore photophysics. Most of the fluorophores identified in videos 2 and 3 are a more stable population of molecules that did not exhibit a digital switching behavior in video 1 and were discarded from analysis as shown on the *right*. The probability of fluorophores considered to be non-blinkers in video 1 but turning on in subsequent videos is low.

Four CCDF distributions were tested: power-law, exponential, Weibull, and lognormal fits. The CDF distributions $S(t)$ are

$$S_{PL}(t) = 1 - \left(\frac{t}{t_{min}}\right)^{-\alpha} \tag{2.6}$$

$$S_{EXP}(t) = 1 - e^{-\lambda t} \tag{2.7}$$

$$S_{WB}(t) = 1 - exp(-t/\beta)^{A} \tag{2.8}$$

$$S_{LN}(t) = \frac{1}{2} erfc\Big(- \frac{ln(t) - \mu}{\sigma\sqrt{2}}\Big) \tag{2.9}$$

respectively, and the CCDF $F(t)$ is calculated by $F(t) = 1 - S(t)$. Note Γ is the Gamma function and $erfc$ is the complementary error function. In general, these distributions have been used in the literature to model the behavior of single molecules.[44]

In particular, the Weibull distribution function has been used in the analysis of fatigue behavior of materials and mechanical strength of complex materials,[46] as well as in descriptions of chemical reactions with distributed activation energies.[47,48] The process is characterized by a time-dependent rate $k(t) = (A/\beta)(t/\beta)^{A-1}$, where A and β are the Weibull fit parameters. When $A > 1$

($A < 1$), the rate of the process increases (decreases) with time, and the CCDF (as shown by Monte Carlo simulations[49,50]). When $A = 1$, the rate is time independent, and the CCDF becomes a single-exponential. In the SMFS data, the Weibull function has been used to describe the distribution of the "on" times resulting from the distributed probability of radical ion pair ISC in perylenediimide single molecules dispersed in PMMA.[51]

The lognormal distribution has been used where several random independent variables, time-dependent rates, or stepwise processes with "memory" have been involved.[52,53] In SMFS, the lognormal distribution has been used to describe the "off" times due to distributed rates for back charge transfer[51,54] and the "on" times distribution due to those for the proton transfer.[52]

2.4.4.1 Least Squares Fitting

Initially, least squares fitting to probability density functions (PDFs) and complementary cumulative distribution functions (CCDFs) was used to study our samples. For each data set, a histogram was first created for the "on" ("off") times, and a probability density distribution was generated with

$$P(t_i) = \frac{2N_i}{(t_{i+1} - t_i) + (t_i - t_{i-1})} \tag{2.10}$$

where N_i is the histogram value at time t_i and t_{i+1} and t_{i-1} are the times

following and proceeding the time t_i in the histogram.[2,45] While this technique works well for systems with triplet state blinking and quantum dots, the PDFs for our molecules have a very broad tail. Cumulative distribution functions (CDFs) are cleaner and easier to fit. They are determined by

$$S(t) = \frac{1}{N} \sum_i t_i < t \tag{2.11}$$

where N is the total number of "on" ("off") times and t_i is a binning time. Since shorter times are more probable for our molecules, the complementary cumulative distribution function (CCDF) is used instead where $F(t) = 1 - S(t)$. Generated $F(t)$ were fit to a variety of distributions including Weibull, lognormal, power law, and exponential distributions. While power law distributions used to be common, E. A. Riley, et al. explain the importance of looking beyond power law fits because the power law does not always physically explaining blinking.[44] All fits are done using least squares fitting where the sum of the squares of the errors are minimized, and R^2 values are calculated.

2.4.4.2 Maximum Likelihood Estimation and p-values

Recently, least squares fitting has been found to underestimate the power law exponent[55,56] and the maximum likelihood estimation (MLE) has been shown to be a more consistent approach.[44,56] MLE estimates parameter values by maximizing

the probability of the data corresponding to that PDF where the probability[44] $\mathcal{L}$ is

$$\mathcal{L}(a_1, a_2, ...a_m) = \prod_{i=1}^{n} f(t_i|a_1, a_2, ...a_m) \tag{2.12}$$

where t_i are data points and a_m are fit parameters. In addition to using MLE, the CDF can also be generated using discrete data points and avoiding binning in histograms all together. Eq. 2.11 is still used, but now t_i corresponds to the actual "on" ("off") times. In other words, for a given $S(t)$, the number of occurrences that a time t_i is less than a given t is divided by the total number of "on" ("off") times N in that given data set. This gives the probability that an event will be shorter than time t.

To check if MLE fit parameters were valid, p-values were calculated using the Kolomogorov-Smirnov (KS) statistic D where

$$D = max_{-\infty<t<\infty}|S_{fit}(t) - S(t)| \tag{2.13}$$

and $S_{fit}(t)$ is the CDF with the fit parameters being tested and $S(t)$ is the actual data set. To calculate the p-value, N_s data sets are generated with the fit parameters, and the KS statistic is calculated for each generated data set. The p-value then becomes

$$p - value = \frac{\sum D_{synth} \geq D}{N_s}. \tag{2.14}$$

Accuracy of the p-value is determined by $1/2\sqrt{N_s}$.[44] As a first test, N_s was set to 100 to determine which fits should be investigated further. N_s was then set to 10,000 to get more accurate p-values. Again, power law, exponential, Weibull, and lognormal fits were tested.

2.5 Results

2.5.1 Donor-acceptor systems under study and visibility

Samples studied at the single molecule level included (i) donor only (plain) samples of varying concentrations, (ii) single molecule donor samples with varying concentrations of added acceptor, and (iii) average acceptor spacings of 5 nm with added donor molecules of varying concentrations. Fig. 2.10 illustrates how the number of visible donor molecules decreases with added acceptor as the concentration of donor molecules increases. The number of donor molecules visible in each sample is shown in Fig. 2.11 along with the expected number of visible fluorophores.[49]

This change in visibility could be attributed to Förster Resonance Energy Transfer (FRET). FRET occurs between two fluorescent dyes when the emission spectrum of one fluorophore overlaps with the absorption spectrum of another flu-

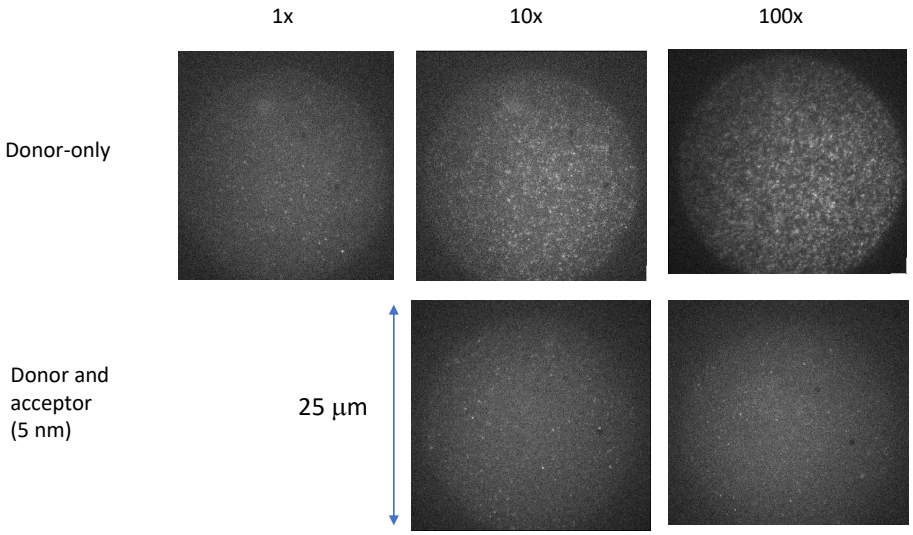

Figure 2.10: Screenshots of different samples. **Top:** Donor-only samples with increasing concentration from left to right. **Bottom:** D/A (IF-TIPS) samples with increasing concentrations of donor from left to right where acceptor spacing is 5 nm. Note donor molecules were not visible at this spacing with a 1x donor concentration.

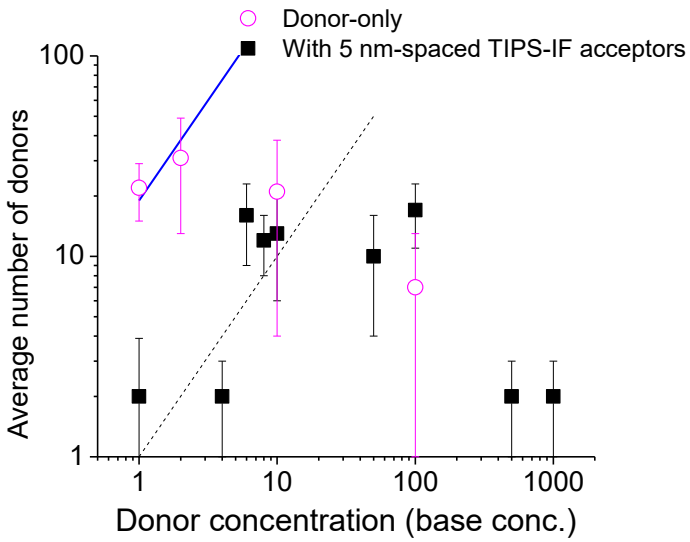

Figure 2.11: Average number of detected Pn-TCHS-F8 molecules (characterized by two-level digital-switching time trajectories) in the field of view depending on the donor concentration, in donor-only samples and in donor-acceptor samples with 5 nm-spaced IF-TIPS acceptors. The donor concentration is given in terms of the base concentration (3.4×10^{-10} M). Error bars correspond to variations in the fluorophore numbers in different areas of the sample. Lines show expected scaling behavior at low concentrations, in donor-only (blue) and donor-acceptor (black) samples, when the average donor-donor separation is considerably higher than the minimal separation resolved within the diffraction limit.

orophore close by and the energy is transfered.[57] The efficiency of FRET E_d can be expressed as

$$E_d = \frac{1}{1 + (R/R_0)^6}, \tag{2.15}$$

where R is the distance between donor and acceptor molecules[1] and R_0 the Förster radius. The Förster radius is a constant, and is the distance between a donor/acceptor pair at which the FRET efficiency is at 50%.[57]

To investigate this phenomenon, an experimental FRET radius was calculated as shown in Fig. 2.12.[49] Eq. 2.15 was modified to

$$y = \frac{A}{1 + (B/x)^6}, \tag{2.16}$$

where A and B are the fit parameters representing the number of fluorophores visible without acceptor and the distance between acceptor molecules $2R$ respectively, y is the number of fluorophores visible, and x is the acceptor spacing. For the donor and IF-TIPS, R_0 was calculated to be 3.1 $\pm$ 0.3 nm. For the donor and PCBM, R_0 was found to be 3.9 $\pm$ 0.4 nm. These radii agree with the FRET radius calculated with the overlap integral as described in Appendix B where R_0 for the donor and IF-TIPS (PCBM) is 2.7 nm (3.4 nm). The overlap of the acceptor absorption spectra and donor fluorescence spectra is shown in Fig. 2.13.[49] The change in PL and lifetimes of donor-only to donor-acceptor samples is also

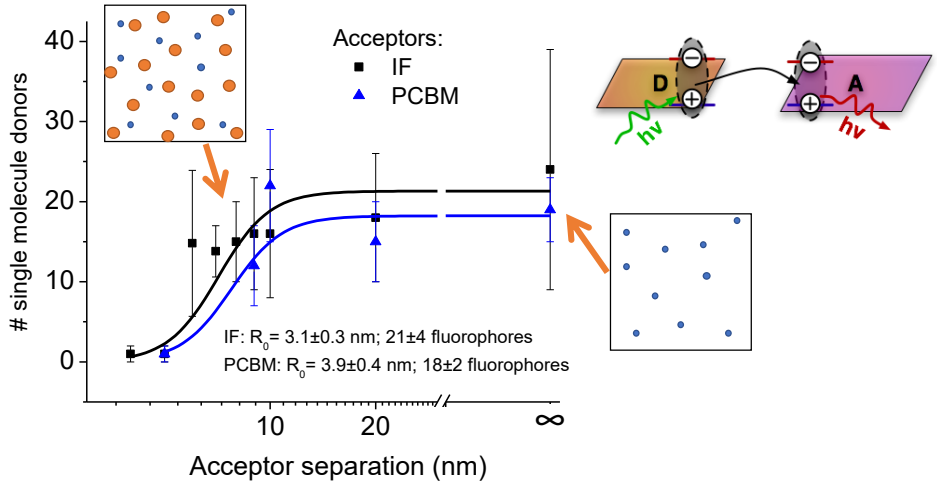

Figure 2.12: Acceptor separation as function of the number of visible single molecule donors. FRET radii for each acceptor were estimated by fitting Eq. 2.16 to the number of visible donors.

apparent in Fig. 2.14.[49]

As FRET limits visibility of donor molecules at 5 nm average acceptor spacings, higher donor concentrations (as compared to those in all other donor-acceptor samples) were used to increase the probability of obtaining the donor-acceptor spacing higher than R_0. In this case, FRET served as a super-resolution tool enabling experiments at donor concentrations of up to two orders of magnitude higher than that used in donor-only samples! FRET ensured only one donor molecule was emissive within the diffraction limited range. The molecules imaged were then spaced at least $\sim 3 - 3.5$ nm away from the nearest acceptor molecule. Therefore, they do not directly participate in energy or charge transfer interactions with

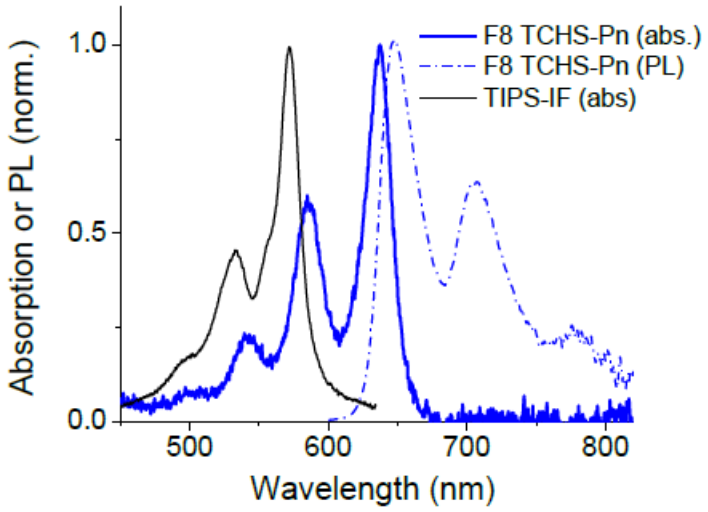

Figure 2.13: Absorption spectra of Pn-TCHS-F8 and IF-TIPS molecules and PL spectrum of Pn-TCHS-F8 molecules in toluene.

the acceptor, but serve as sensors for the acceptor-induced changes in the local nanoenvironment that are important for their photophysics.

2.5.2 Effect of acceptor addition on fluorescence time trajectories

The total number of photons emitted over a fluorophore's lifetime N_{tot} or the detected photons $N_{tot,det}$ decreases as the average acceptor-acceptor separation is 9 nm or below as shown in Fig. 2.15.[49] This decrease in number of photons can be seen when looking at the smaller percentage of non-blinkers and the shorter average on duration τ_{on}. Fig. 2.16 demonstrates while only $\sim 10-14\%$ of Pn-

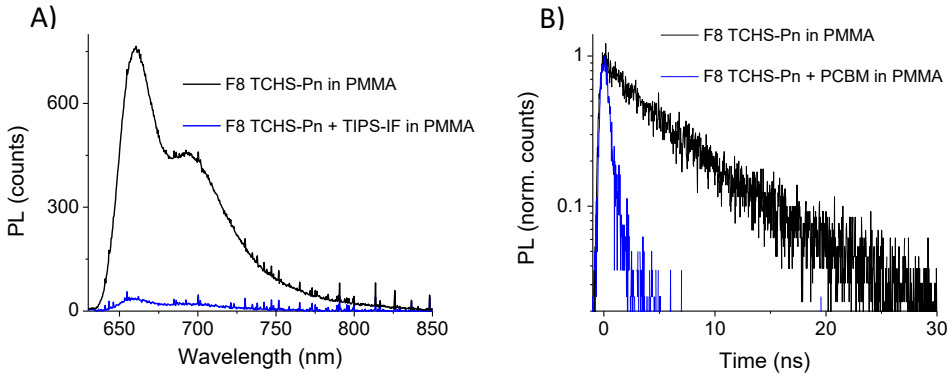

Figure 2.14: A) Photoluminescence (PL) spectra for Pn-TCHS-F8 donor emission from samples with low concentrations of Pn-TCHS-F8 in donor-only and in donor-acceptor "bulk" samples in PMMA under 633 nm excitation. Dramatic quenching of the Pn-TCHS-F8 PL is observed in donor-acceptor samples due to FRET; the IF-TIPS acceptors are not emissive under these conditions. B) PL lifetime decay of the Pn-TCHS-F8 donor emission in donor-only and donor-acceptor "bulk" samples with PCBM acceptor. Fast quenching due to efficient FRET is observed in the donor-acceptor sample.

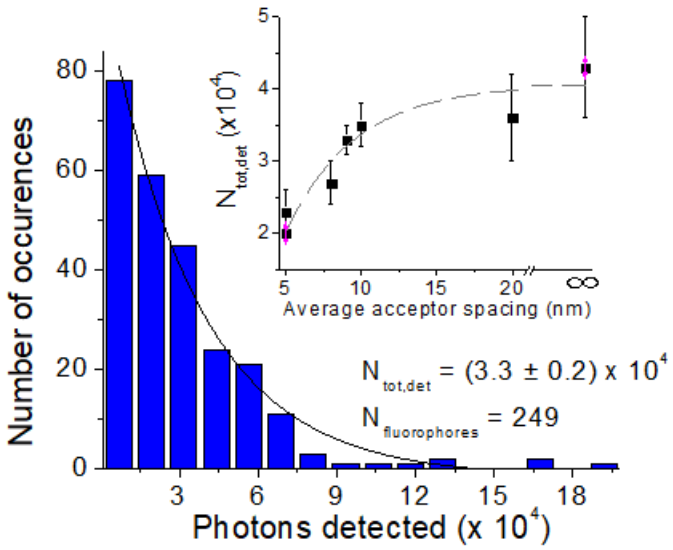

Figure 2.15: Example of a histogram obtained from an ensemble of 249 fluorophores in a donor-acceptor sample with 9 nm-spaced IF-TIPS acceptors and of a single exponential ($\sim exp(-N_{det}/N_{tot,det})$) fit from which the total number of detected photons $N_{tot,det}$ was calculated. Inset shows a change in $N_{tot,det}$ as IF-TIPS acceptors are added. Line provides a guide for the eye.

TCHS-F8 molecules are "blinkers" in donor-only samples, this number increases to over $\sim 50\%$ in donor-acceptor samples at average acceptor-acceptor separation of less than 8 nm.[49]

These observations indicate the addition of acceptor molecules is changing the nanoenvironment of the Pn-TCHS-F8 donor molecule reporters. Now, the effect on their photophysics will be investigated.

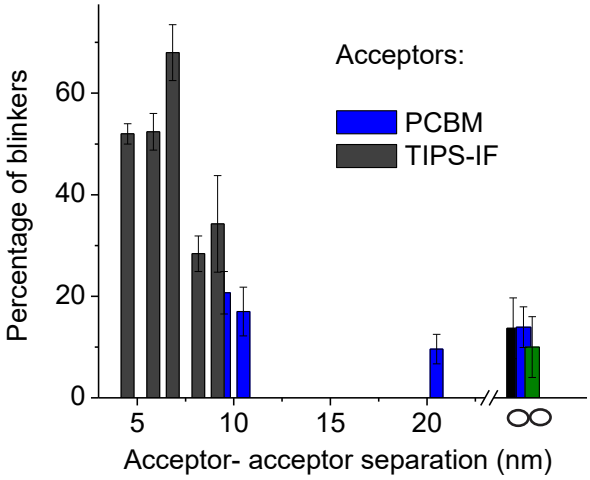

Figure 2.16: Percentage of "blinking" molecules depending on the average acceptor spacing. Error bars correspond to the spot-to-spot variation in each sample. Data from three different donor-only samples (infinite acceptor spacing) are also included.

2.5.3 Evolution of average "on" and "off" time durations

To better understand the underlying physics behind the change in N_{tot} (Fig. 2.15) and percentage of blinkers (Fig. 2.16) with added acceptor, the fluorescence time traces for "blinkers" and "non-blinkers" were separated. Since the integration time of the EMCCD was 100 ms, microsecond time-scale blinking (ie due to intersystem crossing (ISC)) is not observed as the molecule appears to be "on" even after the ISC from S_1 to T_1 has occurred provided it is followed by the T_1 to S_0 relaxation, S_0 to S_1 re-excitation, and emission.[51] As shown in Fig. 2.17, "off" times are on longer time scales of at least 3 s and $\sim 20 - 40$ s on average.[49] In the literature these long-lived dark states have been due to i) charge transfer reactions where the dark state is a charge-separated state or ii) photo-oxidation reactions such that the fluorescent parent molecule reactions with oxygen to create a dark intermediate state followed by photo-oxidation products with different emission properties.[51,58,59] These possible cases will be explored in the discussion section.

Observed "on" for "blinkers," "on" for "non-blinkers," and "off" for "blinkers" time durations were compiled for each sample type, and complementary cumulative distribution functions (CCDFs) were calculated directly from experimental data[44,51] as described in the data processing section. These time duration lists were compiled for $\sim 150 - 350$ fluorophores depending on the acceptor concentration (see Tables 2.1 and 2.2).[49] An example of CCDFs from experimental data are shown in Fig. 2.18 demonstrating shorter "on" and longer "off" time durations, on average, as acceptor is added.[49]

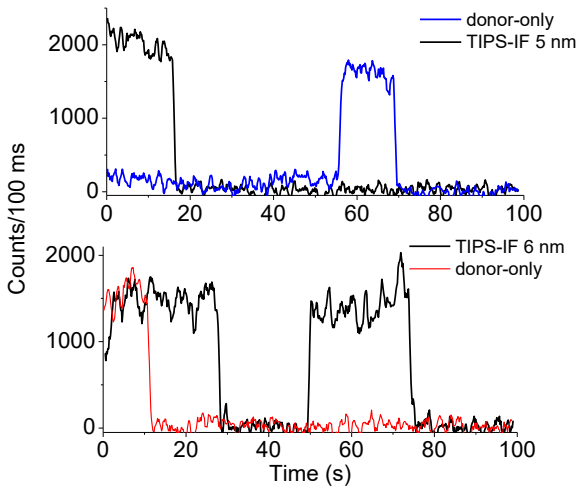

Figure 2.17: Examples of "non-blinker" and "blinker" Pn-TCHS-F8 fluorescence time trajectories obtained in donor-only and donor-acceptor samples with average acceptor-acceptor separation indicated.

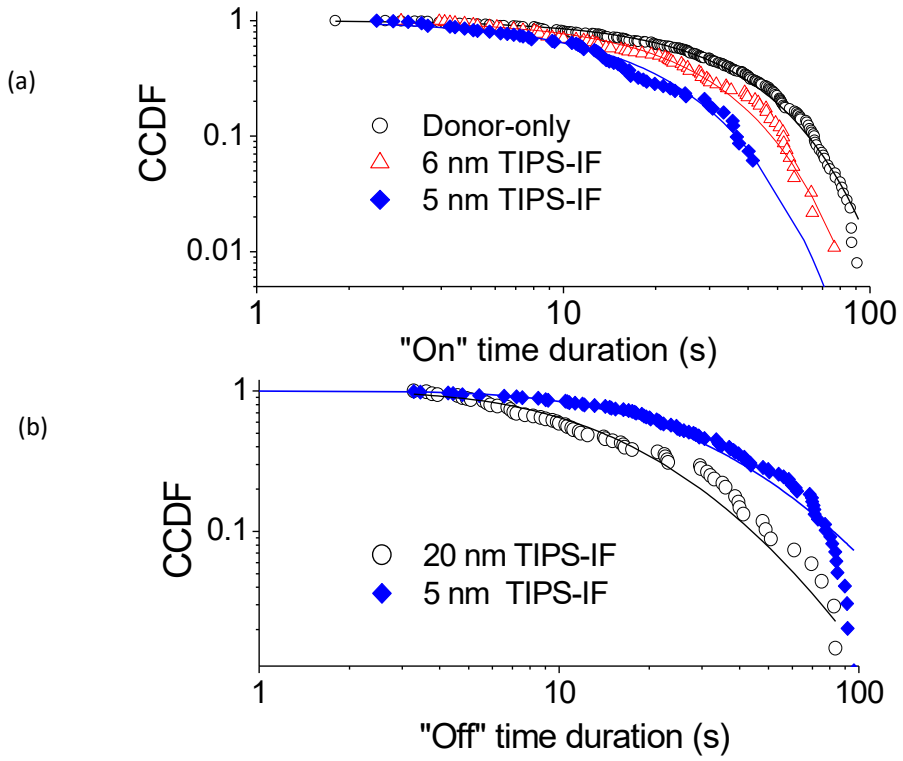

Figure 2.18: The complementary cumulative distribution functions (CCDFs) for "non-blinker" "on" times (*top*) and "blinker" "off" times (*bottom*) compiled from $\sim 90-170$ fluorescence time traces, depending on the sample. Fits to the data with functions that resulted in the highest p-values are also shown. The "on" CCDFs were mostly Weibull-distributed (for example, a p-value of 0.93 for the donor-only sample shown), and Weibull fits ($\sim exp[-t/\beta]^A$) to the data are included. The "off" CCDFs exhibited either lognormal or Weibull behavior. In these examples, the Weibull distribution was predominant.

Data Set Number	Sample	Number of Fluorophores Analyzed
1	Donor-only (1x)	289
	Donor-only (2x)	358
	Donor (1x) - Acceptor (10 nm IF-TIPS)	187
	Donor (1x) - Acceptor (9 nm IF-TIPS)	225
	Donor (1x) - Acceptor (8 nm IF-TIPS)	308
2	Donor-only (2x)	290
	Donor (6x) - Acceptor (5 nm IF-TIPS)	249
	Donor (10x) - Acceptor (5 nm IF-TIPS)	182
	Donor (50x) - Acceptor (5 nm IF-TIPS)	115
3	Donor-only (2x)	334
	Donor (1x) - Acceptor (10 nm PCBM)	287
	Donor (1x) - Acceptor (9 nm PCBM)	151
4	Donor-only (1x)	264
	Donor-only (2x)	358
	Donor-only (10x)	253
	Donor (1x) - Acceptor (7 nm IF-TIPS)	142
	Donor (1x) -Acceptor (6 nm IF-TIPS)	171

Table 2.1: Examples of data sets under study and the number of fluorophores used in analysis of each data set. Each data set was taken on a separate day.

				p-values			
CCDF type	Sample	Number of Fluorophores	N_s	Power Law	Lognormal	Exponential	Weibull
Non-blinkers "on"	Donor-only	158	100	0	0	0	**0.93**
	10 nm IF-TIPS	104	100	0	0.04	0	**0.47**
	9 nm IF-TIPS	115	100	0	0	0	**0.33**
	8 nm IF-TIPS	195	100	0	0	0	**0.25**
	5 nm IF-TIPS	116	10,000	0	0.03	0.01	**0.48**
Blinkers "on"	Donor-only	79	100	0	0.57	0	**0.94**
	9 nm IF-TIPS	61	100	0	0.06	0.05	**0.72**
	6 nm IF-TIPS	75	100	0	0.07	0.01	**0.2**
	5 nm IF-TIPS	43	100	0	0.14	0.06	**0.78**
Blinkers "off"	Donor-only	66	10,000	0	**0.23**	0.02	0.02
	Donor-only	42	100	0	0.12	0	**0.17**
	20 nm IF-TIPS	77	100	0	**0.05**	0.02	0
	10 nm PCBM	22	100	0	0.08	0.18	**0.43**
	8 nm IF-TIPS	104	100	0	0.04	0.13	**0.27**
	7 nm IF-TIPS	66	100	0	0.02	0.06	**0.19**
	5 nm IF-TIPS	93	10,000	0	0.22	0.02	**0.41**
	Donor-only	77	10,000	0	**0.09**	0.02	0.05
	6 nm IF-TIPS	75	100	0	**0.33**	0.11	0.14

Table 2.2: Results of selected p-tests. The highest p-value is shown in bold.

To determine which CCDF distribution is more probable, p-tests were used to test power-law, lognormal, Weibull, and single-exponential distributions.[44,51,54] As shown in Tables 2.2 and 2.3, for most samples, the CCDFs for the "on" times (t_{on}) in "non-blinkers" were best described by the Weibull function CCDF from Eq. 2.8 where A and β are fit parameters.[49] For example, $p = 0.93$ and 0.48 were calculated for "on" times in a donor-only and a donor-acceptor with 5 nm spaced acceptors samples respectively (as shown in Fig. 2.18) while all other functions tested yielded $p \leq 0.03$ (Table 2.2).

The average "on" times $\langle\tau\rangle_{on}$ were calculated from the Weibull fit parameters where $\langle\tau\rangle_{on} = \beta\Gamma(1 + 1/A)$ (and Γ is the Gamma function) depending on the average acceptor-acceptor spacing as shown in Fig. 2.19.[49] As acceptor is added, the average "on" time decreases from (32 ± 1) s in donor-only samples to (14 ± 1) s in donor-acceptor samples with a 5 nm average acceptor spacing. Table 2.3 shows the Weibull scaling parameter β decreased as acceptor was added while the parameter A did not show any strong trends.

In "blinkers," the average "on" times $\langle\tau\rangle_{on}$ were similar to those in "non-blinkers" in most samples (as shown in Fig. 2.19 and Fig. 2.20).[49] While $\langle\tau\rangle_{on}$ values were similar, the fit parameters A and β were slightly different (Table 2.3). As with "non-blinkers," the average on times in "blinkers" decreased with added acceptor (Fig. 2.19).

For "off" times (t_{off}) CCDFs, p-tests mostly indicated the Weibull distribution, though some samples favored the lognormal distribution (Eq. 2.9) where μ and σ

		Weibull (or Lognormal) fit parameters		Average time
CCDF Type	**Sample**	A **(or** σ**)**	β **(s) (or** μ**)**	$\langle\tau\rangle_{on}$ **or** $\langle\tau\rangle_{off}$
Non-blinkers "on"	Donor-only	1.34	34.3	31.5
		1.30	35.2	32.5
		1.47	34.8	31.5
		1.48	31.3	28.3
		1.52	39.4	35.3
	20 nm IF-TIPS	1.47	29.8	27.0
	10 nm IF-TIPS	1.44	33.1	30.0
	9 nm IF-TIPS	1.55	40.2	36.1
	8 nm IF-TIPS	1.57	39.7	35.6
	6 nm IF-TIPS	1.39	26.2	23.9
	5 nm IF-TIPS	1.30	21.4	19.8
		1.54	10.1	9.1
		1.40	14.8	13.5
		1.27	15.8	17.6
Blinkers "on"	Donor-only	1.79	37.8	33.6
		1.56	36.9	33.1
		1.62	31.7	28.4
		1.91	41.2	36.6
		1.88	34.1	30.3
	20 nm IF-TIPS	1.93	36.2	32.1
	10 nm IF-TIPS	1.80	41.7	37.1
	9 nm IF-TIPS	1.59	37.7	33.8
	5 nm IF-TIPS	1.19	15.7	14.8
		1.46	15.3	13.9
		1.34	14.7	13.5
		1.31	13.7	12.7
Blinkers "off"	Donor-only	1.09	25.8	25.0
		1.20	22.7	21.3
		1.11	23.4	22.5
		1.09	15.0	14.5
		1.02	24.5	24.3
		(0.89)	(2.67)	(21.5)
	20 nm IF-TIPS	1.15	22.1	21.1
		(0.89)	(2.64)	(20.9)
	8 nm IF-TIPS	1.26	31.2	29.0
	7 nm IF-TIPS	1.20	29.0	27.3
	5 nm IF-TIPS	1.52	42.0	37.9

Table 2.3: Examples of fit parameters obtained from selected CCDF fits to the Weibull (or Lognormal, when in parenthesis, for the data sets with higher p-values for Lognormal) function.

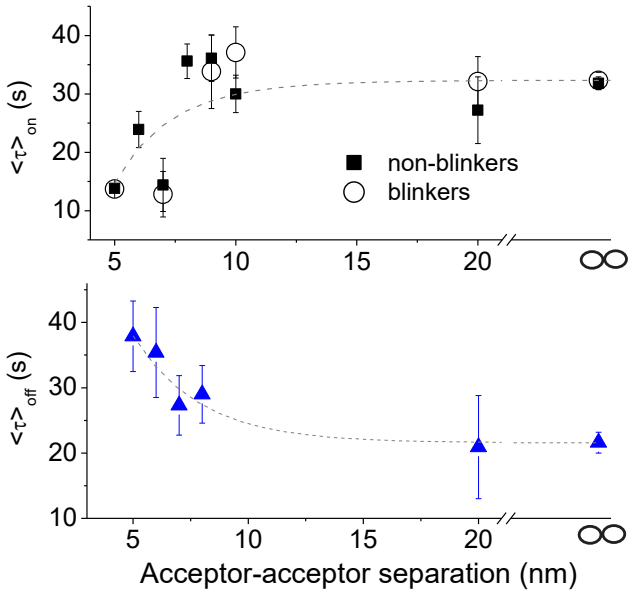

Figure 2.19: Average "on" for "non-blinkers" and "blinkers" (*top*) and "off" for "blinkers" (*bottom*) times calculated from fit paramters (either Weibull or lognormal) depending on the average acceptor spacing. Lines provide a guide for the eye.

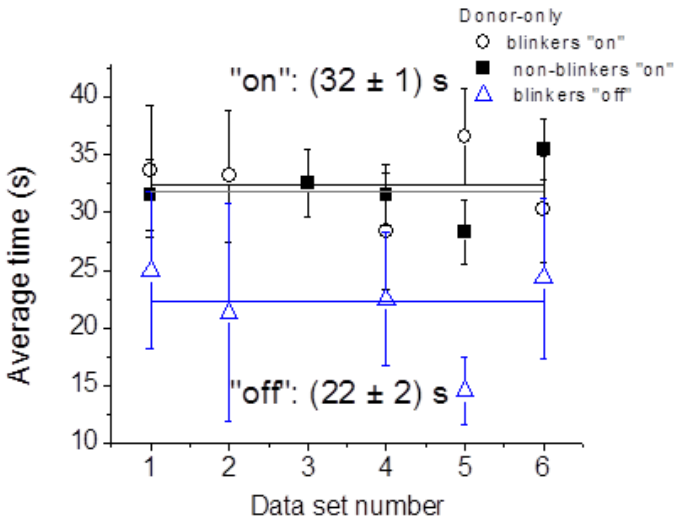

Figure 2.20: Average "on" and "off" times calculated from Wibull fit parameters for donor-only samples measured on different days (represented by data set numbers). Error bars correspond to variation in values obtained from different areas of the same sample. The lines are fit to a constant. The average "on" times for "blinkers" and "non-blinkers" were similar within the error.

are fit parameters (Tables 2.2 and 2.3).[44] The average "off" times calculated from fit parameters can be found in Fig. 2.19 and demonstrate an increase in the average "off" time as acceptor is added from 22 s in donor-only samples (Fig. 2.20) to 38 s in donor-acceptor samples with an acceptor spacing of 5 nm. As with the "on" times, the Weibull scaling parameter β increases with added acceptor, but A also increases with added acceptor.

As described in the data processing section, both the Weibull and lognormal distributions suggest distributed activation energies for the processes that are responsible for the molecule turning "on" or "off", which will be discussed below.

2.5.4 Correlations between the durations of the "on" times and the preceding "off" times

The possible correlations between the "on" times and the immediately preceding "off" times in "blinkers" were also studied. As shown in Figs. 2.21 and 2.22, the dependence changed depending on the sample type.[49] For example, in donor-only samples, the duration of "on" times decreased as the duration of the "off" time increased. However, for donor-acceptor samples at high acceptor concentrations (5 nm spacings), no trend was observed for relatively long "off" times. For donor-acceptor samples, there is a higher probability of obtaining long "on" times following a long "off" time when compared to donor-only samples. This observed difference suggests the added acceptors play a critical role during the "off" time

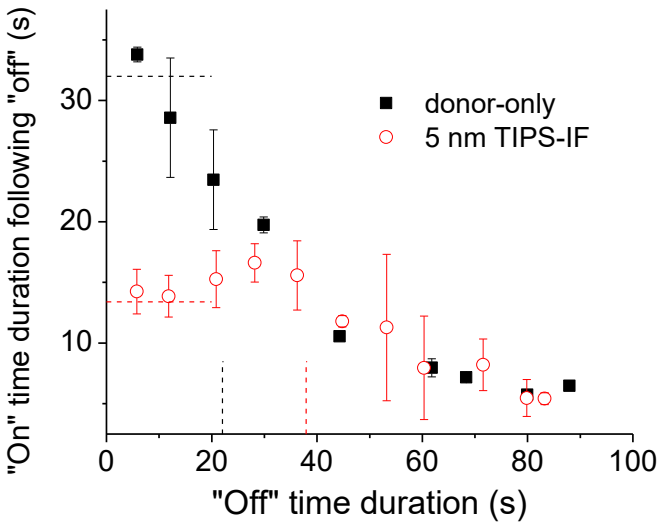

Figure 2.21: Correlation between an "on" time and preceding "off" time in "blinkers" is observed in donor-only and donor-acceptor samples with the 5 nm spaced IF-TIPS acceptor molecules. The lines indicate average "on" or "off" times from Fig. 2.19 in the same samples.

of the Pn-TCHS-F8 molecule by reducing the negative impact of the "off" event on the following "on" period.

2.6 Discussion

Fig. 2.23 is used to describe the observed behavior presented in the results.[49] In this model, the detected emission occurs from the excited state (2) to the ground

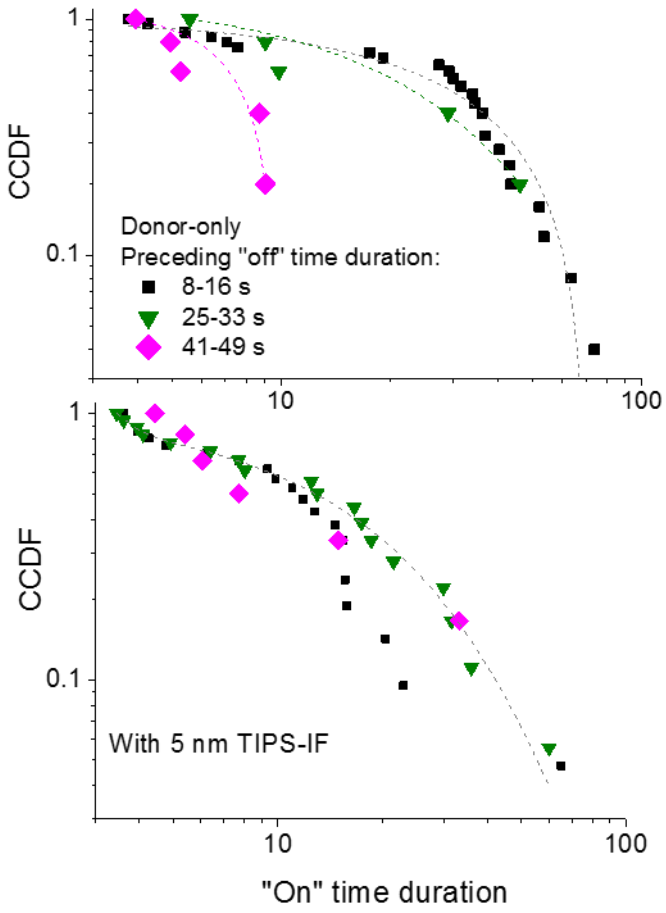

Figure 2.22: CCDFs to illustrate the dependence of the "on" time duration on the preceding "off" time duration in "blinkers" for donor-only sample (*top*) and donor-acceptor samples with 5 nm spaced IF-TIPS acceptors (*bottom*). Lines are to guide the eye. In donor-only samples, the probability to observe an "on" time longer than 10 s following an "off" time decreases as the "off" time increases. No dependence of the "on" times from the preceding "off" times is observed in the donor-acceptor samples at high acceptor concentration.

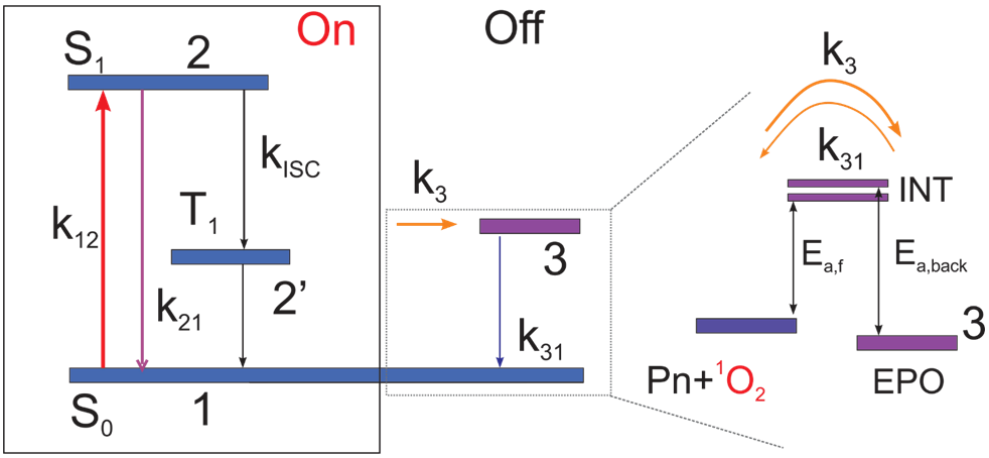

Figure 2.23: Model describing the processes involved and their characteristic rates. The model is described in the text.

state (1), and the transition to the state 3 corresponds to the molecule turning "off" such that state 3 is a "dark" state. The rate responsible for this process depends on the nature of the "dark" state. Since average "on" times for "blinkers" and "non-blinkers" were similar, both population probably share the same pathway for turning "off," which is similar to other reports of organic molecules in polymer matrices.[59,60]

Once in the "dark" state, a "blinker" can return back to the ground state to be re-excited at a rate k_{31} that determines the "off" time. On the other hand, a "non-blinker" would not return back to the ground state. Since most "non-blinkers" do not turn back on for at least 10 minutes (as shown in Fig. 2.9), these molecules are considered "photobleached" even if the process is reversible at longer time scales.[35]

2.6.1 Photodegradation of Pn derivatives

It has been shown that fluorination of the molecular core in functionalized acene derivatives improve their photostability combared to non-fluorinated derivatives[3,61] and will also be demonstrated in the next chapter. The electron-deficient nature of the fluorinated core leads to this enhanced photostability. The addition of eight fluorine substituents shifts the LUMO level from -3.35 eV (Pn-TIPS) to -3.6 eV (Pn-TIPS-F8), making a reaction involving electron transfer from the photoexcited pentacene substantially less favorable. It will be shown in the next chapter that oxygen also plays a critical role in photobleaching of Pn-R-F8 for molecules dispersed in PMMA.

As acenes are important for organic semiconductor devices, acene-oxygen interactions have been studied extensively.[35,62–68] There are two pathways of photooxidation discussed for acene derivatives: type I via electron transfer or type II via energy transfer to oxygen. Type I results from a formation of an acene cation and superoxide (O^{2-}) while type II proceeds by the ISC followed by the energy transfer to the oxygen molecue in its ground state ($^3O_2$) that yields singlet oxygen ($^1O_2$).[62,65] Both O^{2-} and $^1O_2$ are reactive species that could attack the acene molecule leading to an endoperoxide (EPO) formation, which is the main product of acene photobleaching toward decomposition.

The relative contribution of the types I and II processes into photodegredation depends on the derivative.[35] For example, in unsubstituted Pn, the dominant

pathway has been identified to be a concerted type II reaction,[62] whereas for Pn-TIPS both type I and type II processes were realized with the type I process proceeding faster. In particular, in Pn-R derivatives, triplet state energies lower than the singlet-triplet energy gap for O_2 (0.98 eV) have made the type II process inefficient.[35,64,65] However, in a stable bistetracene (BT) derivative, BT-TIPS, the type II process was still dominant, even though the adiabatic triplet state energy was 0.7 eV, due to a considerably higher rate of the backward electron transfer as compared to the forward one and a 0.4 eV range of possible singlet-triplet gap energies caused by energy differences in adiabatic and vertical transitions. A similar situation was reported in the unsubstituted Pn.[62] Fluorination of the Pn core have been observed to lower the triplet state energy.[69]

In many functionalized acenes, the EPO formation was found to be a reversible process with the reversibility time-scale and the activation energy for this process dependent on the derivative.[35] For this study, EPO-TIPS forms when Pn-TIPS oxidation reverted to the parent Pn-TIPS molecule with a clean cleavage of the oxygen molecule. Similar observations were made on other derivatives with triple bonded side groups. The triple bonds of Pn-TCHS-F8 could then protect the acene molecule from irreversible photobleaching (decomposition).[35]

As discussed earlier, the fluorinated derivatives Pn-R-F8 exhibit deeper LUMO energies compared to their non-fluorinated Pn-R counterparts (e.g. by ~ 0.25 eV in Pn-TIPS-F8 compared to Pn-TIPS and by ~ 0.9 eV as compared to the unsubstituted Pn).[6,65,70] This difference dramatically reduces the driving force for

the type I process, making the electron transfer from the electron-deficient Pn-TCHS-F8 to oxygen, with the formation of Pn-TCHS-F8 cation and superoxide, highly unlikely. On the other hand, the triplet state energy for Pn-TCHS-F8 is expected to be even lower than that in Pn-TIPS, and so the type II process is also inefficient. These considerations enable high photostability of Pn-R-F8 derivatives. Following the arguments of Ref. 62, we hypothesize that the type II mechanism, in which the singlet oxygen is generated via self-sensitization and then reacts with the Pn-TCHS-F8 molecule, is the dominant mechanism of photo-oxidation for this molecule. In Pn-TIPS, the types of the EPO that formed as a result of photo-oxidation were 6,13-TIPS-EPO:5,11-TIPS-EPO (98:2),[35] which suggests that our main photo-oxidation product is 6,13-TCHS-EPO. Next, experimental observations consistent with this hypothesis will be discussed.

2.6.2 Nature of the "dark" state

The reaction of an acene with a singlet oxygen towards formation of an EPO can proceed via different pathways.[35,62] For example, in the unsubstituted Pn and BT-TIPS, the joint mechanism was found to have a lower activation energy (13.6 and 17.7 kcal/mol for Pn and BT-TIPS, respectively) for the EPO formation as compared to the stepwise mechanism.[62] On the other hand, the Pn-TIPS derivative first forms an exciplex with the singlet oxygen which then converts to the EPO.[35] Either scenario could be realized in our system, and our present experi-

ments cannot differentiate between these relatively short-lived intermediate states (INT in Fig. 2.23). Regardless of the nature of the intermediate state, we assign our long-lived, and potentially reversible, "dark" state (3 in Fig. 2.23) to the 6,13-TCHS-EPO.

Photo-oxidation reactions have been previously observed using SMFS.[58,71] For example, in the case of terrylene, after the parent molecule stopped emitting (turned "off") for several seconds, the fluorescence re-emerged having a different emission rate and a spectrum that is characteristic of an EPO.[58] For some of the molecules, several photo-oxidation reactions, resulting in different reaction products, could be observed over the period of $\sim$ 60 s under photoexcitation. In the fluorescence time trajectories (as shown in Fig. 2.17), this is observed in a different count level for each "on" state following the "off" state. In this case, the dominant 6,13-TCHS-EPO product would be non-emissive ("dark") under 633 nm excitation[35] used in these experiments. When a "blinker" molecule turns back "on" following an "off" period, it signifies that the EPO reverted back to the parent Pn-TCHS-F8 molecule, which then continues to emit with the same photon emission rate until the next cycle of singlet oxygen generation and EPO formation.

2.6.3 Effect of acceptor addition on the EPO formation and reversal

With an assignment of the molecule turning "off" and back "on" to the forward and reversed (backward) oxidation reactions, two questions arise regarding (i) how

the observed "on" and "off" time distributions (as shown in Fig. 2.18) are related to the kinetics of these reactions and (ii) how the acceptor addition affects these processes. These questions are addressed next.

As mentioned above, both the Weibull and lognormal distributions (which provided best fits to our CCDF data) have been utilized in describing chemical reactions with a distributed activation energy. For example, in the case of Weibull distribution, the time-dependent Weibull rate $k(t)$ can be related to the activation energies via $k = k_0 exp[-E_a/RT]$ where k_0 is a pre-exponential factor, E_a is the activation energy, R is the universal gas constant, and T is the temperature. Then, the distribution function $D(E_a)$ for the activation energies is given by[48]

$$D(E_a) = PDF(t)|dt/dE_a| \tag{2.17}$$

where combining

$$PDF(t) = (A/\beta)(t/\beta)^{A-1} exp[(-t/\beta)^A]) \tag{2.18}$$

where $PDF(t)$ is the Weibull probability function and

$$E_a = -RT(ln(A/(k_0\beta)) + (A-1)ln(t/\beta)) \tag{2.19}$$

where E_a is the activation energy, the distribution function for the activation

energies becomes[44]

$$D(E_a) = \frac{1}{RT}\frac{A}{A-1}\left(\frac{t}{\beta}\right)^A e^{-(t/\beta)^A}. \tag{2.20}$$

This enables extraction of the distribution functions $D(E_a)$ based on the A and β parameters obtained from fits to the "on" or "off" time durations CCDFs. In the following estimates, $k_0 = k_B T/h \approx 6.17 \times 10^{12}\ s^{-1}$ (where k_B is the Boltzmann constant, h is the Planck constant, and $T = 295$ K), used in the transition state theory, will be assumed. This assumption determines the absolute scale for the activation energies and does not affect their distribution and/or trends discussed below.

The average "off" time duration $\langle\tau\rangle_{off}$ is related to the rate k_{31} of Fig. 2.23. If the "off" CCDFs were single-exponential, then k_{31} would be a constant ($\langle\tau\rangle_{off} = 1/k_{31}$), which would correspond to a single activation energy for the backward reaction $E_{a,back}$ from the EPO to the parent molecule. Because the "off" times CCDFs obtained from our data were predominantly Weibull-distributed, there is a distribution in activation energies as shown in Fig. 2.24.[49] In donor-only samples, the distribution $D(E_{a,back})$ is narrow owing to the values of the Weibull parameter A close to 1 (e.g.,$A = 1.1$ for the donor-only data in Fig. 2.24). The lognormal-tending CCDFs observed in some donor-only samples (Table 2.2) then would indicate a more symmetric, closer to the Gaussian, distribution of activation energies. The most probable activation energy $E^0_{a,back}$ in a donor-only sample

yielded a value of $E^0_{a,back} = 19.05$ kcal/mol or ~ 80 kJ/mol. This is lower than the $\sim$ 90 kJ/mol obtained for the thermolysis reaction in several reversible functionalized acene-EPOs,[35] consistent with a more favored reverse reaction in Pn-TCHS-F8. As acceptors are added, the distribution $D(E_{a,back})$ shifts towards the higher activation energies and broadens (Fig. 2.24).

The average "on" time duration ($\langle\tau\rangle_{on}$), in a simple case of a single-exponential "on" CCDF, is related to the rate of the EPO formation (k_3 in Fig. 2.23) by $\langle\tau\rangle_{on} = 1/(\Phi_{O2}k_3)$, where Φ_{O2} is the probability of generating singlet oxygen upon photon absorption. In our case of Weibull-distributed "on" CCDFs, the activation energies for the forward reaction ($E_{a,f}$) are distributed according to $D(E_{a,f})$ as shown in Fig. 2.24, and Φ_{O2} determines the absolute scale for the activation energies given by $E^0_{a,f}$. The upper bound on Φ_{O2} is imposed by the ISC efficiency. If we assume an ISC triplet yield of $\sim 1\%$ (so that $\Phi_{O2} = 0.01$),[72] the most probable activation energy ($E^0_{a,f}$) in donor-only samples for "non-blinkers" yields $\sim$ 16.5 kcal/mol, which is in between 13.6 kcal/mol and 17.7 kcal/mol obtained for concerted reactions of the unsubstituted Pn and BT-TIPS, respectively, with singlet oxygen.[62] As the Pn-TCHS-F8 derivative is an order of magnitude more stable[3] than Pn-TIPS, which in turn is about 50 times more stable than the unsubstituted Pn,[64] it is reasonable to expect that the activation energy for the forward reaction for Pn-TCHS-F8 would be considerably higher than that for the unsubstituted Pn. However, there is an alternative scenario which yields a different scaling energy $E^0_{a,f}$ that could be operational here, as discussed below. Regardless of the absolute scale set by the value of $E^0_{a,f}$, as acceptors are added, the activation energies shift to the

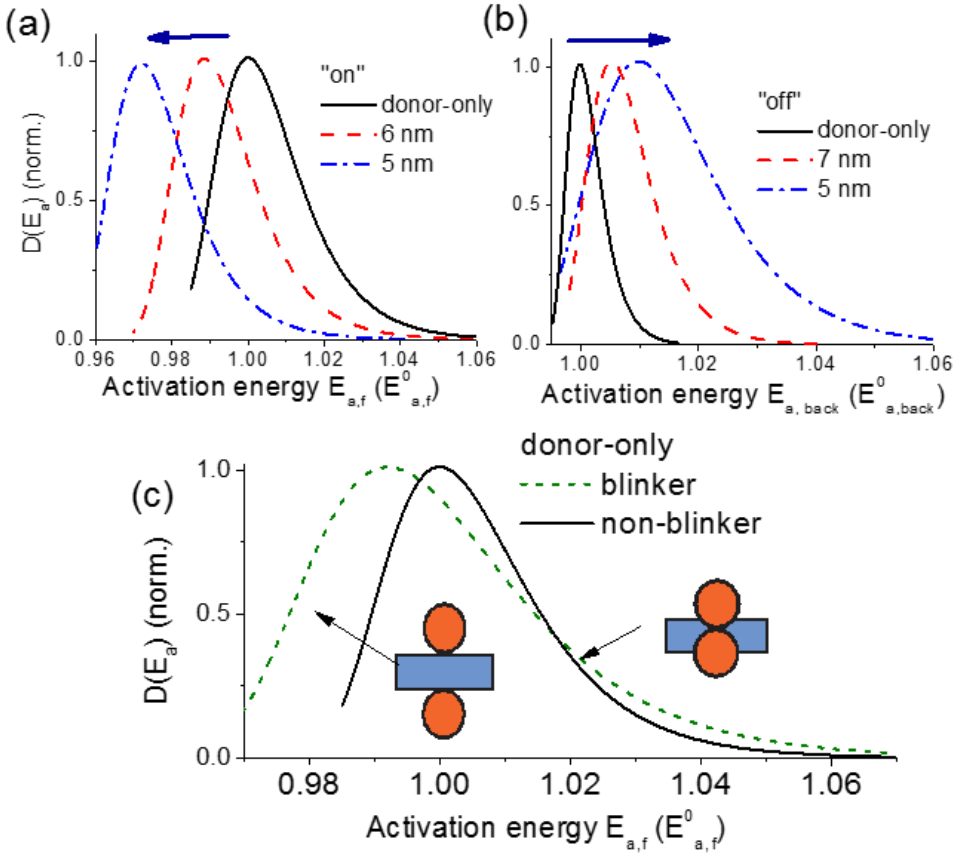

Figure 2.24: Distributions of activation energies for the forward ($E_{a,f}$) (a) and reversed ($E_{a,back}$)(b) reactions of the Pn-TCHS-F8 with singlet oxygen. The scale is set with respect to $E^0_{a,f}$ ($E^0_{a,back}$) which is the most probable activation energy for forward (backward) reactions in donor-only samples. As the acceptors are added, the activation energies for the forward reaction shift to the lower values (a), while those for the reversed reaction shift to the higher values (b). (c) Distributions of $E_{a,f}$ for "non-blinkers" and "blinkers" in donor-only samples. The scale is set with respect to $E^0_{a,f}$, which is the most probable activation energy for forward reactions in "non-blinkers." "Blinkers" exhibit a larger population of molecules with lower activation energies as compared to "non-blinkers." The difference in the distributions is attributed to the differences in the TCHS groups conformations that make the molecule less vulnerable (right) or more vulnerable (left) for the oxygen attacks as schematically shown.

lower values, making the forward reaction, on average, more probable (Fig. 2.24). Fig. 2.24 compares the forward reaction activation energy distributions $D(E_{a,f})$ for the "non-blinkers" and "blinkers" in donor-only samples. In spite of the similarity in their average "on" time durations (Fig. 2.20), the distributions are distinctly different, with a considerably more pronounced contribution of the lower activation energies in the case of "blinkers."

One of the possibilities for the origin of the distributed activation energies in Fig. 2.24 is in the heterogeneity of the conformations of the bulky TCHS side groups when a Pn-TCHS-F8 molecule is incorporated in a PMMA matrix as discussed in the next chapter.[3] Some of these conformations are more protective of the molecular core with respect to reactions with oxygen (acting as an "umbrella") than others, resulting in a slightly higher or lower activation barrier for the reaction. The presence of such side-group-related effects, and protective conformations in particular, is validated by a factor of ~ 2 enhancement of photostability of Pn-TCHS-F8 molecules as compared to Pn-TIPS-F8 molecules dispersed in PMMA again discussed in the next chapter.[3] In this context, the difference observed in the "non-blinkers" and "blinkers" distributions in donor-only samples may suggest that after the oxygen cleavage during the reverse reaction, the TCHS conformations are more randomized, considerably increasing the occurence of less protected configurations. Along the same lines, the presence of acceptors reconfigures the volume available ot the Pn-TCHS-F8 molecule in the blend, which favors less protective TCHS conformations as compared to those in donor-only samples. This makes photo-oxidation more probable and the reversal less probable on average.

2.6.4 Physical Picture

The overall physical picture consistent with observations discussed above is schematically illustrated in Fig. 2.25.[49] In donor-only samples, about 90% of the Pn-TCHS-F8 molecules are "non-blinkers": after they turn "off," they do not turn back "on" again for at least several hundreds of seconds. There are two main possibilities behind this observation: (i) as the parent molecule turns into its EPO, the activation barrier $E_{a,back}$ for the reversal is too high and (ii) the reversal does occur, but the backward reaction generates the singlet oxygen, which then attacks the molecule again before it can be re-excited. The dramatic increase in the percentage of "blinkers" as the acceptors are added ($> 50\%$ in donor-acceptor samples with less than 8 nm-spaced acceptors, Fig. 2.16) indicates a considerable contribution of (ii). It also suggests that the backward reaction is a joint process characterized by a high yield of the singlet oxygen. In donor-acceptor samples with the average acceptor-acceptor separation of < 10 nm, the acceptor molecules located well within the oxygen diffusion length ($L = \sqrt{6D\tau_{O2}} \approx 14$ nm, assuming the diffusion coefficient $D = 1.4 \times 10^{-8}\ cm^2/s$ and the singlet oxygen lifetime $\tau_{O2} = 25\ \mu s$ in PMMA)[51,73] from the Pn-TCHS-F8 molecule, act as singlet oxygen quenchers. They protect the Pn-TCHS-F8 molecule from a repeated reaction to form the EPO and enable the Pn-TCHS-F8 molecule to turn "on" again, thus turning a "non-blinker" into a "blinker." The effect of the singlet oxygen quenching by acceptor molecules is also apparent from the correlations of the "on" and "off" durations of Figs. 2.21 and 2.22. With the exception of rare cases of very long "off" time dura-

tions, the presence of acceptors "erases" the correlation between the "on" and the preceding "off" time duration. This suggests that the "off" event does not make the molecule more vulnerable towards further oxygen attacks (e.g., due to repeated oxidation/reversal reactions resulting in progressively less protective TCHS conformations) in donor-acceptor samples, in contrast to that in donor-only smaples, as can also be appreciated from comparison of the "blinkers" and "non-blinkers" distributions in Figs. 2.24(c) and 2.26.[49] Even though the TCHS groups conformations in the Pn-TCHS-F8 molecules in donor-acceptor samples are on average less protective than those in donor-only samples, making the forward reaction more probable and the reverse reaction less probable, once the reverse reaction does happen, the molecule has a considerably lower probability to immediately react again, until the next photoexcited cycle of the singlet oxygen generation, and is not susceptible towards photo-oxidation during that cycle than before.

Considering the observations above, the following estimates are made. Considering for simplicity a constant value of the rate k_3 of the EPO formation and using the average "on" time $\langle\tau\rangle_{on} = 1/(\Phi_{O2}k_3) = 32$ s (in donor-only samples), one obtains $\Phi_{O2}k_3 \approx 0.03\ s^{-1}$. Given the photobleaching QY (Φ_B) for Pn-TCHS-F8 in PMMA of $\sim 10^6$ and $\Phi_B = \Phi_{O2}k_3\tau_{O2}$, one obtains τ_{O2} of 32 μs (which is comparable with that of $\sim 25\ \mu s$ reported in pristine PMMA[74]). On the other hand, once the reverse reaction (EPO to parent molecule) produces singlet oxygen with a 100% yield, the probability of the repeat forward reaction is then $k_3\tau_{O2} = 0.9$, where 0.9 represents $\sim$ 90% of "non-blinkers" in donor-only samples, which assuming $\tau_{O2} = 32\ \mu s$ yields $k_3 \approx 3 \times 10^4\ s^{-1}$. This yields the probability of the

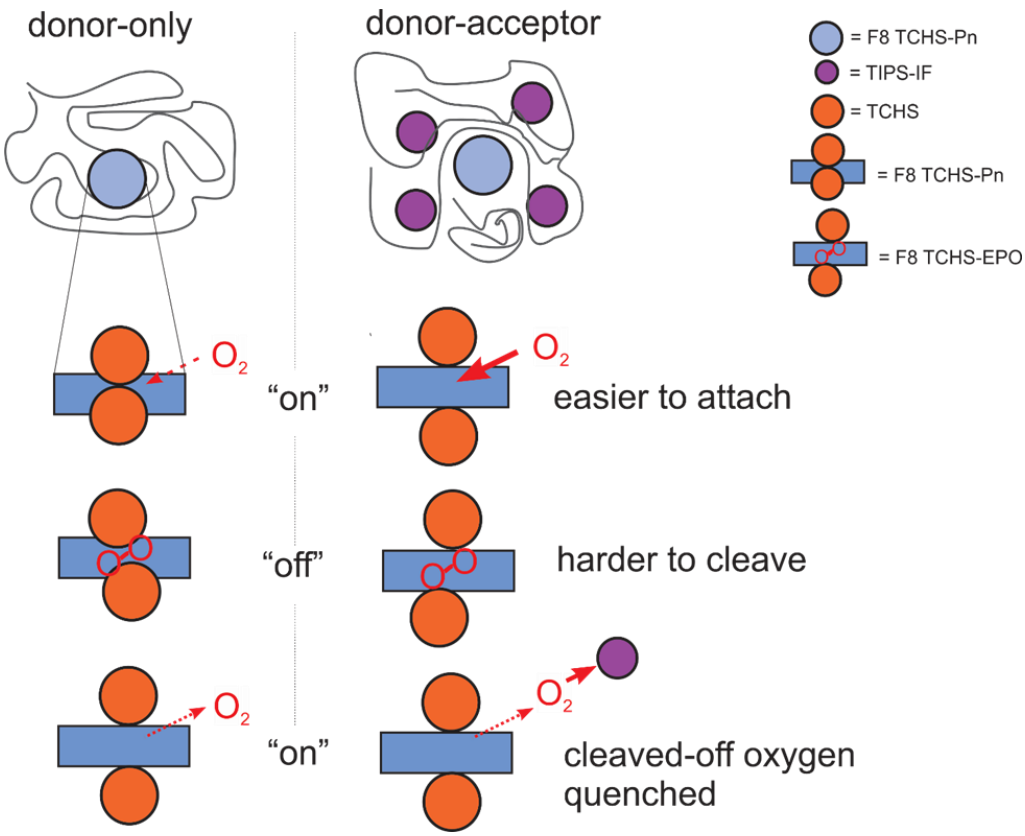

Figure 2.25: Schematics of the effect of acceptor-modified environment on the photophysics of Pn-TCHS-F8 donor molecules. Schematic described in the text.

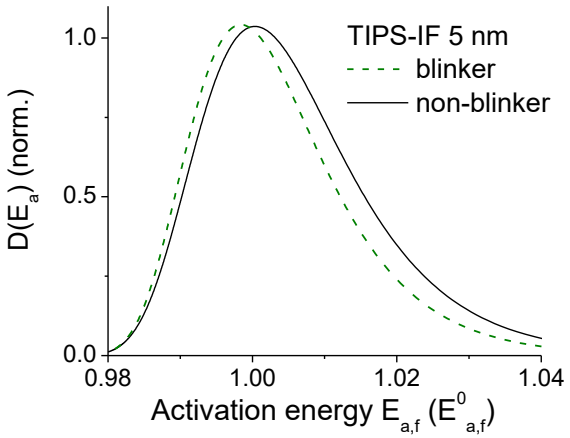

Figure 2.26: Distributions of activation energies for the forward reaction ($E_{a,f}$) for "non-blinkers" and "blinkers" in donor-acceptor samples with 5 nm-spaced IF-TIPS acceptor. The scale is set with respect to $E^0_{a,f}$ which is the most probable activation energy for forward reactions in "non-blinkers." Considerably smaller difference in the distributions is observed in donor-acceptor samples as compared to donor-only sample (Fig. 2.24(c))

.

singlet oxygen generation per absorbed photon Φ_{O2} of 10^{-6}. Such low probability would be consistent with the low adiabatic singlet-triplet energy gap making the self-sensitization a rare process. With these considerations, the most probable activation energy for the forward reaction ($E^0_{a,f}$ in Fig. 2.24(a)) is about $\sim$ 11 kcal/mol, which could correspond to that of the exciplex formation, a precursor to the EPO formation.[35,75] The addition of acceptors increases the rate k_3 due to creating morphology less protective of the Pn-TCHS-F8 reactions with oxygen (resulting in a lower $\langle\tau\rangle_{on}$), but quenches the singlet oxygen as to considerably reduce the singlet oxygen lifetime τ_{O2} which dramatically reduces the probability of the immediate repeat reaction.

2.7 Conclusion

We obtained a molecular-level picture of the photophysics of Pn-TCHS-F8 (donor) molecules in PMMA serving as a probe of evolution of the nanoenvironment due to the addition of IF-TIPS or PCBM acceptor molecules. Reversible photo-oxidation was observed, with the distribution activation energies for both the forward (parent molecule to EPO) and the reverse (EPO to parent molecule) reactions. The acceptor addition shifted the most probable activation energy towards the lower (higher) energies for the forward (reverse) reactions. We attribute these observations to acceptor-induced change in the polymer morphology that imposes the conformation of the TCHS side groups such that the Pn-TCHS-F8 molecule is less

protected from oxygen attacks. The singlet oxygen is produced in high yield in the reverse reaction but is efficiently quenched by acceptors, thus preventing the molecule from the repeat oxygen attack. Therefore, the overall photostability of the donor molecule in the presence of acceptors is determined by an interplay between the acceptor-modified morphology and the ability to quench singlet oxygen. Understanding this interplay and how to slow down the photo-oxidation/enhance the reversibility of photo-oxidation reactions is important for improving stability of organic semiconductor devices. How this interplay is influenced by the particular features of the host polymer, electronic structure, and the side groups of the molecules will be a subject of further investigation.

Chapter 3 Single-Molecule Probes of Molecular Packing

3.1 Introduction

In order to improve device performance with organic semiconductors, it is important to understand the photophysics and molecular packing of these materials in film as these properties influence the efficiency of charge transfer. These properties can be studied at the nanoscale with single molecule fluorescence spectroscopy, which can provide molecular resolution. Functionalized acene and acene-thiophene derivatives (Fig. 3.1) are under investigation as guest molecules within either a polymer or crystalline host matrix with single molecule fluorescence spectroscopy (SMFS). These host matrices were utilized because they limit guest-host interactions, and have been used in devices themselves.

Photophysical properties of these functionalized acene and acene-thiophene derivatives studied include molecular photophysics, molecular packing, and photoinduced intermolecular interactions to better understand processes occurring at the nanoscale level in donor/acceptor (D/A) bulk heterojunctions (BHJs). These derivatives are of interest beacuse they are solution-processable organic semiconductors that have been extensively studied in thin film transistors (TFTs) and solar cells.[76–79] They can also be functionalized to tune either photophysical parame-

ters of the molecule itself or to change the molecular packing (changing the R' or R groups respectively)[6,16,76] to study the local nanoenvironment of the molecular photophysics and packing. Lastly, D/A combinations of these molecules exhibit FRET and/or emissive CT state formation (exciplex),[6–8,38] so these combinations can be used to study nanoscale D/A morphology and effects of the local nanoenvironment on photoinduced D/A interactions[80] through SMFS techniques.

Here, we examine how molecular packing and photophysics (including photodegredation) are affected by the choice of side groups R and by the host. In particular, fluorinated pentacene molecules with three different side groups of various sizes will be studied. Packing and photophysics of these molecules within a polymer host (PMMA) will be compared to a crystalline organic semiconductor host (t-bu BTBTB).

3.2 Materials

Molecules under study as guests embedded in a host matrix for SMFS, include functionalized anthradithiophene (ADT) derivatives with (triethylsilyl)ethynyl (TES) and (triisopropylsilyl)ethynyl (TIPS) side groups (ADT-TES-F and ADT-TIPS-CN) and pentacene (Pn) derviatives with TIPS, NODIPS ((n-octyldiisopropylsilyl)ethynyl), or TCHS ((tricyclohexylsilyl)ethynyl) side groups. Host matrices included a functionalized benzothiophene (BTBTB) derivative t-bu BTBTB (6,12-bis [2-(t-butyl)ethynyl] benzo [1,2-b:4,5-b'] bis(1) benzothiophene) and poly(methyl)methacrylate (PMMA),

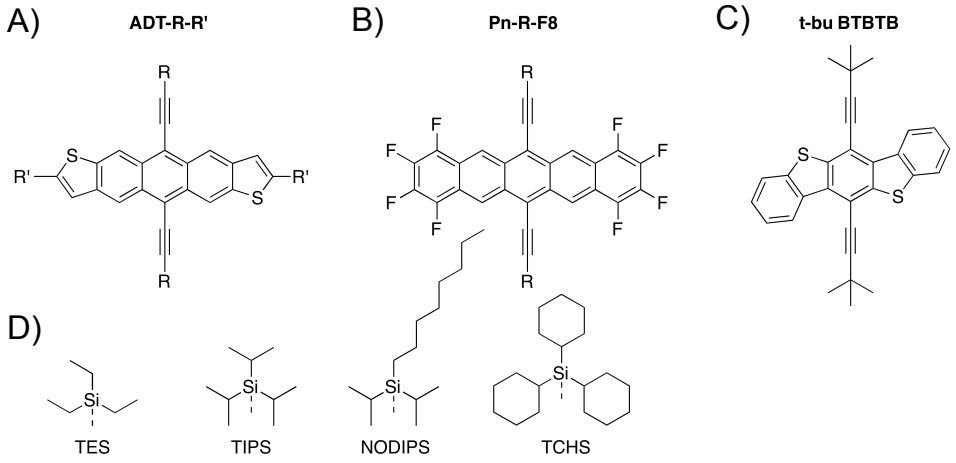

Figure 3.1: Molecular structures of **A)** ADT-R-R', **B)** Pn-R-F8, **C)** t-bu-BTBTB, and **D)** side groups including from left to right, TES, TIPS, NODIPS, and TCHS. Note R indicates side group and R' indicates end group.

which have been used in studies of photoconductivity in ADT-TES-F doped films.[81] These molecules are shown in Fig. 3.1. For thin t-bu BTBTB films, the lowest absorption maximum is 405 nm and the lowest fluorescence maximum in thin t-bu BTBTB films is 415 nm,[82] making t-bu BTBTB a great candidate as a host matrix for SMFS at 532 nm and 633 nm. Functionalized BTBTB derivatives have been used in devices including solution-deposited field effect transistors with functionalized BTBTB derivatives are photoconductive under UV excitation,[82] and have been used in solution-deposited field effect transistors with charge carrier mobilities reaching 1.7 $cm^2/(Vs)$,[83] 7 $cm^2/(Vs)$,[84] and 31.3 $cm^2/(Vs)$,[85] depending on functionalization of the molecule and on device fabrication.

3.3 Experimental Set-Up

3.3.1 Experimental Set-Up: Single Molecule

For single molecule fluorescence spectroscopy experiments, the same experimental set-up and procedures were followed as in Chapter 2. For polarization experiments, a linear polarizer was added as shown in Fig. 3.2. The linear polarizer was set on a rotation stage to the change the polarization of the excitation beam by rotating the polarizer in steps of 22.5°. The excitation light was turned off for $\sim 2-5$ seconds as the polarizer rotated to its next position before the excitation light was turned back on. The same filter combination was used for imaging at 633 nm.[3] For imaging at 532 nm, a 560DCLP (Omega Optical) and HQ537LP (Chroma Tech.) filter combination was used.

At each polarizer setting, the data during the time interval at which the molecule was excited were averaged. Traces from blinking events ($<$ 3% of all traces analyzed) were excluded from analysis.

Again, collection efficiency was determined by

$$\eta_{coll} = \eta_Q T_{ang} T_{opt} T_{filt} \tag{3.1}$$

where η_Q is the quantum efficiency of the camera (85 - 94%, depending on the fluorescence emission spectrum of the molecule), T_{ang} is the angular collection

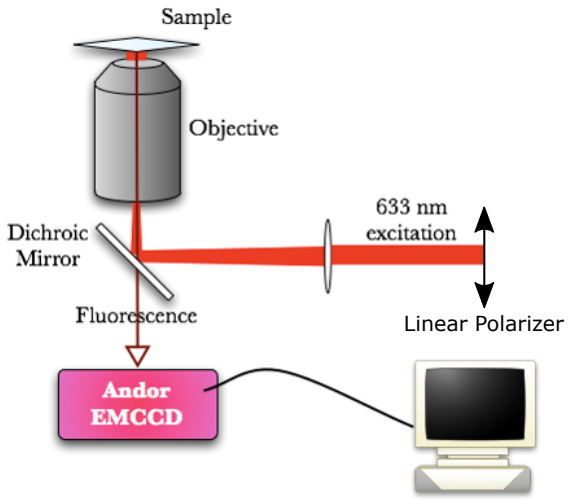

Figure 3.2: Similar experimental set up as Chapter 2 but with added linear polarizer to change the polarization of the excitation beam.

factor, T_{opt} is the collection factor through the microscope optics (62 - 68%), and T_{filt} is the transmission through the dichroic and emission filter (21 - 65%).[3,42] For a single dipole emitter lying parallel to the surface of the cover slip, we estimated T_{ang} to be $\sim$ 34% using Ref. 43. These values give us an estimated collection efficiency of 4.6% for ADT-TES-F, 12.0% for ADT-TIPS-CN, and 10.6% for Pn-R-F8.

To measure the number of photons detected (emitted) by the EMCCD, a conversion factor is necessary using camera settings and the collection efficiency. The number of photons detected can be found through

$$photons_{det} = (counts) \times \frac{ADConversion}{EMGain} \tag{3.2}$$

where $ADConversion$ is the analog to digital conversion determined by camera settings (12.68) and $EMGain$ is the EM gain setting of the camera where it was set to 40x for all samples in PMMA and 100x for all samples in BTBTB. Emitted photons $photons_{em}$ can be calculated from the detected number of photons through

$$photons_{em} = photons_{det} \times \frac{1}{\eta_{coll}} \times \frac{frameConv}{t_{int}} \tag{3.3}$$

where $frameConv$ is the frame conversion rate from the camera (0.16413 s) and t_{int} is the integration time of the camera (0.1 s).

3.3.2 Experimental Set-Up: Bulk

Bulk experiments included absorption, fluorescence, FRET, fluorescence lifetime, photobleaching, and XRD measurements. Optical absorption measurements were conducted with a halogen lamp and a fiber coupled spectrometer (Ocean Optics USB2000). All measurements were performed in solution and referenced off of clean cuvettes with solvent. Absorbance was calculated as $A = -log(I/I_0)$ where I_0 is the incident intensity and I is the trasmitted intensity. The molar absorptivity ϵ was obtained from linear fits of absorbance as a function of concentration c of molecules in toluene solution ($A = \epsilon cl$, where l is length of the cuvette). The absorption cross section was calculated using $\sigma = 2.303\epsilon/N_A$ where N_A is Avogadro's number.[3]

Fluorescence spectra in solution were measured as reported in Ref. 16. For FRET studies, the spectra of "bulk" films of 50/50 D/A in PMMA were measured using a Horiba Custom Fluorog fluorimeter under 490 nm excitation.[3]

Fluorescence lifetime measurements were measured under 470 ps 532 nm exciation (Q-switched frequency-doubled Nd:YAG, 55 kHz, Altechna STA-01-SH-4-MOPA). A time-correlated single photon counting (TCSPC) board (PicoQuant TimeHarp 200) was used with a single photon avalanche photodiode (SPAD - Molecular Photonic Devices) for detection. The instrument response function (IRF) was recorded using scattered light from a frosted glass slide and was 260 ps.[3]

Photobleaching experiments in "bulk" samples with the PMMA host were performed under a 633 nm (532 nm) excitation for Pn-R-F8 (ADT-R-R') with the light intensity (I_λ) of 28 W/cm^2. Considerably higher intensities were necessary to observe real-time photobleaching in samples with the t-bu BTBTB host, which in these samples was carried out at 185 W/cm^2. Fluorescence spectra were collected as a function of time with a fiber coupled spectrometer (Ocean Optics USB2000) and integrated over all emission wavelengths for each time frame, which was 0.5-2 s, depending on the time span of the experiment. For selected samples, the experiment was performed both in air and in vacuum at 10^{-5} Torr, for which the sample was placed in a micro-cryostat (Janis STC-500). The photobleaching dynamics in PMMA were fit with a biexponential function, and the time constant (τ_B) or weighted average of the two time constants ($\tau_T = (a_1\tau_{B1}+a_2\tau_{B2})/(a_1+a_2)$), respec-

tively, was obtained.[42] For the data in the t-bu BTBTB host, single exponential fits were applied.[3]

Photobleaching QYs (Φ_B) were calculated using[42]

$$\Phi_B = \frac{1}{\tau_B \sigma_\lambda I_\lambda / (hc/\lambda)} \tag{3.4}$$

where σ_λ is the absorption cross-section at the wavelength of excitation (λ), I_λ is the excitation intensity, h is the Planck constant, and c is the speed of light. From the photobleaching QY Φ_B and fluorescence QY Φ_F, the total number of photons emitted by the molecule was obtained using $N_{tot} = \Phi_F/\Phi_B$.[3,42]

3.4 Theory

Ref. 43 was followed to estimate the orientation of molecules in film via single molecule fluorescence spectroscopy. As the intensity of emission I_{tot} can be related to the transition dipole moment μ and incoming excitation E by

$$I_{tot} \sim |\mu \bullet \mathbf{E}|^2, \tag{3.5}$$

the angle between the surface normal and transition dipole moment can be estimated by changing the polarization of incoming light. These angles are shown in Fig. 3.3.

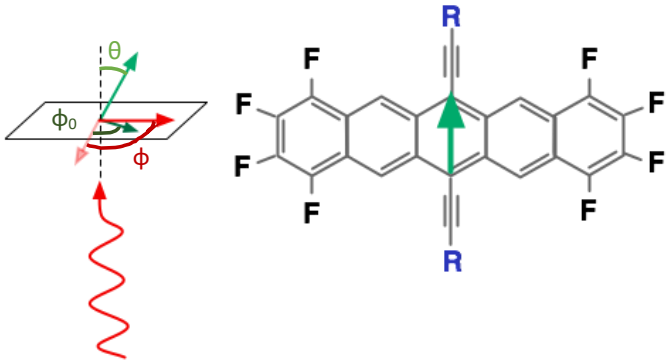

Figure 3.3: *Left:* Cartoon of the transition dipole moment μ (green) (for the S_0-S_1 transition excited with our wavelength of 633 nm) in sample plane. The polarization of the incoming light (red) is varied between $\phi = 0$ and 360 degrees. Differences in the detected photon counts due to variations in coupling between the electric field and transition dipole moment are recorded to determine θ. The in plane dipole angle is represented as ϕ_0. *Right:* Fluorinated pentacene molecule with side groups R. The dipole moment μ is indicated along the short axis of the molecule.

I_{tot} can then be written as

$$I_{tot} = A_0 cos^2(\phi - \phi_0) + I_b \tag{3.6}$$

where ϕ is the angle of the excitation polarization, ϕ_0 is the in plane dipole angle, and I_b is the background intensity level. A_0 is the amplitude of the varying emission as polarization is varied. A_0 depends on the angle θ between the surface normal and dipole moment μ of the guest molecule. The amplitude A_0 can be written as

$$A_0 = I_0 sin^2\theta((K_1 + K_2)sin^2\theta + 2K_3 cos^2\theta) \tag{3.7}$$

where K_1, K_2, and K_3 are parameters which, for our objective, are equal to 0.332, 0.0065, and 0.106, respectively. If $\theta = 90°$, such correction becomes 0.34, which was used to estimate T_{ang} in Eq. 3.1. I_0 is the intensity proportional to the molecule's emission rate. As I_0 is generally not known since it can vary molecule to molecule and vary for the same molecule depending on blinking and rotational diffusion, it was assumed I_0 does not explicitly depend on θ or ϕ.

By fitting experimental data to Eq. 3.6, A_0 and ϕ_0 can be determined. Then, a histogram of A_0 values is generated for each sample type and fit to a Gaussian distribution $\sim exp[-(A_0 - \langle A_0 \rangle)^2/\sigma^2]$ to determine $\langle A_0 \rangle$ and σ. As $\langle A_0 \rangle$ is the ensemble average of the amplitude of Eq. 3.6, by combining with Eq. 3.7 it can be

written as

$$\langle A_0 \rangle = \langle I_0 sin^2\theta((K_1 + K_2)sin^2\theta + 2K_3 cos^2\theta)\rangle. \tag{3.8}$$

While Eq. 3.8 depends on I_0, we assume I_0 is not dependent on θ and ϕ. Then, Eq. 3.8 becomes $\langle sin^2\theta((K_1 + K_2)sin^2\theta + 2K_3 cos^2\theta)\rangle$. This new ensemble average can be calculated after determining the orientational probability distribution $W(\theta, \phi)$. As PMMA is a polymer, it is assumed there is an isotropic distribution of dipole emitters such that $W(\theta, \phi) = 1/(4\pi)$. The probability to find a molecule with orientation within angles θ and $\theta + d\theta$, and ϕ and $\phi + d\phi$ is

$$W(\theta, \phi) = \frac{1}{4\pi} sin\theta d\theta d\phi. \tag{3.9}$$

Now, since $\int_0^{2\pi} d\phi \int_0^{\pi} d\theta \sin\theta \frac{1}{4\pi} = 1$, the ensemble average of $\langle sin^2\theta((K_1 + K_2)sin^2\theta + 2K_3 cos^2\theta)\rangle$ becomes $\frac{1}{4\pi}\int_0^{2\pi} d\phi \int_0^{\pi} d\theta \sin\theta \sin^2\theta((K_1 + K_2)\sin^2\theta + 2K_3\cos^2\theta) = 0.2088$ using Eq. 3.9.

As the t-bu BTBTB host is crystalline, a narrower range of A_0 values is expected (and shown later experimentally). Assuming the distribution of dipole emitters is sharply peaked around $\theta = \theta_0$, the orientational distribution function is

$$W(\theta, \phi) = \frac{1}{4\pi}\delta(cos\theta - cos\theta_0) \tag{3.10}$$

so that now the ensemble average $\langle sin^2\theta((K_1 + K_2)sin^2\theta + 2K_3cos^2\theta)\rangle$ in BTBTB becomes approximately $sin^2\theta_0((K_1 + K_2)sin^2\theta_0 + 2K_3cos^2\theta_0)$.

To calculate the angle θ_0 in the BTBTB host, it can be assumed that the orientational constraints of the host matrix is causing the difference in $\langle A_0\rangle$ values for Pn-R-F8 molecules. Then, using the ratio

$$\frac{\langle A_0\rangle_{PMMA}}{\langle A_0\rangle_{BTBTB}} = \frac{0.2088}{\sin^2\theta_0((K_1 + K_2)\sin^2\theta_0 + 2K_3\cos^2\theta_0)}. \tag{3.11}$$

the angle θ_0 for the molecule in the BTBTB host matrix can be determined.

The orientational distribution function $W(\theta, \phi)$ was adjusted as well to determine how a small but finite width would affect Eq. 3.10. For example, a Gaussian function

$$W(\theta, \phi) = C\exp[-(\theta - \theta_0)^2/\delta^2] \tag{3.12}$$

where θ_0 is the peak, δ is the width, and C is the normalization constant such that $\int_0^{2\pi} d\phi \int_0^{\pi} d\theta \sin\theta W(\theta, \phi) = 1$. The denominator of Eq. 3.11 was then replaced with $\langle\sin^2\theta((K_1+K_2)\sin^2\theta+2K_3\cos^2\theta)\rangle$ using the Gaussian distribution function $W(\theta, \phi)$ to solve the equation and determine θ_0 at various widths δ. When applying these techniques to the following results, it is determined using the delta-function $W(\theta, \phi)$ results in an upper bound for the angle θ_0 since the Gaussian distribution function $W(\theta, \phi)$ results in slightly smaller angles. For example, for Pn-TCHS-F8

in t-bu BTBTB (for which $\theta_0 = 20°$ when a delta-function $W(\theta, \phi)$ is assumed), $\theta_0 = 19°$ and $17.5°$ at $\delta = \theta_0/3$ and $\theta_0/2$, respectively.[3]

3.5 Results

3.5.1 Bulk Results

3.5.1.1 Characterization

Photophysical properties of organic semiconductor molecules used in our studies are summarized in Table 3.1. Optical and fluorescence properties of ADT-R-R' and Pn-R-F8 molecules in toluene solution are shown in Fig. 3.4. They have been studied in detail elsewhere.[6–8,16,81,86] It is important to note that the side group R does not affect the absorption and fluorescence properties of a molecule, but they determined the π-stacking properties of the molecules in the solid state, which considerably affected the (opto)electronic properties of thin films.[16]

Quantum yield Φ was calculated from

$$\Phi = \Phi_R \frac{I}{I_R} \frac{OD_R}{OD} \frac{n^2}{n_R^2} \tag{3.13}$$

where Φ_R is the quantum yield of a reference sample, I and I_R are the integrated fluorescence spectrum for the molecule of interest and reference sample respectively,

Molecule	λ^a_{abs} (nm)	λ^a_{em} (nm)	ϵ^b_{max} ($M^{-1}cm^{-1}$)	Φ^c_F	τ^d (nm) (PMMA)	Φ^e_B (10^5) PMMA	N^f_{tot} (10^5) PMMA	$N^g_{tot,det}$ (10^5) PMMA ($N_{tot,em}$)	$N^h_{tot,det}$ (10^5) t-bu BTBTB
ADT-TES-F	525	532	40,400	0.70 (0.90)	9.4 (12.1)	1.1±0.2	8.2	0.35±0.02 (7.7±0.5)	-
ADT-TIPS-CN	579	588	33,000	0.76 (0.89)	12.7 (14.9)	2.5±0.5	3.6	0.29±0.01 (2.4±0.1)	-
Pn-TIPS-F8	632	644	22,200	0.60(0.80)	9.4 (12.5)	1.9±.05	4.2	0.50±0.05 (4.7±0.5)	0.28±0.03[i]
Pn-NODIPS-F8	632	645	29,200	0.53 (0.67)	6.4 (8.1)	1.2±0.2	5.6	0.40±0.03 (3.8±0.3)	0.38±0.03
Pn-TCHS-F8	635	644	19,400	0.61(0.82)	8.7(11.7)	1.0±0.2	8.2	1.0±0.1 (9.4±0.9)	0.31±0.01

Table 3.1: [a] Wavelengths of lowest enery absorption maximum or of maximal fluorescence emission, measured in dilute toluene solutions, [b] Molar extinction coefficient at the wavelength of maximal absorption λ_{abs} in toluene, [c] Fluorescence QY in toluene. The values in parentheses are from "bulk" samples in PMMA, [d] Fluorescence lifetime in toluene. The values in parentheses are from "bulk" samples in PMMA, [e] Photobleaching QY of Eq. 3.4 obtained in "bulk" samples in PMMA. Error reflects sample-to-sample variation, [f] Total number of emitted photonis in PMMA calculated using $N_{tot} = \Phi_F/\Phi_B$. [g] Mean number of total *detected* photons obtained from single exponential fits to SM histograms (such as that in Fig. 3.11) in the PMMA host. The value in parentheses is the mean number of total photons *emitted* by the molecule calculated from the number of total *detected* photons as $N_{tot,em} = N_{tot,det}/\eta_{coll}$, where η_{coll} is the collection efficiency of Eq. 3.1. [h] Mean number of total *detected* photons obtained from single exponential fits to SM histograms (such as that in Fig. 3.11) in the t-bu BTBTB host. [i] Based on 29 molecules whose trajectories could be reliably analyzed, as compared to, for example, 169 (102) molecules in the case of Pn-TCHS-F8 (Pn-NODIPS-F8) in t-bu BTBTB. This is due to molecular orientation constraints (discussed in the text) which reduced signal-to-noise ratio in the majority of fluorescence trajectories of Pn-TIPS-F8 molecules in the t-bu BTBTB host.

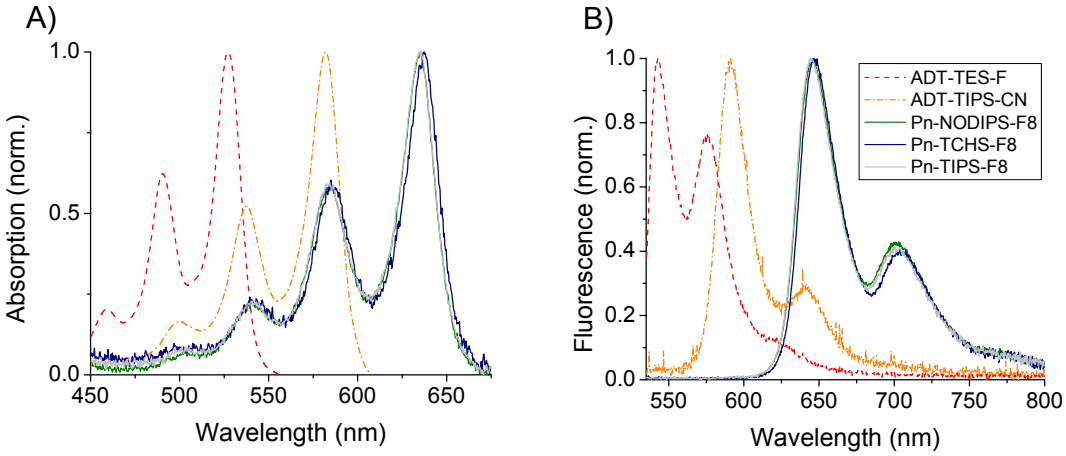

Figure 3.4: A) Normalized absorption and B) normalized fluorescence spectra of ADT-R-R' and Pn-R-F8 molecules in toluene.[3]

OD and OD_R are the measured optical densities at the excitation wavelength for the molecule of interest and reference sample respectively, and n and n_R are the indices of refraction of the solute of the sample of interest and the reference sample.[87] ZL18 was used as a reference to calculate quantum yields presented in Table 3.1.[3] These high fluorescence QYs, Φ_F, obtained in toluene were even higher when immobilized in a solid host, most likely due ot the reduction in non-radiative relaxation as a result of suppressed rotational and torsional motion of the molecule,[88–90] reaching values of 0.7-0.9 in PMMA that are comparable with many commonly used SM fluorophores.[3,42,89]

The photobleaching QY Φ_B which is the probability that a molecule will photobleach when a photon is absorbed, is shown in Table 3.1. Photobleaching experiments were performed for both Pn-TIPS-F8 and ADT-TIPS-CN in PMMA. Experiments were conducted in both vacuum and in air. The fluorescence intensity

as a function of time is shown in Fig. 3.5 as an example. The fluorescence intensity decays quickly in air when compared to vacuum, confirming that photobleaching of these molecules is largely due to a photoinduced reaction with oxygen.[3,49,82,91] In PMMA, the values of Φ_B of (1 - 2.5) $\times 10^{-6}$ obtained in ADT and Pn derivatives were comparable to those of commonly used SMFS fluorophores in a similar environment.[42,89] Under identical illumination conditions, considerably lower photobleaching decay rates of all derivatives studied were observed in the t-bu BTBTB host as compared to PMMA.[82] This could be due to reduced oxygen diffusion in the crystalline t-bu BTBTB host as compared to PMMA, a mechanism similar to the photostability of terrylene molecules embedded in a crystalline film of p-terphenyl.[92] While Φ_B values are as low as (0.6-1.2) $\times 10^{-8}$ for Pn-R-F8 molecules in t-bu BTBTB, as discussed later, the host restricts molecular orientation, which prevents an accurate determination of Φ_B since Eq. 3.4 assumes an absorption cross-section measured in an isotropic medium with randomly oriented molecules.[3]

As shown in Table 3.1, the photostability of Pn-R-F8 molecules in PMMA and t-bu BTBTB hosts also depended on the side group R. Molecules with larger side groups were more photostable than Pn-TIPS-F8 molecules (with smaller side groups). This suggests that large side groups R can help protect molecules from oxygen reaching reactive sites on the molecular backbone such that molecules are less likely to undergo an oxidative reaction. And as seen in the previous chapter, the conformation of side groups is also important to protecting molecules from oxygen. The N_{tot} values reflect this conclusion as well as shown in Table 3.1.[3]

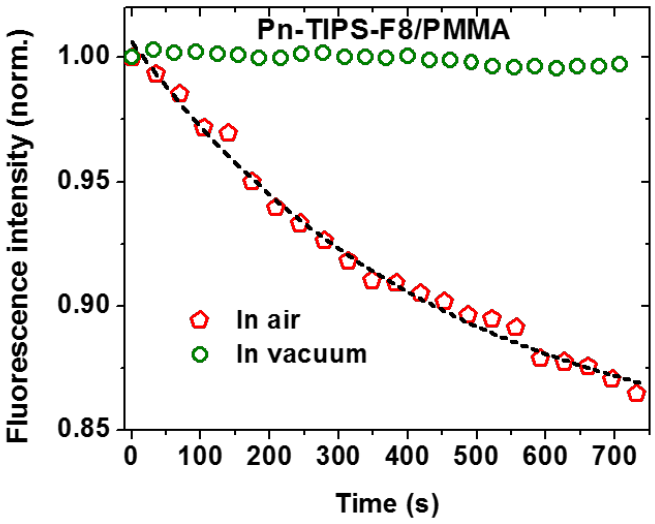

Figure 3.5: Decay of the fluorescence emission due to photobleaching for Pn-TIPS-F8 in PMMA at 0.28 W/cm^2 633 nm illumination in air and in vacuum (at 10^{-5} Torr). Line provides guide for the eye.[3]

Maximum molar extinction coefficients ϵ_{max} were also recalculated based on new absorption data as shown in Table 3.1 where

$$\epsilon_{max} = \frac{OD_{\lambda_{abs,max}}}{OD_{\lambda_{excitation}}}\epsilon_{\lambda} \tag{3.14}$$

and $OD_{\lambda_{abs,max}}$ is the optical density at the wavelength of maximal absorption, $OD_{\lambda_{excitation}}$ is the optical density at the excitation wavelength, and ϵ_{λ} is the molar extinction coefficient at the excitation wavelength calculated previously.

3.5.1.2 FRET

Intermolecular interactions between ADT-TES-F (donor) and ADT-TIPS-CN (acceptor) molecules have been studied[7] and shown FRET or emissive CT state (exciplex) formation depending on the D/A distance. The presence of a spacer such as PMMA has been shown to increase the favorability of FRET.[6,7,86]

Similar observations were made for the ADT-TES-F/Pn-R-F8 (D/A) systems when separated by PMMA as a spacer. Fig. 3.6 shows an example of the fluorescence spectra of donor-only, acceptor-only, and D/A samples in PMMA. In film containing both donor and acceptor, the fluorescence emission from the acceptor was enhanced due to FRET while that of the the donor was reduced. The donor lifetime was also reduced (see inset of Fig. 3.6). FRET radii ranged from 4.2-4.5 nm, and a summary can be found in Table 3.2.[3]

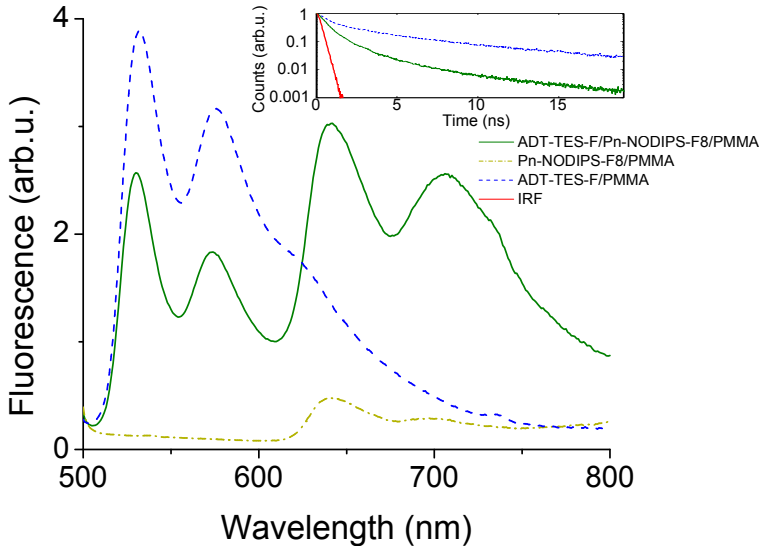

Figure 3.6: Fluorescence spectra of ADT-TES-F in PMMA (donor-only), Pn-NODIPS-F8 in PMMA (acceptor-only), and ADT-TES-F/Pn-NODIPS-F8 in PMMA (donor/acceptor pair) obtained under a 490 nm excitation. Inset shows donor fluorescence lifetime decay obtained in the donor-only sample and donor-acceptor sample at the same average spacing between donor molecules. The instrument response function (IRF) is also included in the inset.[3]

D/A system	Volume of R^a $\mathring{A}^3$	R_0^b nm	λ_{CT}^c nm	τ_{CT}^f ns	$I_{CT}(D/A)/I_{CT}$(D/ADT-TIPS-CN)^h
ADT-TES-F/ADT-TIPS-CN	278.5	4.8[d]	669[d]	20[d]	1
ADT-TES-F/Pn-TIPS-F8	278.5	4.2	723[e]	4.5[e]	0.21± 0.03
ADT-TES-F/Pn-NODIPS-F8	402.5	4.5	723[e]	3.4[e]	0.064±0.004
ADT-TES-F/Pn-TCHS-F8	469.2	4.4	711[e]	2.2[g]	0.021±0.001

Table 3.2: [a] Volume of a side group R of acceptor calculated from cyrstallographic data. From Ref. 6. [b] FRET radius calculated as described in Appendix B. FRET in these D/A systems is observed when the donor and acceptor molecules are separated by a neutral spacer such as PMMA. [c] Wavelength of maximal fluorescence emission from the D/A charge transfer (CT) state. The emissive CT state is observed in these systems when a neutral spacer is removed. [d] From Ref. 7. [e] From Ref. 6. [f] Lifetime of the fluorescence emission from the CT state obtained in ADT-TES-F/ADT-TIPS-CN (2 wt%) or ADT-TES-F/Pn-R-F8 (2 wt%) films. [g] From Ref. 8. [h] Intensity of the CT emission in the ADT-TES-F/Pn-R-F8 (2 wt%) films relative to that in ADT-TES-F/ADT-TIPS-CN (2 wt%) films obtained from integrated spectra of CT emission under same excitation conditions. Error reflects sample-to-sample variation. From Ref. 6.

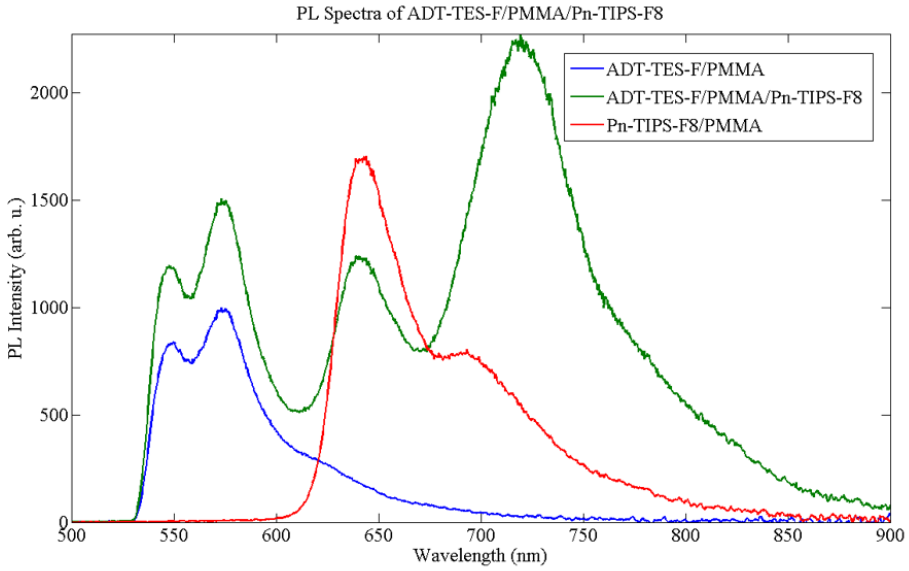

Figure 3.7: Fluorescence spectra of ADT-TES-F in PMMA (donor-only), Pn-NODIPS-F8 in PMMA (acceptor-only), and ADT-TES-F/Pn-NODIPS-F8 in PMMA (donor/acceptor pair) obtained under a 490 nm excitation with 2 nm spacing of the donor and acceptor molecules. Exciplex formation is dominant in the D/A sample, but FRET could be present as well. More precise control of concentrations is needed for FRET to dominate.

The CT state emission depended on the size of the acceptor's R groups. In particular, the CT state was less emissive in the D/A pair with a larger D/A separation due to the larger side-group R on the acceptor molecule.[6] Fig. 3.7 shows an example where the CT state dominates the interaction between donor and acceptor molecules.

The ADT-TES-F/Pn-R-F8 D/A systems were also studied in BTBTB in addition to PMMA at 3 and 5 nm average spacings.

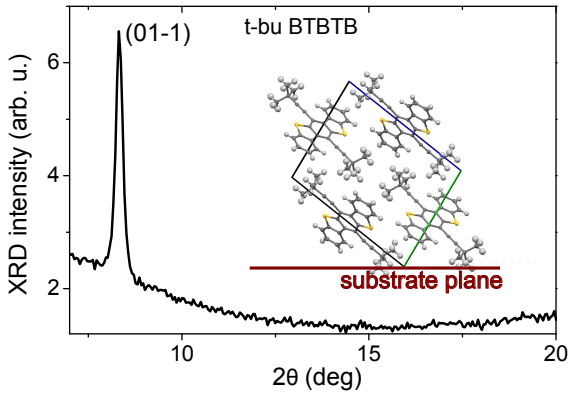

Figure 3.8: XRD results for out-of-plane structures in spin-cast t-bu BTBTB films. Inset shows alignment of the t-bu BTBTB molecules on the substrate consistent with the (0 1 - 1) crystallite orientation as revealed by the XRD. Inset cartoon shows orientiation of molecules on substrate plane.[3]

3.5.1.3 XRD

X-ray diffraction (XRD) was used to confirm the crystalline order of spin-cast t-bu BTBTB films. As shown in Fig. 3.8, these t-bu BTBTB films exhibit crystalline order with a domininant (0 1 -1) crystalline orientation.[3]

3.5.2 Single Molecule Results

3.5.2.1 N_{tot} Calculations

The ADT-R-R' (Pn-R-F8) molecules of Fig. 3.1 were imaged at the single-molecule level in PMMA and t-bu BTBTB hosts under 532 nm (633 nm) wide-field exci-

tation. Fig. 3.9 shows examples of fluorescence time trajectories collected from individual molecules of Pn-R-F8 in PMMA and t-bu BTBTB. In both hosts, up to 80% of molecules did not exhibit blinking, and most blinking molecules only experienced one blinking event before photobleaching as shown in Chapter 2. The total number of detected photons from each molecule was determined by integrating SM time traces such as those in Figs. 3.9 and 3.10 to construct histograms. From this histogram (an example is shown in Fig. 3.11), the mean number of detected photons per molecule $N_{tot,det}$ was calculated by fitting the histogram to a single exponential as described in the previous chapter.

While $N_{tot,det}$ values in Table 3.1 are much lower than N_{tot} calculated from Φ_B, this is to be expected as N_{tot} is the number of emitted photons over the lifetime of a molecule. The number of photons emitted $N_{tot,em}$ was then estimated using $N_{tot,det}$ and the collection efficiency of Eq. 3.1, and yielded values similar to N_{tot}. For example, the SM value of $N_{tot,em}$ of ADT-TES-F in PMMA ($(7.7 \pm 0.5) \times 10^5$) was comparable to the N_{tot} calculated from "bulk" (8.2×10^5).[3]

Both "bulk" N_{tot} and $N_{tot,em}$ of the Pn-TCHS-F8 derivative reveal the highest values of the three Pn-R-F8 derivatives in PMMA where $N_{tot,em}$ reached $(9.4 \pm 0.9) \times 10^5$ photons. This $N_{tot,em}$ is similar to the values of (1.2 - 2.4) $\times$ 10^6 emitted photons per molecule of good SMFS fluorophores such as DCDHF derivatives or rhodamine 6G under similar conditions.[42,89] Again, these $N_{tot,em}$ results indicate greater photostability for molecules with a larger side group R.

In t-bu BTBTB, the SM $N_{tot,det}$ values were similar or slightly lower compared

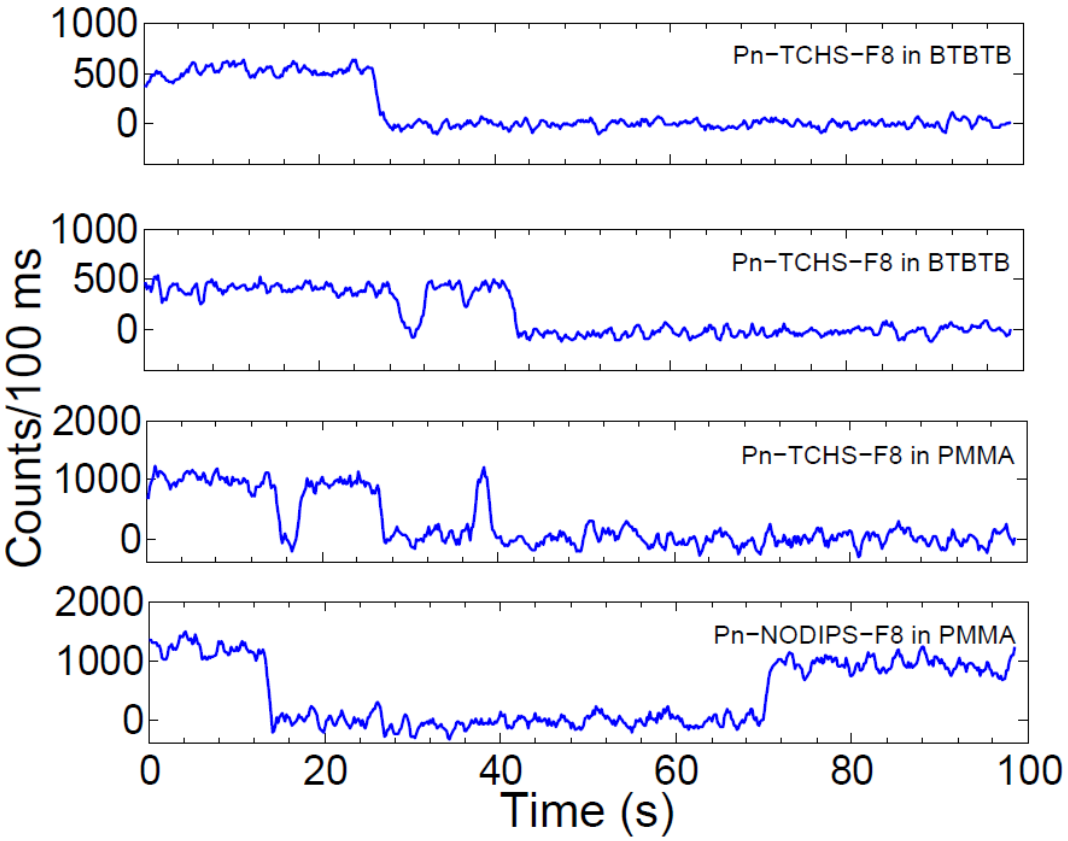

Figure 3.9: Examples of single molecule fluorescence time trajectories for non-blinking molecules (top trace) and for blinking molecules (last three traces). Up to 80% molecules did not exhibit any blinking events (top) in either host. Most of the remaining 20% molecules exhibited one blinking event (second and fourth traces); in rare cases, two (third trace) or three blinking events were observed.[3]

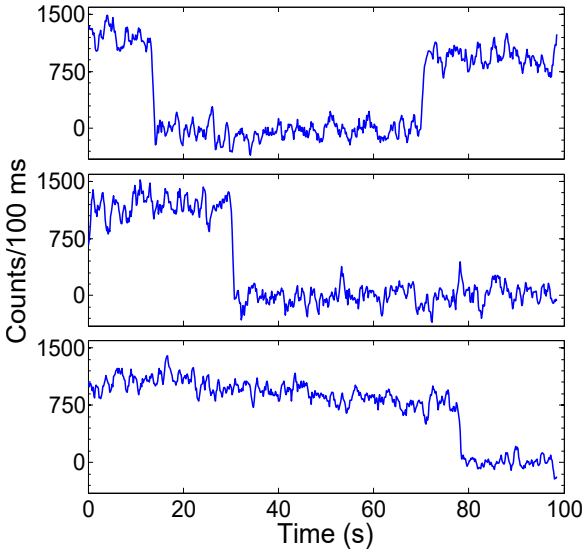

Figure 3.10: Single molecule fluorescence time traces obtained under a wide-field 633 nm excitation at 55 W/cm^2 of Pn-TCHS-F8 in t-bu BTBTB (top) and in PMMA (middle, bottom).[3]

to those in PMMA (Table 3.1) even though photostability was considerably higher for Pn-R-F8 molecules in t-bu BTBTB in the "bulk" compared to PMMA. This phenomena could be explained by how these guest molecules were oriented in their host matrix of PMMA or t-bu BTBTB. For example, if the t-bu BTBTB host constrained guest molecules such that their dipole moments were more closely aligned with the surface normal, the assumption to convert $N_{tot,det}$ to $N_{tot,em}$ would be incorrect, and underestimate $N_{tot,em}$ as the intensity of light collected I is represented in Eq. 3.5.[3] To confirm orientational constraints, the molecules in different host matrices were tested as described in the next section.

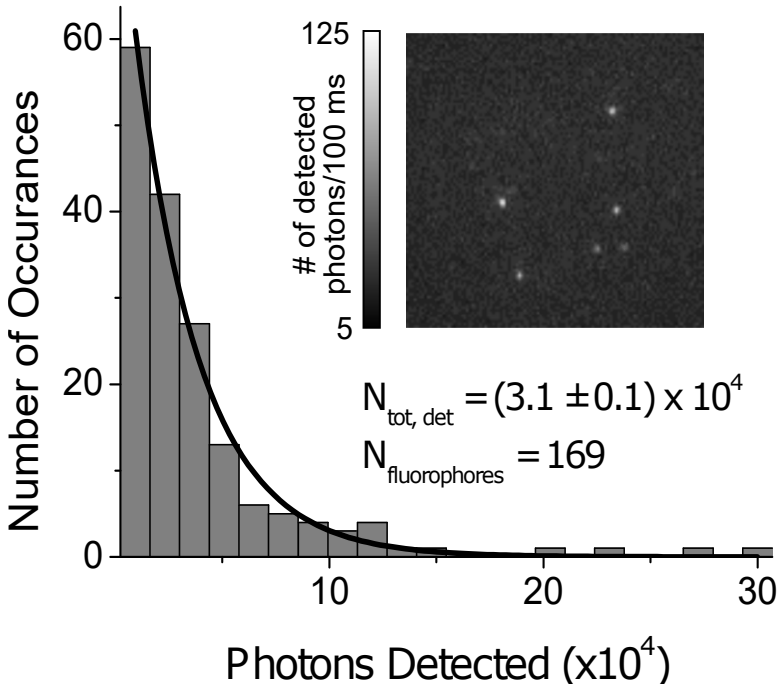

Figure 3.11: Histogram of the total number of detected photons of Pn-TCHS-F8 in t-bu BTBTB from 169 fluorophores. Single-exponential fit and the resulting value of $N_{tot,det}$ are also included. Inset shows a wide-field epi-fluorescence image of Pn-NODIPS-F8 molecules in the t-bu BTBTB host taken under a wide-field 633 nm excitation at 55 W/cm^2.[3]

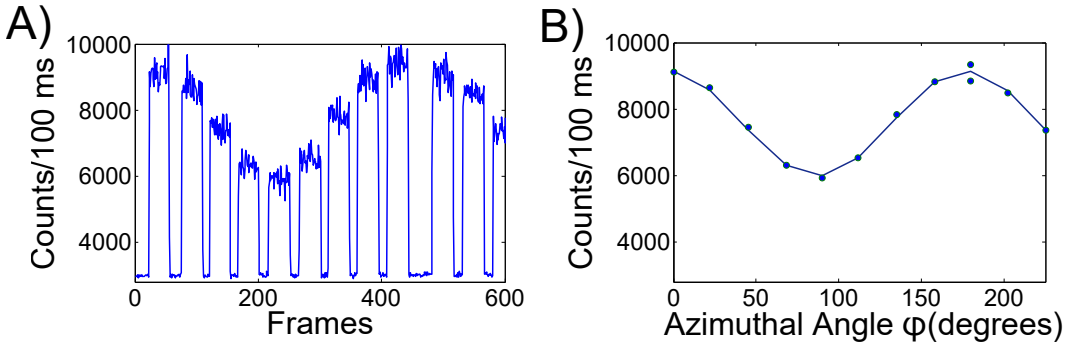

Figure 3.12: A) Raw time trace from a Pn-TIPS-F8 fluorophore in PMMA under 633 nm 28 W/cm^2 excitation with varying polarization. Time intervals with no data indicate where the light is shuttered as the polarizer rotated to the next setting. For most traces, the modulation depth $((I_{min} - I_{max})/(I_{max} - I_b))$ was close to 100%. B) Averaged data from the raw time trace with a fit to Eq. 3.6.[3]

3.5.2.2 Polarization Single Molecule Experiments

To confirm orientational constraints in t-bu BTBTB compared to PMMA, SM emission was studied as a function of excitation polarization in each host matrix with the experimental set-up described earlier. An example of data collected is shown in Fig. 3.12A. As described in Eq. 3.5, modulation in emission was observed as expected. In this case, μ is the transition dipole moment for the $S_0 - S_1$ transition, which in our molecules is aligned with the short axis of the backbone (Fig. 3.13).[93]

Polarization-dependent time traces from 391 (513, 210) molecules of Pn-TCHS-F8 (Pn-NODIPS-F8, Pn-TIPS-F8) in PMMA and 4575 (2991) of Pn-TCHS-F8 (Pn-NODIPS-F8) in t-bu BTBTB were studied. Unfortunately, Pn-TIPS-F8 in t-bu BTBTB did not provide enough signal to produce reliable data for analysis.

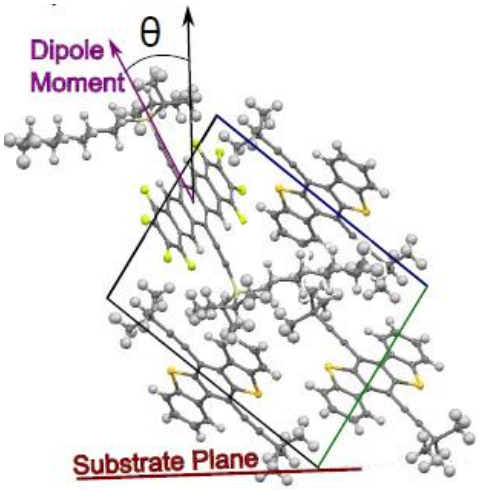

Figure 3.13: Schematic of a Pn-R-F8 molecule packing in the crystalline t-bu BTBTB host inferred from the SM data (here, R = NODIPS).[3]

Most molecules exhibited close to 100% modulation depth such that the modulation amplitude A_0 of Eq. 3.6 is $I_{max} - I_{min}$ with $I_{min} \approx I_b$ as shown in Fig. 3.14. In this case, I_{max} (I_{min}) is the highest (lowest) emission intensity and I_b is the background intensity or intensity after the molecule photobleaches. There was no evidence of rotational jumps in the time traces studied.[3,43]

Following the formalism developed in Ref. 43, the data were fit with Eq. 3.6 as shown in Fig. 3.12 where the phase ϕ_0 and amplitude A_0 parameters were determined. No preferential azimuthal orientation ϕ_0 was observed in either host. Fig. 3.15 shows the distribution of A_0 values obtained for Pn-R-F8 molecules in PMMA and t-bu BTBTB hosts along with Gaussian fits. These fits were used to obtain mean values of A_0 $\langle A_0 \rangle$ and the standard deviations σ of the distributions

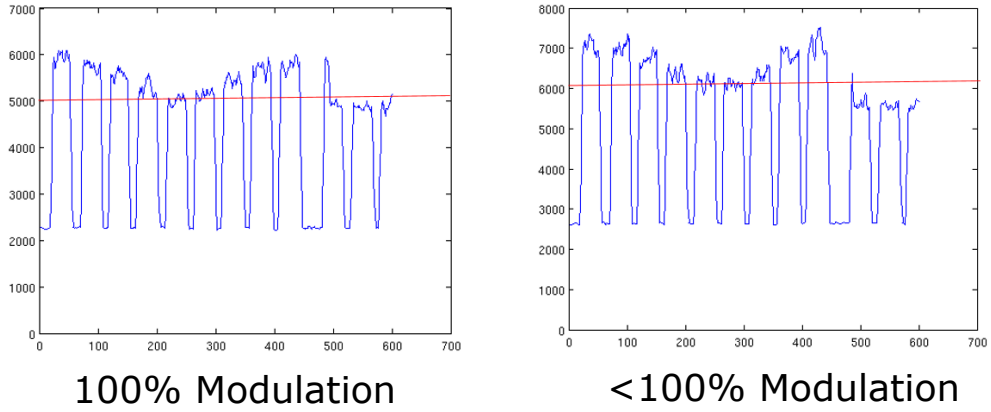

Figure 3.14: Examples of polarization-dependent single molecule data (Pn-NODIPS-F8 in PMMA). Time intervals with no data are from the excitation beam being blocked while the polarization was rotated. **Left:** Example of 100% modulation where I_{min} is simlar to I_b after photobleaching while **Right:** I_{min} is greater than I_b after photobleaching demonstrating less than 100% modulation.

as shown in Table 3.3.[3]

Similar (within 9%) $\langle A_0 \rangle_{PMMA}$ values obtained for all three Pn-R-F8 derivatives are consistent with similar products of molar extinction coefficients and fluorescence QYs of these molecules (Table 3.1) and the absence of orientational constraints in PMMA. The distribution widths σ_{PMMA} reflect a spread in the polar angle θ (Fig. 3.13) and in the inhomogeneity of the local nanoenvironment experienced by a Pn-R-F8 molecule in PMMA. The largest σ_{PMMA} for Pn-TCHS-F8 molecules could indicate the largest degree of inhomogeneity experienced by these molecules as similar spreads of θ would be expected for all Pn-R-F8 derivatives in PMMA.[3]

Considerably smaller values of $\langle A_0 \rangle$ and σ for Pn-R-F8 were observed in the

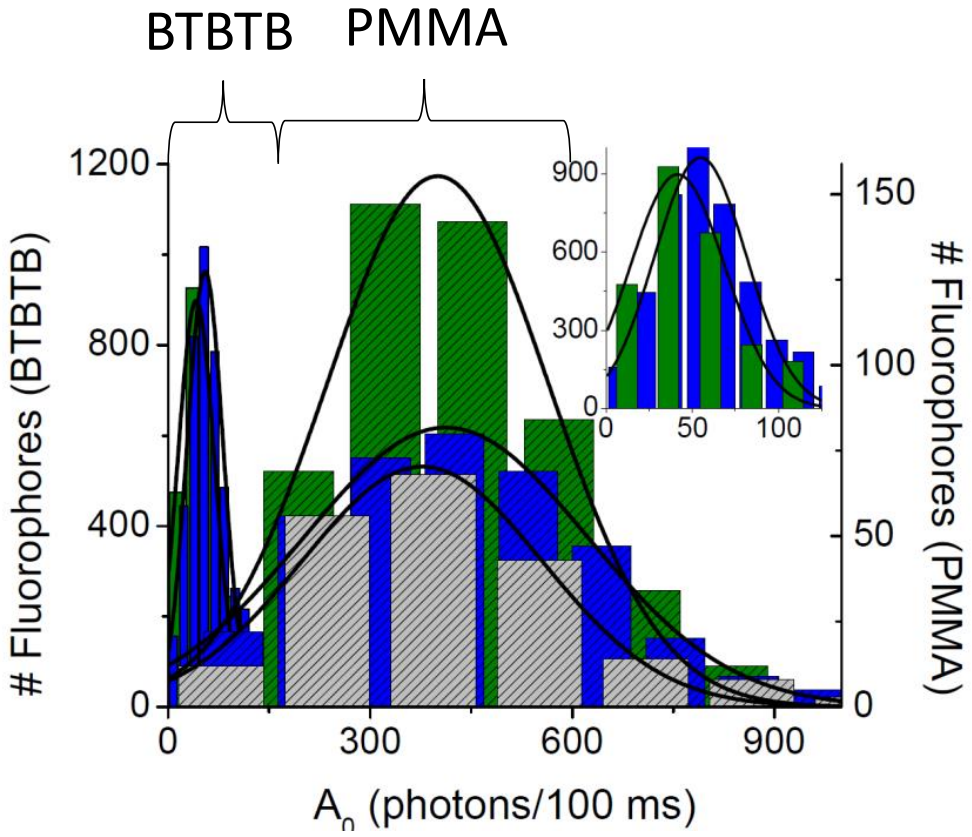

Figure 3.15: Histograms of modulation amplitudes A_0 from fits of the polarization-dependent SM emission data to Eq. 3.6 (blue: Pn-TCHS-F8, green: Pn-NODIPS-F8, gray: Pn-TIPS-F8). Gaussian fits to the histograms are also shown. The inset shows an expanded view of the histograms obtained for Pn-TCHS-F8 and Pn-NODIPS-F8 in the t-bu BTBTB host.[3]

Host Matrix	Side Group R	$\langle A_0 \rangle$ (photons/100 ms)	σ (photons/100 ms)
PMMA	TCHS	410 ± 10	299 ± 3
	NODIPS	401 ± 2	234 ± 5
	TIPS	377 ± 4	250 ± 10
t-bu BTBTB	TCHS	55 ± 1	38 ± 1
	NODIPS	42 ± 9	40 ± 20
	TIPS	N/A	N/A

Table 3.3: These are the mean values of A_0 ($\langle A_0 \rangle$) and standard deviation σ of these distributions obtained from Gaussian fits to the histograms of A_0. Error bars are from the Gaussian fits.[3]

t-bu BTBTB host compared to the PMMA host, which supports the constraints in orientation within the t-bu BTBTB host matrix. From Eq. 3.6, A_0 depends on the polar angle θ between the transition dipole moment of the molecule and substrate normal and a correction due to the polarization mixing in the high-NA objective. There is no evidence of host-guest interactions quenching guest fluorescence[94] in the t-bu BTBTB host, the considerably lower values of $\langle A_0 \rangle_{BTBTB}$ and σ_{BTBTB} compared to those in PMMA (Fig. 3.15) can be attributed to Pn-R-F8 molecule orientations constrained by the t-bu BTBTB host to small polar angles (Fig. 3.13).[3,92]

To estimate the angle at which molecules were oriented in t-bu BTBTB θ, an isotropic orientation of Pn-R-F8 molecules in PMMA was assumed. An upper bound θ_0 was estimated in the t-bu BTBTB host for Pn-R-F8 molecules using $\langle A_0 \rangle_{PMMA} / \langle A_0 \rangle_{BTBTB}$ ratios. These estimates yielded $\theta_0 = 20^\circ \pm 1^\circ$ and $18^\circ \pm 2^\circ$ for Pn-TCHS-F8 and Pn-NODIPS-F8 respectively. Since $\langle A_0 \rangle_{BTBTB}$ for Pn-TIPS-F8 molecules was at or below the highest level of background variation with the

incident polarization $A_{0,b}$, sinilar analysis using $\langle A_0 \rangle_{BTBTB} = A_{0,b}$ revealed an upper bound of $\theta_0 \approx 12°$. As this angle θ_0 is much lower than that of Pn-NODIPS-F8 and Pn-TCHS-F8 in the t-bu BTBTB host, this may suggest that given a larger free volume (as TIPS is a much smaller side group as shown in Table 3.2), the Pn-R-F8 molecule constrained by the crystalline t-bu BTBTB host prefers orientation such that its transition dipole moment is nearly parallel to the substrate normal.[3]

3.6 Conclusion

Photophysical properties of functionalized organic semiconductor molecules were characterized for SMFS studies. All derivatives studied were imaged on the single molecule level in a crystalline organic semiconductor (t-bu BTBTB) and polymer (PMMA) host to investigate changes in the local nanoenvironment and molecular packing. Molecules with larger side groups were found to be more photostable, and molecules within PMMA were found to emit a total number of photons similar to that of a standard SMFS fluorophore. The t-bu BTBTB host put orientational constraints on guest molecules depending on the side group R.

For future studies, functionalization of t-bu BTBTB could be studied to achieve different types of packing with a variety of guest molecules to better understand the formation and properties of organic semiconductor bulk heterojunctions.

Chapter 4 Optical Tweezers-based Probe of Charge Transfer

4.1 Introduction

Most organic semiconductor applications rely on the material's conductive or photoconductive properties.[95] Therefore it is important to understand processes of charge carrier generation and charge transfer, which depend on the dielectric properties of local nanoenvironment. Current techniques require materials to be incorporated into devices, where the surrounding environment of the device cannot be varied systematically. Our goal is to develop a non-contact optical tweezers-based method to measure the efficiency of charge carrier generation and charge transfer in organic semiconductors, at nanoscales, with a single charge resolution, and in systematically varying environments.

The first single beam optical traps were made at AT&T[96] and the first three-dimensional trap was made in 1986 by Ashkin.[5] Optical tweezers are ideal for noninvasive micromanipulation and mechanical measurements.[27,97,98] They can manipulate objects with lengths ranging from tens of nanometers to hundreds of micrometers allowing optical tweezers to manipulate cells, organelles and other larger molecules.[99] Optical tweezers can measure forces on the order of femtonewtons to nanonewtons and on time scales on the the order of microseconds.[96] In

addition to biological applications, there are also uses for the physics community. Optical tweezers can be used to directly measure macromolecular interactions in solution where there are like-charged colloidal particles for statistical mechanics. Another experiment with optical tweezers found the second law of thermodynamics to not always hold true.[96]

Optical tweezers have many applications both by themselves and combined with other techniques. In general, there are many biology applications such as measuring tensions or trapping objects noninvasively through cell walls. For example, Ashkin and Dziedzic used optical tweezers to take membranes inside plant cells and pull out their viscoelastic filaments thereby altering the structure of the cell. Kuo and Sheetz attached spheres to microtubules they wanted to study. The spheres served as an anchor as they were able to trap the attached sphere and then estimate the force of kinesin on microtubules.[27]

It is also possible to build with optical tweezers by modifying an existing structure. This process is achieved by placing dielectric spheres in an existing structure and filling the remaining gaps with a high index material. The optical tweezers can then be used to dissolve the spheres away by heating and damaging the spheres due to large flux.[27,96]

There are many variations on optical tweezers including optical scissors or scalpels, nanometric optical tweezers, optical vortices, and magneto-optical tweezers. Optical scalpels or scissors use spatially resolved photo-oxidation of biological materials[96] and have been used to study the movement of chromosomes during

mitosis.[27] Nanometric optical tweezers trap particles by concentrating optical energy using surface plasmon resonance at nanoprobes. This allows the trapping of particles that are on the order of nanometers or smaller if the particles are fluorescent.[99]

Ring-like optical traps that exert torques and forces are called optical vortices or optical spanners. A photon in a helical mode has both orbital and spin angular momenta. These traps are good for learning about photon spin and angular momenta.[96] While optical tweezers are characterized by 3 stiffness constants (one constant per "real" axis), optical vortices do not have "real" axes. The trapping stability of optical vortices depends on the damping medium in addition to the gradient force.[28]

Scanned optical tweezers allow the trapping of multiple particles. They are similar to a regular optical tweezer trap, but the light that enters the objective is scanned at different angles to create multiple traps. However, this scanning technique limits the patterns in which particles can be trapped and is limited by the scanning time. Another method is where the image is focused on a diffractive beam splitter at the image point to create multiple traps. The beam splitter can be a computer generated hologram to create holographic optical tweezers. An array of traps could be useful for sorting particles and act as a sieve.[96]

Roberts et al. reported an optical tweezers based technique to measure the surface charge of PMMA microspheres suspended in dodecane by applying a sinusoidal electric field. They were able to measure the surface charge of these

spheres with an uncertainty of $0.25e$ where e is an elementary charge.[30] A few years later, Beunis et al. demonstrated the surface charge of PMMA microspheres suspended in dodocane could be measured over time to study the interaction at the solid-liquid interface.[31]

4.2 Theory

4.2.1 Mie and Rayleigh Frameworks

Optical tweezers use a highly focused laser beam to trap particles that are suspended in a medium. When a dielectric particle is close to the focus of the laser, the particle is pulled into the trap. Depending on the relationship between the wavelength of trapping light and the particle size, particle trapping can be described by one of two frameworks.

In the Mie framework, the particle is larger than the wavelength of light, and the particle or bead can be trapped when the bead is close enough to the focus of the laser (see Fig. 4.1). The incoming light hits the particle and refracts through the particle as if the particle were another lens. The refracted light causes an overall change in momentum for that light. The change in momentum creates a force on the light. Due to Newton's third law, there is an equal and opposite force on the particle, which pushes the particle back towards the focus of the laser. This principle works both when the particle is misaligned from the focus in the

horizontal and vertical directions. Also, since the intensity of the light beam is a Gaussian, the individual forces will not all be of the same magnitude, which also contributes to the bead moving back to the center of the trap. The force due to the change in momentum of light is called the gradient force.[5]

It is important that the index of refraction of the trapped particle has a higher index of refraction than the suspension medium. This condition allows the light to refract in the correct direction and create a force on the particle towards the focus of the laser. For example, an air bubble in a medium, such as water, would not be trapped by the tweezer set up. Instead the bubble would be pushed to a less intense region of the laser beam since the index of refraction for air is less than the index of refraction of water.[27] In addition to refraction of light, a small amount of light is reflected off the particle creating a scattering force[5] which can be overcome with a sharper focus.[27] In the Mie framework, it is important to consider the size of the particles. Since larger particles absorb more light, larger particles generate more thermal forces that could affect trap stiffness.[100]

In the Rayleigh framework, the wavelength of light is much larger than the bead. In this case, the bead can be approximated to a dipole. The dipole then feels a force from the gradient in electric field from the laser, which pushes the bead back to the center. The force can be represented as

$$< \vec{F} >= \frac{\alpha}{2} \nabla < \vec{E}^2 >, \tag{4.1}$$

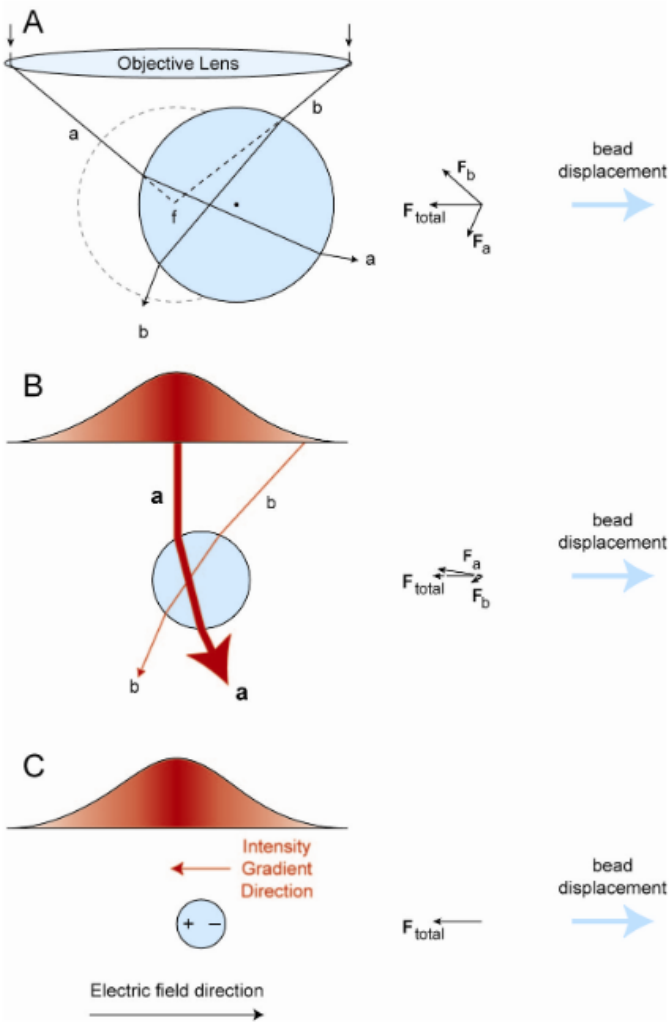

Figure 4.1: (A) The dielectric bead is displaced horizontally from the focus of the optical trap. In this case, the wavelength of light is smaller than the size of the dielectric bead. The light refracts through the bead, and the change in momentum of the light creates a force on the light and force on the bead in the opposite direction, which pushes the bead to the left back towards the focus. (B) The magnitudes of refraction vary through the bead since the laser beam is a Gaussian. (C) When the wavelength of light is larger than the bead, the bead can then be approximated as an electric dipole that gets trapped in the beam. Figure from 5.

where α is the polarizability.[5]

4.2.2 Measuring Trap Stiffness

Trap stiffness k defines the strength of an optical tweezers trap. It is analogous to the spring constant of a spring. As the trapped particle moves due to Brownian motion, the trap constantly needs to pull the particle back to the center of the trap. As with a spring's ability to pull an object back towards equilibrium is based on its spring constant, the ability of optical tweezers to pull a particle back to the center of the laser beam focus is based on its trap's stiffness. The stiffer the trap, the harder it is for the particle to fall out of the trap. With the position of the trapped particle and the trap stiffness of the tweezers, one can measure the movement and forces exerted on the particle.[101]

For this work, the trap stiffness in the x-y plane was calculated by applying three analysis methods to the data.[102] In a stable unperturbed trap, the trap stiffness values extracted from each method are equal within approximately 10-15%. The methods included applying the equipartition theorem to the variance of the sphere's motion in the trap, performing a Gaussian fit to a histogram of the sphere's position in the trap, and obtaining the corner frequency of the power spectrum of the suppressed Brownian motion of the sphere.

With the equipartition theorem, the energy due to the Brownian motion is

$$E_{Brownian} = \frac{1}{2} k_B T, \tag{4.2}$$

and the energy due to a spring is

$$E_{spring} = \frac{1}{2} k \Delta x^2, \tag{4.3}$$

where k is the spring constant. Combining Eq. 4.2 and Eq. 4.3, the spring constant is

$$k = \frac{< x^2 >}{k_B T}. \tag{4.4}$$

Using Eq. 4.4, the trap stiffness can be calculated, since it is simple to find the average location of the particle in the trap (see Fig. 4.2).

The normal distribution method determines the trap stiffness of an optical trap by fitting a Gaussian $f(x)$ to a histogram of the position measurements where

$$f(x) = A e^{-(\frac{x - x_c}{\sqrt{2}\sigma})^2}. \tag{4.5}$$

The trap stiffness is then determined by the standard deviation σ of the distribution where

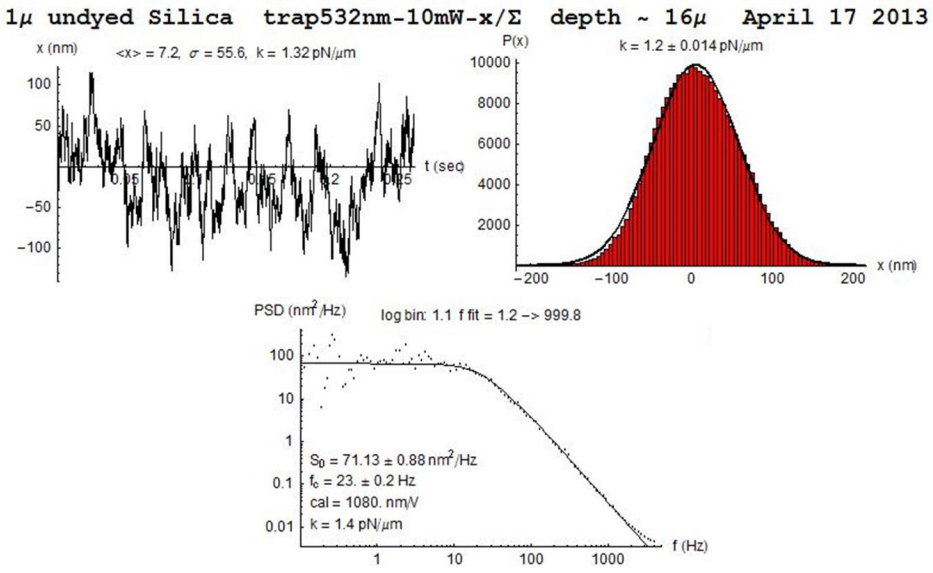

Figure 4.2: The trap stiffness k for a trapped silica sphere suspended in MilliQ water is calculated with three different methods including the A) equipartition method, B) histogram method, and C) power spectral density method.

$$\sigma^2 = \frac{k_B T}{k} \tag{4.6}$$

and k is the trap stiffness.

Finally, the power spectrum can be used to calculate trap stiffness. This method is the best method to measure trap stiffness when a sinusoidal electric field is applied. A massless, damped oscillator due to Brownian motion can be represented by the equation of motion

$$\beta \dot{x} + kx = F(t), \tag{4.7}$$

where the drag coefficient $\beta = 6\pi\eta r$ depends on the viscosity η of the surrounding fluid of the particle and the radius of the bead r. The power spectrum can be written

$$|\tilde{x}(f)|^2 = \frac{k_B T}{\pi^2 \beta[(\frac{k}{2\pi\beta})^2 + f^2]}, \tag{4.8}$$

where $\tilde{x}(f)$ is the position of the particle as a function of frequency. The corner frequency f_c is then found to be $f_c = k/2\pi\beta$, which makes the spring constant for the trap $k = 2\pi\beta f_c$.[5] The corner frequency is the frequency at which the Brownian motion at lower frequencies begins to become suppressed.

4.2.3 Charge Measurement Theory

While measuring trap stiffness provides a powerful tool to measure forces imparted on objects, placing an optically trapped sphere in an oscillating electric field can be used as a tool to probe surface charge of the trapped sphere.

Applying an AC electric field to a trapped sphere introduces an electric field-dependent term in the power spectrum from Eq. (4.8) to become

$$|\tilde{x}(f)^2| = \frac{k_B T}{\pi^2 \beta (f_c^2 + f^2)} + \frac{k_B T \gamma^2}{2k}[\delta(f - f_{AC}) + \delta(f + f_{AC})], \tag{4.9}$$

where γ^2 is the scaled ratio of the mean square periodic and Brownian forces and can be calculated from

$$P_{AC} = \int_{-\infty}^{\infty} |\tilde{x}(f)^2|_E df = \frac{k_B T}{k}\gamma^2, \tag{4.10}$$

where $|\tilde{x}(f)^2|_E$ is the power spectrum due to the applied electric field.[30] As shown in Ref. 30 the effective charge Z_{eff} on a sphere can be calculated with

$$e|Z_{eff}| = \frac{\gamma\beta}{E}\sqrt{\frac{2k_B T}{k}((2\pi f_{AC})^2 + (k/\beta))}, \tag{4.11}$$

where e is the charge of an electron, E is the applied electric field, and f_{AC} is the driving frequency of the electric field. This method has an estimated sensitivity

of $0.25e$ where e is the charge of one electron![30] The MATLAB script to calculate the surface charge of a trapped sphere using this method can be found in Appendix C.

This method can be used to resolve measuring surface charge as a function of time by making these measurements every 40 ms. However, this method employs a weaker electric field and lower driving frequency (on the order of 100 Hz). With these conditions, the resolution of our experiment can be calculated using error propagation[103] with

$$\delta Z = \sqrt{\left(\frac{\delta Z}{\delta a}\delta a\right)^2 + \left(\frac{\delta Z}{\delta V}\delta V\right)^2 + \left(\frac{\delta Z}{\delta d}\delta d\right)^2 + \left(\frac{\delta Z}{\delta P_{AC}}\delta P_{AC}\right)^2 + \left(\frac{\delta Z}{\delta k}\delta k\right)^2 + \left(\frac{\delta Z}{\delta f_{AC}}\delta f_{AC}\right)^2 + \left(\frac{\delta Z}{\delta f_c}\delta f_c\right)^2} \quad (4.12)$$

where the partial derivatives are with respect to Eq. 4.11 and a is the radius of a trapped sphere and d is the separation between electrodes. These partial derivatives are as follows:

$$\frac{\delta Z}{\delta a} = \frac{Z}{a} \quad (4.13)$$

$$\frac{\delta Z}{\delta V} = \frac{-Z}{V} \quad (4.14)$$

$$\frac{\delta Z}{\delta d} = \frac{Z}{d} \tag{4.15}$$

$$\frac{\delta Z}{\delta P_{AC}} = \frac{-Z}{2P_{AC}} \tag{4.16}$$

$$\frac{\delta Z}{\delta k} = \frac{-Z}{k} \tag{4.17}$$

$$\frac{\delta Z}{\delta f} = \frac{6\pi\eta a}{Ee}\frac{k_B T}{k}\Big[P_{AC}\Big((2\pi f_{AC})^2 + (2\pi f_c)^2\Big)\Big]^{-1/2} 4\sqrt{2}\pi^2 f \tag{4.18}$$

where in the last equation, f is either f_c or f_{AC}. To give an example of error propagation, the following estimations were made: $\delta a = 0.01\ \mu m$, $\delta V = 0.01\ V$, $\delta d = 5\ \mu m$, $\delta P_{AC} = 0.1 P_{AC}$ (10% of P_{AC}), $\delta k = 0.08\ pN/\mu m$, $\delta f_{AC} = 1\ Hz$, and $\delta f_0 = 1\ Hz$ where δk and δf_c are calculated from the standard deviation of multiple runs. Then, $\delta Z_{eff} = 19.8$ for $Z_{eff} = 180$ charges. In terms of surface charge density, this gives an error of 6.3 $e/\mu m^2$.

A more effective method to measure the (dis)charging dynamics of a trapped sphere uses a much higher sampling frequency, higher applied electric field, and higher driving frequency. By increasing the sampling frequency, electric field strength, and driving frequency, the charge resolution improves greatly. The effective charge can be calculated using

$$|Z_{eff}| = \frac{2\beta f_{s,Q}}{E}\left(2\pi f_c Re(|\tilde{x}(f)^2|_E) + 2\pi f_{AC} Im(|\tilde{x}(f)^2|_E)\right), \tag{4.19}$$

where $f_{s,Q}$ is the sampling rate of overlapping windows of charge measurements within a data set.[31] To measure the effective charge with this method, we increased our sampling frequency from 10kHz to 20 kHz and used f_{AC}=1 kHz (from $\sim$ 100 Hz) and $f_{s,Q}$=4.88 Hz.

4.3 Experiment

Four types of experiments were performed to develop a new tool to investigate transfer of charge from donor to acceptor materials using optical tweezers as outlined in Fig. 4.3. The first experiment compares surface charge measurements of plain spheres to the literature. Next, a coating, with for example an organic semiconductor material, is applied to the spheres and the surface charge is measured during simultaneous photoexcitation. The third experiment placed plain spheres in solution with acceptor material to study the movement of surface charge with photoexcitation. Lastly, donor coated spheres and acceptor materials in solution were combined to measure the charging dynamics under photoexcitation. In addition to measuring surface charge, the PL of coated spheres was monitored with a spectrometer.

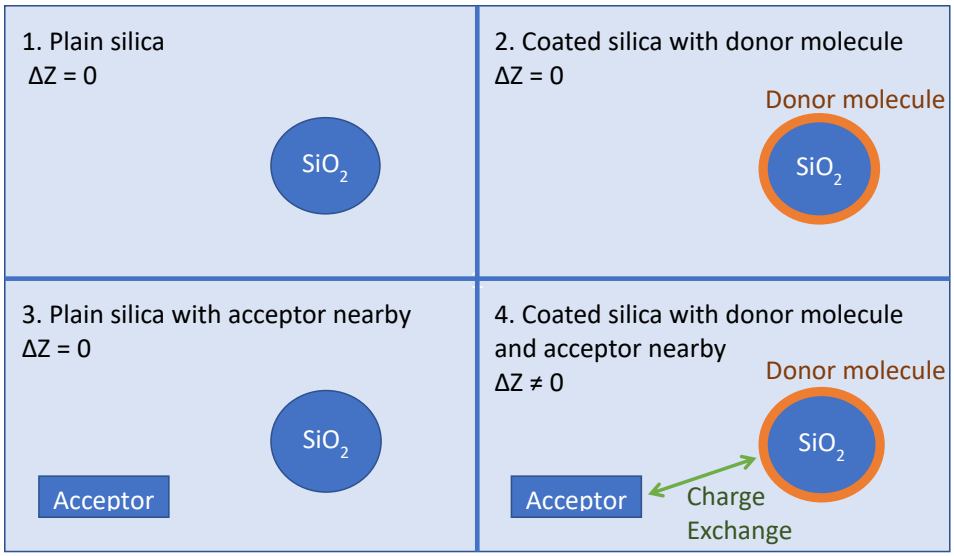

Figure 4.3: Four types of experiments were carried out. Clockwise from the top left, 1) plain spheres, 2) coated spheres, 3) plain spheres in a doped solution, and 4) coated spheres in a doped solution were studied and the surface charge of the spheres was measured.

4.3.1 Materials

For our studies, we chose a fluorinated anthradithiophene (ADT) derivative functionalized with (triethylsilyl)ethynyl (TES) side groups, ADT-TES-F, a cyano-substituted ADT derivative functionalized with (triisopropylsilyl)ethynyl (TIPS) side groups, ADT-TIPS-CN (Fig. 4.4), and a fluorinated pentacene (Pn) derivative functionalized with TIPS groups (Pn-TIPS-F8, Fig. 4.4). The ADT-TES-F derivative has shown TFT charge carrier (hole) mobilities of over 1.5 $cm^2/(Vs)$,[104] fast charge carrier photogeneration,[70,105] and high photoconductivity under continuous wave (cw) illumination.[16] The ADT-TIPS-CN and Pn-TIPS-F8 derivatives have been used as acceptors in donor-acceptor (D/A) bulk heterojunctions (BHJs) with polymer or ADT-TES-F donors.[6–8,38,79,86] The ADT-TES-F/ADT-TIPS-CN and ADT-TES-F/Pn-TIPS-F8 blends exhibit strong exciplex formation with the peak energy corresponding to the gap between the HOMO of the donor to the LUMO of the acceptor, which yields 1.86 eV (668 nm) and 1.72 eV (723 nm), respectively.[6,7] We chose millipore water and toluene for our initial set of experiments because they did not compromise the quality of the coating and because they provided environments with considerably different dielectric permittivity (ϵ = 80 and 2.38, respectively).

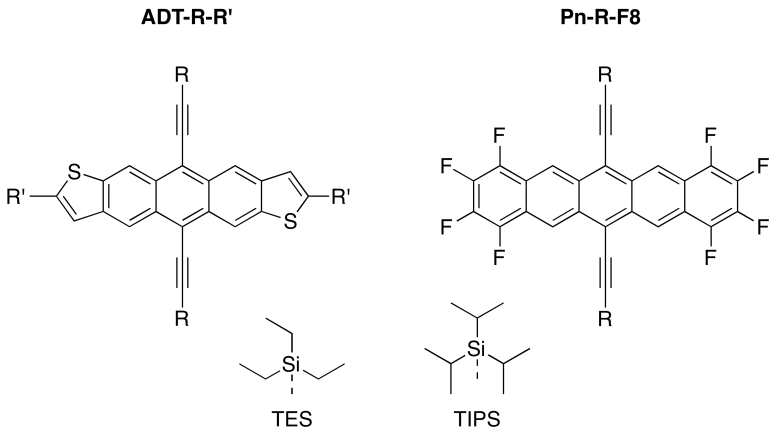

Figure 4.4: Molecular structures of ADT-R-R' and Pn-R-F8 with TES and TIPS side groups (R). End groups (R') for ADT-R-R' could be either F or CN.

4.3.2 Sample Preparation

For this study, four types of samples were prepared corresponding to each experimental set-up as shown in Fig. 4.3.

First, plain spheres were studied. Amorphous silica spheres 1 μm in diameter (Thermo Scientific, 0.99 $\pm$ 0.02 μm, refractive index n = 1.40 - 1.46, 2% suspension in water) were studied in one of three environments: ultra-pure millipore (Milli-Q, 18 $M\Omega$ cm) water, toluene, and a 50% wt/wt mixture of water and glycerol. Polystyrene (PS) spheres of 1 μm in diameter (Duke Scientific, Inc., refractive index n = 1.55) were studied in ultra-pure millipore water.

All coated silica spheres were studied in ultra-pure millipore water. Coatings were ADT-TES-F, Pn-TIPS-F8, PS, or an ADT-TES-F and ADT-TIPS-CN (D/A)

blend. For the ADT-TES-F and Pn-TIPS-F8 coatings, silica spheres were coated by mixing a 2 μL solution of silica spheres in water was added to 50 μL 30 mM stock solution of the coating molecule in toluene and sonicated for 20 minutes. Then, 14 μL of the mixture was added to 4 mL of ultra-pure millipore (Milli-Q, 18 $M\Omega$ cm) water, sonicated for 5 minutes, and left unperturbed overnight. For the PS coatings, 2 μL solution of silica spheres in water was added to 40 μL of 1% wt/wt solution of PS in toluene followed by the same protocol used for coating silica spheres with ADT-TES-F.

For the D/A blend, we prepared spheres coated with an ADT-TES-F (donor) and ADT-TIPS-CN (acceptor) D/A blend. A 30 mM stock solution of ADT-TES-F in toluene and 2 mM stock solution of ADT-TIPS-CN in toluene were sonicated for 10 minutes. 2 mL of the ADT-TES-F stock solution and 526 μL of the ADT-TIPS-CN stock solution were combined and sonicated for 10 minutes. Next, 4 μL solution of silica spheres in water was added to 100 μL the ADT-TES-F and ADT-TIPS-CN solution and sonicated for 20 minutes. Lastly, 14 μL of the silica and D/A solution was added to 4 mL of millipore water, sonicated for 5 minutes, and left unperturbed overnight. The ADT-TES-F and ADT-TES-F/ADT-TIPS-CN (Pn-TIPS-F8) coatings were confirmed using fluorescence microscopy at 532 nm (633 nm) cw excitation, which resulted in strong emission by the coatings at wavelengths of >580 nm (>650 nm)[16] as shown in Fig. 4.5. No fluorescence was observed from uncoated silica spheres.

Additionally, ADT-TES-F coated silica spheres were tested in toluene and a

50% wt/wt mixture of water and glycerol. When using toluene, the same procedure with water was followed, but toluene replaced water at the last step of the procedure. The ADT-TES-F coated silica spheres in a 50% wt/wt mixture of water and glycerol were made by adding 4 μL of the coated sphere solution in toluene to 4 mL of the 50% wt/wt mixture of water and glycerol.

Solutions of spheres described above were added to the sample holder shown in Fig. 4.6. Sample holders were constructed by grinding two holes into a glass slide to insert the solution of interest, and creating a fluid chamber with small pieces of a glass coverslip secured with UV glue (Thorlabs, NOA81). The top glass coverslip had two pieces of aluminum foil (secured with UV glue), which served as coplanar electrodes. The electrodes were separated by a gap of approximately 100 μm measured in each sample using optical microscopy by moving the sample on an x-y stage between the two electrodes and recording the position of the electrodes using a micrometer. Spheres were typically trapped about 20 μm away from the top coverslip to avoid any interactions between the glass slide and sphere. Spheres were trapped in the center of the gap between two electrodes to minimize edge effects.

4.3.3 Optical Tweezer Trapping Setup

Optical tweezer trapping was performed in a custom inverted microscope assembly with an oil immersion microscope objective (Edmund Optics, 100X, NA of 1.25,

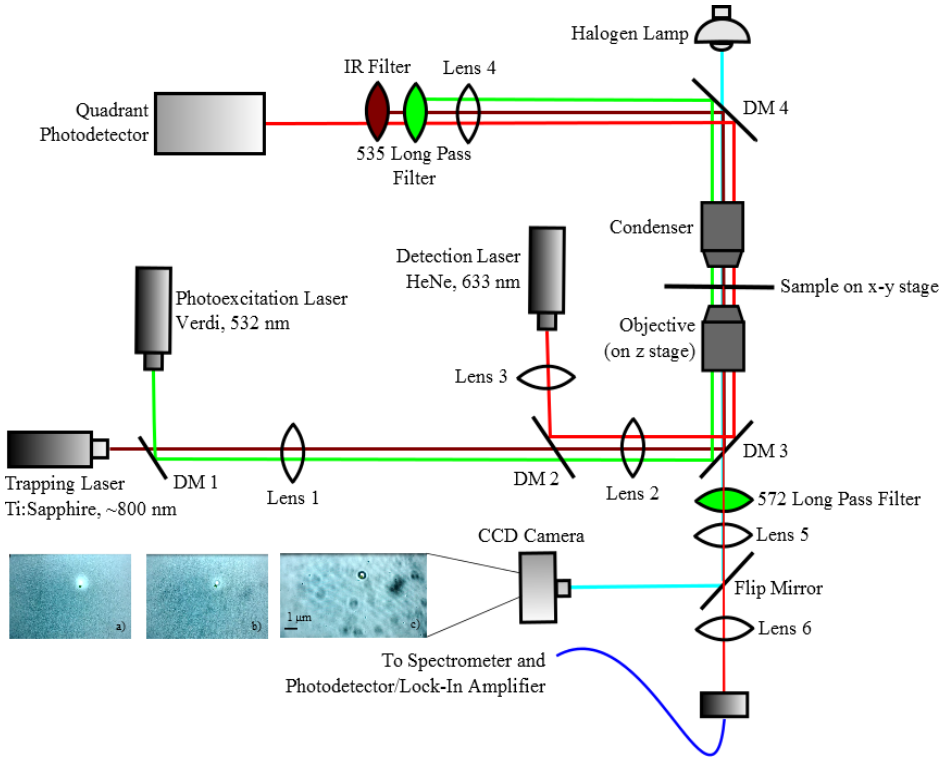

Figure 4.5: The experimental set up used to measure effective charge, which includes an 800 nm trapping laser, 633 nm (532 nm) detection laser, and 532 nm (633 nm) photoexcitation laser for the ADT-TES-F-coated (Pn-TIPS-F8-coated) spheres. The images are of a trapped ADT-TES-F coated silica sphere: (a) under 532 nm excitation (halogen lamp off), (b) under 532 nm excitation (halogen lamp on), and (c) no excitation (halogen lamp on). Fluorescence emission of the ADT-TES-F coating can be seen in (a) and (b).

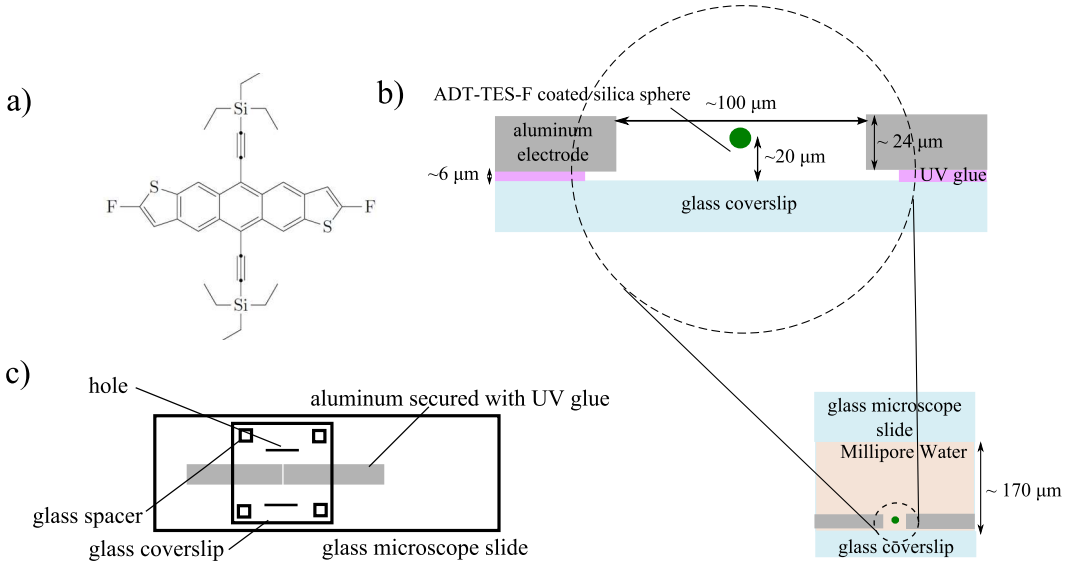

Figure 4.6: a) Molecular structure of ADT-TES-F. b) Side view of sample holder. Note the trapping distance away from the glass coverslip to minimize interaction between the coverslip and sphere. c) Top view of sample holder to show the holes ground into the microscope slide and positioning of the electrodes.

160 mm tube length) as shown in Fig. 4.5.[102] Spheres were trapped with a cw 800 nm Ti:Sapphire laser (KM Labs, Inc.). For uncoated silica spheres and coated silica spheres, the position of the trapped sphere was detected by the scattering of a cw 633 nm Helium-Neon laser (or cw 532 nm laser, Verdi V5, Coherent, Inc. for silica spheres coated with Pn-TIPS-F8) detected by a Hamamatsu S4349 quadrant photodiode (QPD). The QPD signal was collected using a data acquisition card (DAQ) (NI-6221) read out by a custom LabVIEW program. Additionally, a cw 532 nm (633 nm) laser beam, collimated to minimize its effect on the trap stability, was used to photoexcite all coatings (or Pn-TIPS-F8). Spheres were imaged with a CCD camera and halogen lamp. When assessing fluorescence from an ADT-TES-F coating, a long-pass 572 nm filter was placed in front of the CCD camera to transmit the fluorescence emission of the ADT-TES-F molecules, while blocking the 532 nm excitation. Filters were also placed in front of the QPD to block the 800 nm and 532 nm light. For spheres with a Pn-TIPS-F8 coating, a 632.8 nm notch filter was placed in front of the CCD camera to block light from the 633 nm excitation laser. A band pass filter was placed in front of the QPD to block emission from the spheres, but allow the scattering of the 532 nm light to pass. An IR filter was also placed in front of the QPD to block the trapping laser.

To measure effective charge on our spheres, we applied an AC voltage in the range of 2.5 V_{pp} to 20 V_{pp} across the electrodes of the sample holder using an amplified sinusoidal signal from function generator (Tektronix, AFG3021). Frequencies f_{AC} ranging from 30 Hz to 500 Hz were tested, and charge measurements at frequencies in the range between 70 and 110 Hz yielded most consistent data, prompt-

ing us to select a driving frequency of 110 Hz for most experiments reported here. The electric field was estimated as $\lambda\frac{V}{d}$ where V is the applied voltage and d is the distance between electrodes. The scaling factor λ, described in Ref. 30, takes into account the electric field dependence on the position of the sphere with respect to the electrodes. Another interpretation comes from treating the electrode-solution interface as a double-layer capacitance as described in Ref. 32. There is also an internal resistance at this double-layer, and a second capacitor is included in analysis for the Stern layer effect. The electric field then depends on the driving frequency of the sinusoidal electric field. The electric field can be represented as

$$E(\omega) = \frac{V_{pp}}{2d}\frac{R_b}{Z(\omega)} \tag{4.20}$$

where R_b is the resistance of the water far from the double-layer region of the trapped sphere and $Z(\omega)$ is the total impedance in the angular frequency domain.[32] The change in surface charge density can be seen as a function of frequency in Fig. 4.7. Since the apparent electric field strength changes as a function of frequency as seen in Eq. 4.20, the driving frequency used of $\sim 110\ Hz$ represents a lower bound of surface charge.

In order to probe changes in effective charge density upon photoexcitation of ADT-TES-F in ADT-TES-F-coated spheres, we performed charge measurements under 532 nm excitation at powers of up to 28 mW.

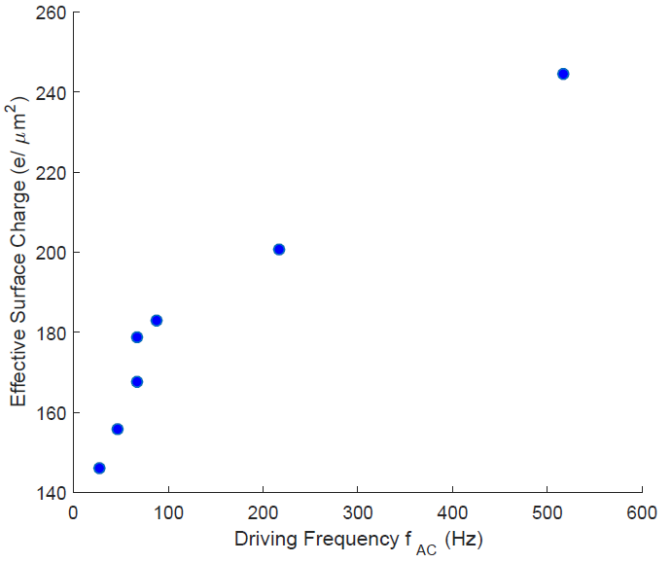

Figure 4.7: Dependence of the effective surface charge density of a plain silica microsphere in water on driving frequency of electric field. As shown in Eq. 4.20, there is some dependence on the screening of electric charges with different driving frequencies.

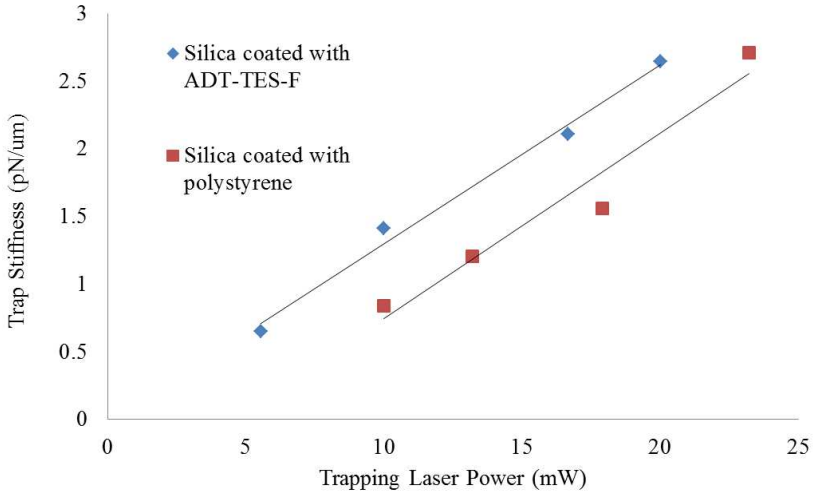

Figure 4.8: Dependence of measured trap stiffness on the trapping beam power in coated spheres. Linear dependence is expected in the case of stable trapping.

4.4 Results: Trap Stiffness

The trap stiffness was measured at various trapping beam powers, and the linear dependence of k on the power was observed (Fig. 4.8). As expected, at same trapping beam power, the trap stiffness for PS spheres, as well as for PS- and ADT-TES-F-coated spheres, was higher than that for silica spheres since PS and ADT-TES-F have a higher index of refraction as compared to silica.[102]

4.5 Results: Surface Charge

Charge measurements were performed by tracking the position of a trapped sphere with an applied AC electric field. Fig. 4.9 shows two of the methods for calculating trap stiffness, which also demonstrates the presence of charge on the sphere.[106] The histograms (Fig. 4.9a) are used to calculate trap stiffness without an electric field. In the presence of an electric field, the histogram broadens, with the broadening increasing as the electric field increases. The alternating electric field makes it possible for the sphere to spend more time away from the center of the trap since there is now an electric force in addition to Brownian motion. The power spectral density (PSD) (Fig. 4.9b) also demonstrates the presence of charge on the sphere, as there is a response at the 110 Hz driving frequency of the AC electric field, which increases as the electric field increases. Silica spheres in water exhibited a much larger response to the AC electric field, as compared to those in toluene: in water, the AC field-driven sphere oscillations overriding the Brownian motion could be obtained within our range of applied electric fields.[107] These oscillations were not apparent in toluene, consistent with a considerably smaller charge density on silica spheres in toluene as compared to water (see Table 4.1). A bimodal distribution of position is not expected to be seen either based on their γ values (< 1.257) of Eq. 4.9.[30] Applying higher electric fields also agrees with Eqs. 4.10 & 4.11 where the relationship between P_{AC} and E^2 is linear as shown in Fig. 4.10.[106] A larger slope corresponds to a larger charge on the sphere as expected.

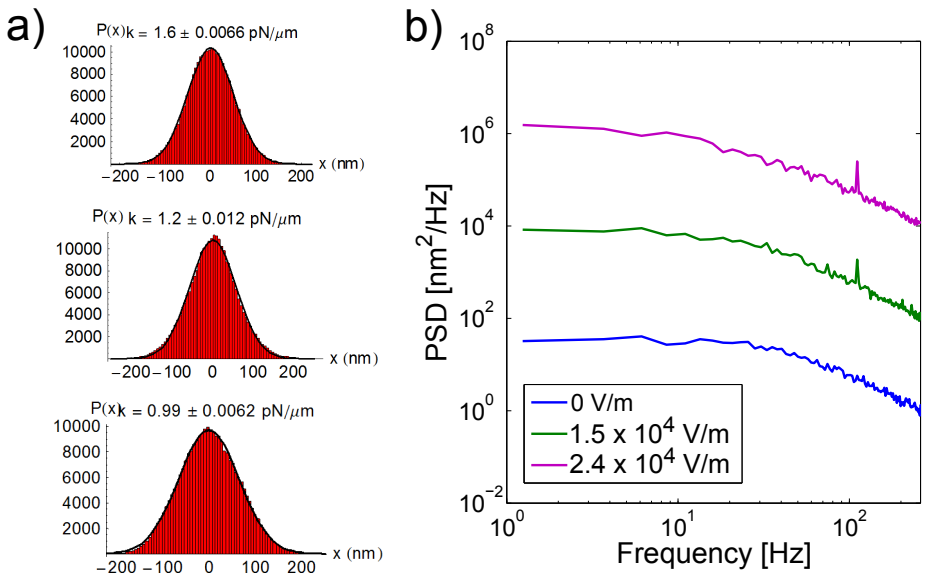

Figure 4.9: a) Top: No electric field; Middle: $E = 1.5 \times 10^4$ V/m; Bottom: $E = 2.4 \times 10^4$ V/m. b) Power spectral densities for silica in toluene with varying applied electric fields. Note the peak at the driving frequency of 110 Hz get larger as electric field increases. Data for non-zero electric fields are shifted up on the vertical axis for clarity.

	Surface Charge (e/μm^2)	
Sphere Type	**Water**	**Toluene**
Silica	290 ± 95	4 ± 1
PS	25 ± 12	
Silica coated with ADT-TES-F	13 ± 5	7 ± 1
Silica coated with Pn-TIPS-F8	22 ± 13	

Table 4.1: Effective surface charge measured for various spheres in water and toluene. The values were averaged over 5-7 spheres of the same type and over at least 9 data runs for each sphere. The error bars reflect sphere-to-sphere variation. The run-to-run error for each given sphere was less than 5%.

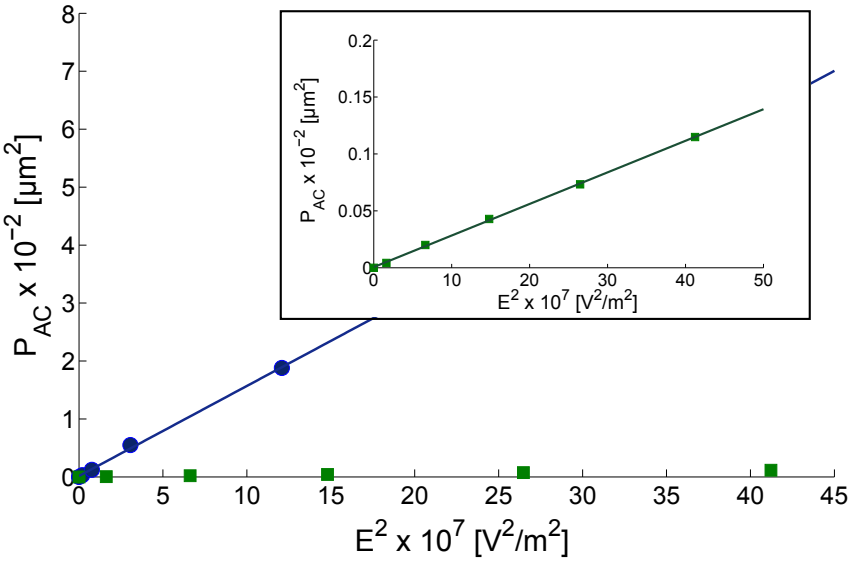

Figure 4.10: **Blue circle** : Silica; **Green square** : Silica coated with ADT-TES-F. All spheres in water. Slopes correspond to the amount of charge on sphere and are linear as predicted.

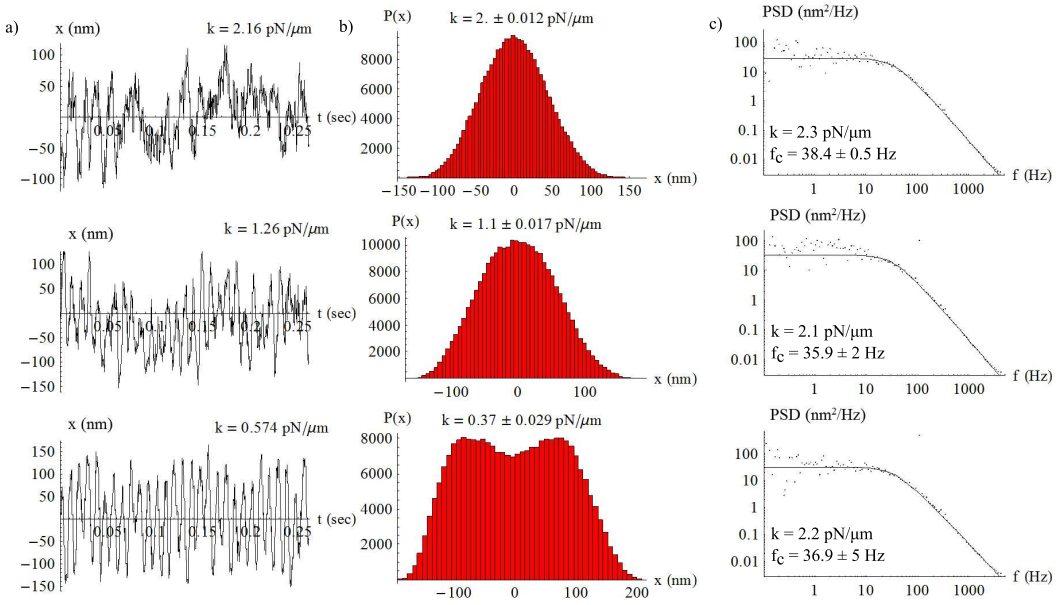

Figure 4.11: Example of data obtained from a trapped PS sphere: (top) no applied electric field, (middle) and (bottom) applied electric fields of 1.71×10^4 V/m and 3.43×10^4 V/m, respectively, with a driving frequency of 110 Hz. Note the peaks at 110 Hz in the power spectrum due electric field induced motion of the charged sphere. a) Time series data of suppressed Brownian motion. Note a transition to sinusoidal dependence at higher electric fields. b) Histogram of the sphere's motion in the trap. c) Power spectrum of the sphere's motion.

4.5.1 Uncoated Spheres and PS Coated Spheres in Water

As a control, uncoated PS and silica spheres were suspended in water.

Effective surface charge measurements of plain silica spheres is shown in Table 4.1. It is well known that silica in contact with water is negatively charged due to dissociation of silanol groups.[108] The magnitude of the effective charge density increases with ionic strength.[108] In ultra-pure deionized water with an ionic

strength of below 10^{-6}M, it is expected to be below 2000 $e/\mu m^2$, where e is the elementary charge. For example, a surface charge density of -700 $\pm$ 150 $e/\mu m^2$ was obtained in Ref. 108. Our experiments yielded the magnitude of the surface charge density for silica spheres of about 290 $e/\mu m^2$ (Table 4.1). This value represents a lower bound on the magnitude of the surface charge density, as the electric field in the proximity to the sphere immersed in a medium with high dielectric constant such as water ($\epsilon = 81$) is partially screened; accounting for such reduction in the electric field in the Eq. 4.11 would increase the effective charge Z_{eff}.

Effective surface charge measurements of plain PS spheres is shown in Table 4.1. Negative charge on the surface of PS spheres in water has previously been attributed to the adsorption of hydroxyl ions (ion transfer), to the electron transfer from water to PS resulting from the overlap of local intrinsic molecular-ion states in PS and water, or both.[109,110] The obtained surface charge densities ranged from 455 $e/\mu m^2$ to 553 $e/\mu m^2$ for PS spheres functionalized with sulfate groups and carboxylated, respectively[111] and 9375 $e/\mu m^2$ for larger PS spheres (d=2.23 μm) in an aqueous solution of 1-butyl-3-methylimidazolium chloride (BMIM-CI) at a pH of 6.[112] Surface charge densities for PS spheres obtained in our experiments in ultra-pure water yielded considerably lower values (Table 4.1), as expected.

The silica spheres coated with PS exhibited surface charge densities lower than those in uncoated silica spheres and higher than those in PS spheres (Table 4.1). Adsorption of PS by silica has been previously observed and attributed to a hydrogen bond formation between the hydroxyl group on silica and phenyl ring on

PS.[113] Therefore, a reduction of effective charge in PS-coated silica spheres by a factor of ∼3, as compared to uncoated silica spheres, is due to a partial or complete isolation of the silanol groups on the silica surface from water, which prevents their dissociation.

4.5.2 Organic Semiconductor Coated Spheres

As shown in Table 4.1, the silica spheres coated with ADT-TES-F or Pn-TIPS-F8 exhibited effective charge densities that are a factor of ∼13 - 22 lower than those in uncoated silica and a factor of ∼7 lower than those in silica coated with PS. ADT-TES-F is a nonpolar molecule which is not expected to significantly interact with water, and the observed effective charge reduction reflects efficient adsorption of ADT-TES-F (Pn-TIPS-F8) onto silica surface, which prevents silica-water interaction. A considerably smaller effective charge densities in ADT-TES-F-coated as compared to PS-coated spheres are most likely due to efficient ADT-TES-F aggregation that promotes thicker surface layers. A further reduction by more than an order of magnitude in effective charge density was observed in the ADT-TES-F-coated silica spheres when water was replaced with a 50 % wt/wt mixture of water and glycerol, due to reduction in polarity ($\epsilon = 64$). This is consistent with Ref. 111 who found more than an order of magnitude reduction in the effective charge of PS spheres in 35% wt/wt glycerol/water solution as compared to water.

4.5.3 Uncoated and Coated spheres in Toluene

Spheres suspended in (nonpolar) toluene, both uncoated and coated, exhibited a considerably lower surface charge as compared to those in water, which suggests weak or no interaction of either silica or organic semiconductor molecules with toluene. This is consistent with observations of low surface charge on PMMA spheres suspended in (nonpolar) dodecane in similar experiments.[30,31] No degradation of the coatings or changes in the total surface charge density were observed for spheres suspended in toluene over the period of at least 6 hours of experimental observation.

4.5.3.1 Monitoring PL

Measuring the type of interaction between donor/acceptor blends is just as important as measuring the effective surface charge over time. In order to confirm coating of the silica spheres, we obtained fluorescence spectra of the coating of trapped spheres in water under a 532 nm or 633 nm excitation, depending on the coating. Fig. 4.12 demonstrates the fluorescence of a silica sphere coated with ADT-TES-F and of a sphere coated with the ADT-TES-F/ADT-TIPS-CN (D/A) blend.[106] The ADT-TES-F-coated spheres exhibited fluorescence emission with a maximum at 590 nm, consistent with that from pristine ADT-TES-F films previously studied in thin-film devices.[81,86] The fluorescence emission from the ADT-TES-F/ADT-TIPS-CN D/A blend coating was dominated by that from the

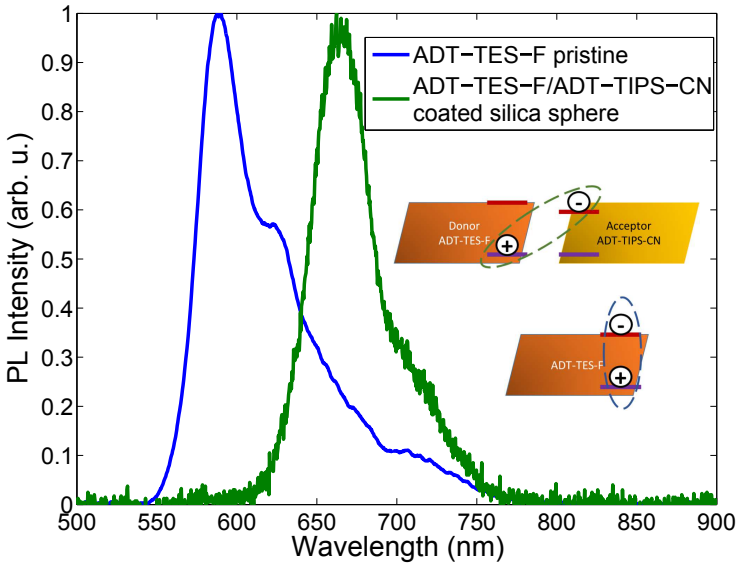

Figure 4.12: Fluorescence from an ADT-TES-F-coated silica sphere and an ADT-TES-F/ADT-TIPS-CN (D/A blend) - coated silica sphere. Fluorescence emission from the D/A coated sphere is due to the exciplex formed between the donor and acceptor molecules. Inset shows schematics of the emissive ADT-TES-F exciton and of the ADT-TES-F/ADT-TIPS-CN exciplex.

ADT-TES-F/ADT-TIPS-CN exciplex at $\sim$ 668 nm, also consistent with that from the ADT-TES-F/ADT-TIPS-CN films.[7] While in our present studies the fluorescence emission is used to confirm quality of our coatings, quantitative analysis of fluorescence as a function of applied electric field can be used to monitor exciton (in pristine materials) or exciplex (in D/A blends) dissociation into charge carriers. This can be then combined with monitoring of the total effective charge on the organic semiconductor coating (described below), to quantify photoexcited charge exchange between the organic semiconductor and the surrounding environment.

4.5.3.2 Surface Charge over Time

In order to investigate time evolution of effective charge density, we increased the AC electric field driving frequency to 1 kHz, which is substantially higher than the typical corner frequencies characterizing our optical traps (Figs. 4.9 and 4.11), and analyzed data obtained from ADT-TES-F-coated silica spheres in a 50% wt/wt water/glycerol mixture using Eq. 4.19 and a method proposed in Ref. 31. Rapid fluctuations of the effective charge were observed, which are expected in a polar medium; however, considerably higher electric fields are necessary to quantify time dependence of the charge density. Similarly, considerably higher applied electric fields are needed to observe a time evolution of effective charge as a result of photoconductivity induced in the ADT-TES-F film by the 532 nm excitation under applied electric field, as no effect of ADT-TES-F photoexcitation with cw 532 nm beam on the effective charge density was observed under our experimental conditions.

In order to conduct (dis)charging experiments with our samples, it must be possible to apply much higher electric fields.[31] Higher electric fields on the order of 1×10^6 V/m were applied to both silica spheres in toluene and water. The spheres suspended in toluene remained usable whereas the spheres suspended in water were not as the water started to boil. Surface charge density was also measured while coated spheres were photoexcited while simultaneously being trapped. Their surface charge density was comparable to spheres without photoexcitation.

4.6 Conclusion

We demonstrated feasibility of using an optical tweezer-based technique for measurements of effective charge density in organic semiconductor films at microscopic scales in several environments concurrently with measurements of fluorescence emission from the coatings. Effective charge densities of 13±5 elementary charges per μm^2 were observed in ADT-TES-F-coated silica microspheres suspended in water indicating the coating did not react with the water. These are about a factor of ∼7 lower than effective charge densities obtained in similar silica microspheres coated with PS, indicative of efficient adsorption of ADT-TES-F onto silica surface followed by ADT-TES-F aggregation to promote a thicker coating, as compared to PS.

Effective charge densities lower than one elementary charge per μm^2 were observed in the ADT-TES-F-coated spheres upon replacing water with the 50% wt/wt glycerol/water mixture. The spheres suspended in toluene also had a low surface charge density, indicating neither the silica or coatings reacted with toluene.

We also demonstrated fluorescence of a coated sphere of either donor or D/A blends can be monitored with a spectrometer in the optical tweezers set up.

With the ability to measure the effective surface charge of organic semiconductor-coated microscpheres concurrently with fluorescence, and in both highly polar and nonpolar environments, future systematic studies of photoinduced charge photogeneration and transfer can be performed at nanoscales. With high electric fields,

there is potential for single charge resolution.[31] and to measure surface charge as a function of dielectric permittivity of the surrounding environment.

Chapter 5 Conclusion

While organic semiconductors offer a low cost, tunable, and solution processable alternative to inorganic semiconductors, there is still much to be learned about molecular properties and their interactions to improve upon the efficiencies of these devices. Over the last six years, I have focused on improving our understanding of how the properties and packing of molecules change within blends as a function of its environment and the molecular structure of the molecule itself.

My main projects have utilized two techniques: single molecule fluorescence spectroscopy (SMFS) and optical tweezers. SMFS looks beyond the ensemble average and allows one to study individual molecules. SMFS probes a population of well-spaced molecules with a high signal to noise ratio and allows the study of nanoscale molecular behavior and its local nanoenvironment. Studying individual molecules allows the study of intermediate molecular stages that are normally lost in the ensemble average. Optical tweezers use a highly-focused laser beam to optically trap micron-sized particles. In the last decade, it was shown surface charge of trapped particles can be measured using optical tweezers.

I concentrated on studies involving the effects on the local nanoenvironment and packing on the photophysics of these organic semiconductors. Using SMFS, I have studied 1) how the photophysics of these molecules changes by modifying

and controlling the nanoenvironment by adding acceptor molecules and changing their concentration, and 2) the orientation and photophysics of these molecules in a variety of host matrices and with different side groups. Using optical tweezers, I have 3) developed a novel technique which allows the study charge transfer with the potential for single charge resolution.

My first project presented investigated how the photophysics of donor molecules (D) changes as the local environment changes by adding acceptor molecules (A) at different concentrations. As acceptor concentration increases, donor molecule visibility decreases and at very high concentrations of acceptor, is not observed at all. This observation was due to efficient energy transfer (FRET) between the donor and acceptor molecules such that the donor molecules were all dark. By increasing donor molecule concentration with this high (non-fluorescent) acceptor background, weve created a new super-resolution tool to image donor molecules in a modified local environment that has not been achieved before.

By fitting the distribution of "on" (bright) and "off" (dark) times, we can model how the photoexcited molecule interactions with the local nanoenvironment. We found as the concentration of acceptors increases, the "on" times get shorter, but the "off" times stay the same. This insight reveals that the local nanoenvironment is changing with the added acceptor. To understand this behavior, we studied the relationship between "on" times and the previous "off" time and found there is only a trend for samples with no added acceptor where the "on" time decreases as the duration of the "off" time increases. The addition of added acceptors plays

a critical role during the "off time of the donor molecule by reducing the negative impact of the "off" event on the following "on" period.

The interpretation for the observed behavior is the following: the donor molecule is "on" until it reacts with oxygen and forms a different species (thus turning "off"). This process is reversible; however, during the reverse reaction, highly reactive oxygen is released and the molecule reacts again. In this process, there is only 10% probability not to immediately react again and turn back "on". As acceptors are added, the changes in the local morphology result in less protection of the donor molecule with respect to interaction with oxygen, so that the molecule turns "off" faster. However, once the reverse reaction happens, the singlet oxygen diffuses and reacts with the acceptor molecules instead of the donor, increasing the probability of turning back "on" to $> 50\%$.

The second project presented investigated the packing of organic semiconductor molecules as it is directly related to their charge carrier dynamics and photostability. This project with SMFS focused on how molecular packing changes as a function of different host matrices and as a function of different side groups. In addition to performing these experiments, I wrote code to efficiently analyze the large data sets generated from both my colleagues and my own experiments. We found that molecules embedded in a crystalline organic semiconductor host matrix (t-bu BTBTB) exhibited higher photostability than a polymer matrix (PMMA). In addition, larger side groups also lead to higher photostability, indicating the larger side groups provide better protection from reactions with oxygen. Using a

crystalline host restricts guest molecule orientation and molecules with larger side groups are oriented more broadly than those with smaller side groups.

Lastly, I developed a novel method to study charge transfer between organic semiconductor materials using optical tweezers. A silica microsphere is coated with an organic semiconductor film and suspended in a solution (e.g., water, toluene, glycerol/water mix). The surface charge of this sphere can be measured by trapping the sphere using optical tweezers and applying a sinusoidal electric field across the sphere. The surface charge is calculable by measuring the position of the sphere in response to the applied field. (Dis)charging dynamics is measurable by photoexciting the coating of the sphere and observing the formation of excitons (electron-hole pairs) by collecting the photoluminescence of the trapped sphere. If a sphere is close to a piece of material (either donor or acceptor), charge transfer between the coating and material in solution is observed.

These projects are important to the scientific community. I have characterized different molecules in a variety of host matrices via SMFS, developed a super-resolution technique with SMFS, investigated how acceptors change the local nanoenvironment and affect the interaction of oxygen and donor molecules, and created a non-contact technique of measuring (dis)charging dynamics with optical tweezers.

Bibliography

[1] W. E. Moerner and David P. Fromm. Methods of single-molecule fluorescence spectroscopy and microscopy. *Review of Scientific Instruments*, 74(8):3597–3619, 2003.

[2] Whitney E. B. Shepherd. *Optoelectronic Properties of Organic Semiconductors: From Bulk to Single Molecule*. PhD thesis, Oregon State University, 2012.

[3] W. E. B. Shepherd, R. Grollman, A. Robertson, K. Paudel, R. Hallani, M. A. Loth, J. E. Anthony, and O. Ostroverkhova. Single-molecule imaging of of organic semiconductors: Toward nanoscale insights into photophysics and molecular packing. *Chemical Physics Letters*, 629:29–35, 2015.

[4] R. Grollman, W.E.B. Shepherd, A. Robertson, K. Paudel, J. E. Anthony, and O. Ostroverkhova. Photophysics of organic semiconductors: from ensemble to the single-molecule level. *Proc. of SPIE*, 9360, 2015.

[5] J. W. Shaevitz. A practical guide to optical trapping. www.genomics.princeton.edu/shaevitzlab/OT_Practicle_Guide.pdf, 2006.

[6] M. J. Kendrick, A. Neunzert, M. M. Payne, B. Purushothaman, B. D. Rose, J. E. Anthony, M. M. Haley, and O. Ostroverkhova. Formation of the donoracceptor charge-transfer exciton and its contribution to charge photogeneration and recombination in small-molecule bulk heterojunctions. *Journal of Physical Chemistry C*, 116:1810818116, 2012.

[7] W. E. B. Shepherd, A. D. Platt, M. J. Kendrick, M. Loth, J. E. Anthony, and O. Ostroverkhova. Energy transfer and exciplex formation and their impact on exciton and charge carrier dynamics in organic films. *Journal of Physical Chemistry Letters*, 2:362–366, 2011.

[8] K. Paudel, B. Johnson, A. Neunzert, M. Thieme, B. Purushothaman, M. M. Payne, J. E. Anthony, and O. Ostroverkhova. Small-molecule bulk heterojunctions: Distinguishing between effects of energy offsets and molecu-

lar packing on optoelectronic properties. *Journal of Physical Chemistry C*, 117:24752–24760, 2013.

[9] W. Brütting. Introduction to the physics of organic semiconductors. In W. Brütting, editor, *Physics of Organic Semiconductors*, chapter 1. Wiley-VCH, 2005.

[10] M. Pope, H. P. Kallmann, and P. Magnante. Electroluminescence in organic crystals. *Journal of Chemical Physics*, 38:2042–2043, 1963.

[11] C. K. Chiang, C. R. Fincher, Y. W. Park, A. J. Heeger, H. Shirakawa, E. J. Louis, S. C. Gau, and Alan G. Macdiarmid. Electrical conductivity in doped polyacetylene. *Physical Review Letters*, 39:1098–1101, 1977.

[12] Oksana Ostroverkhova. Organic optoelectronic materials: Mechanisms and applications. *Chemical Reviews*, 116:13279–13412, 2016.

[13] M. E. Gershenson, V. Podzorov, and A. F. Morpurgo. Colloquium: Electronic transport in single-crystal organic transistors. *Rev. Mod. Phys.*, 78:973–989, Sep 2006.

[14] Oksana Ostroverkhova. Photophysical and photoconductive properties of novel organic semiconductors. In F. Cicoira and C. Santato, editors, *Organic Electronics*, chapter 10. Wiley-VCH, 2013.

[15] Joseph R. Lakowicz. *Principles of Fluorescence Spectroscopy*. Springer, 3rd edition, 2006.

[16] Andrew D. Platt, Jonathan Day, Sankar Subramanian, John E. Anthony, and Oksana Ostroverkhova. Optical, fluorescent, and (photo)conductive properties of high-performance functionalized pentacene and anthradithiophene derivatives. *Journal of Physical Chemistry C*, 113:14006–14014, 2009.

[17] D. T. Chase, B. D. Rose, S.P. McClintock, L. N. Zakharov, and M. M. Haley. Indeno[1,2-b]fluorenes: fully conjugated antiaromatic analogues of acenes. *Angew Chem Int Ed*, 50:1127–1130, 2011.

[18] Boleslaw Kozankiewicz and Michel Orrit. Single-molecule photophysics, from cryogenic to ambient conditions. *Chemical Society Review*, 43:1029–1043, 2014.

[19] Chelsea M. Hess, Erin A. Riley, and Philip J. Reid. Dielectric dependence of single-molecule photoluminescence intermittency: Nile red in poly(vinylidene fluoride). *The Journal of Physical Chemistry B*, 118(29):8905–8913, 2014.

[20] Kristin L. Wustholz, Eric D. Bott, Bart Kahr, and Philip J. Reid. Memory and spectral diffusion in single-molecule emission. *The Journal of Physical Chemistry C*, 112(21):7877–7885, 2008.

[21] Samuel J. Lord, Nicholas R. Conley, Hsiao-lu D. Lee, Stefanie Y. Nishimura, Andrea K. Pomerantz, Katherine A. Willets, Zhikuan Lu, Hui Wang, Na Liu, Reichel Samuel, Ryan Weber, Alexander Semyonov, Meng He, Robert J. Twieg, and W. E. Moerner. Dcdhf fluorophores for single-molecule imaging in cells. *ChemPhysChem*, 10(1):55–65, 2009.

[22] Michel Orrit. Single-molecule spectroscopy: The road ahead. *Journal of Chemical Physics*, 117(24):10938–10946, 2002.

[23] W. E. Moerner and L. Kador. Optical detection and spectroscopy of single molecules in a solid. *Physical Review Letters*, 62(21):2535–2538, 1989.

[24] M. Orrit and J. Bernard. Single pentacene molecules detected by fluorescence excitation in a p-terphenyl crystal. *Physical Review Letters*, 65(21):2716–2719, 1990.

[25] Eric Betzig and Robert J. Chichester. Single molecules observed by near-field scanning optical microscopy. *Science*, 262(5138):1422–1425, 1993.

[26] The nobel prize in chemistry 2014 - press release, 2014.

[27] S. M. Block. Making light work with optical tweezers. *Nature*, 360:493–495, 1992.

[28] Jack Ng, Zhifang Lin, and C. T. Chan. Theory of optical trapping by an optical vortex beam. *Phys. Rev. Lett.*, 104:103601, Mar 2010.

[29] A. Ashkin. History of optical trapping and manipulation of small-neutral particle, atoms, and molecules. *IEEE J. Sel. Top. Quantum Electron*, 6:841–856, 2000.

[30] G. Seth Roberts, Tiffany A. Wood, William J. Frith, and Paul Bartlett. Direct measurement of the effective charge in nonpolar suspensions by optical tracking of single particles. *The Journal of Chemical Physics*, 126(19), 2007.

[31] Filip Beunis, Filip Strubbe, Kristiaan Neyts, and Dmitri Petrov. Beyond millikan: The dynamics of charging events on individual colloidal particles. *Phys. Rev. Lett.*, 108:016101, Jan 2012.

[32] Giuseppe Pesce, Vincenzo Lisbino, Giulia Rusciano, and Antonio Sasso. Optical manipulation of charged microparticles in polar fluids. *Electrophoresis*, 34:3141–3149, 2013.

[33] Giuseppe Pesce, Giulia Rusciano, Gianluigi Zito, and Antonio Sasso. Simultaneous measurements of electrophoretic and dielectrophoretic forces using optical tweezers. *Optics Express*, 23(7), 2015.

[34] T. Basche. *Single-molecule optical detection, imaging and spectroscopy.* Weinheim; Cambridge : VCH, 1997.

[35] Werner Fudickar and Torsten Linker. Why triple bonds protect acenes from oxidation and decomposition. *Journal of the American Chemical Society*, 134(36):15071–15082, 2012.

[36] E Brooks Shera, Newton K Seitzinger, Lloyd M Davis, Richard A Keller, and Steven A Soper. Detection of single fluorescent molecules. *Chemical Physics Letters*, 174(6):553–557, 1990.

[37] Conerd K Frederickson, Bradley D Rose, and Michael M Haley. Explorations of the indenofluorenes and expanded quinoidal analogues. *Accounts of Chemical Research*, 2017.

[38] Keshab Paudel, Brian Johnson, Mattson Thieme, Michael M. Haley, Marcia M. Payne, John E. Anthony, and Oksana Ostroverkhova. Enhanced charge photogeneration promoted by crystallinity in small-molecule donor-acceptor bulk heterojunctions. *Applied Physics Letters*, 105(4), 2014.

[39] Bradley D Rose, Natalie J Sumner, Alexander S Filatov, Steven J Peters, Lev N Zakharov, Marina A Petrukhina, and Michael M Haley. Experimental and computational studies of the neutral and reduced states of indeno [1, 2-b] fluorene. *Journal of the American Chemical Society*, 136(25):9181–9189, 2014.

[40] Daniel T Chase, Aaron G Fix, Seok Ju Kang, Bradley D Rose, Christopher D Weber, Yu Zhong, Lev N Zakharov, Mark C Lonergan, Colin Nuckolls, and

Michael M Haley. 6, 12-diarylindeno [1, 2-b] fluorenes: syntheses, photophysics, and ambipolar ofets. *Journal of the American Chemical Society*, 134(25):10349–10352, 2012.

[41] Yang Cao, Yong Liang, Lei Zhang, Sílvia Osuna, Andra-Lisa M Hoyt, Alejandro L Briseno, and KN Houk. Why bistetracenes are much less reactive than pentacenes in diels–alder reactions with fullerenes. *Journal of the American Chemical Society*, 136(30):10743–10751, 2014.

[42] Samuel J. Lord, Zhikuan Lu, Hui Wang, Katherine A. Willets, P. James Schuck, Hsiao-lu D. Lee, Stefanie Y. Nishimura, Robert J. Twieg, and W. E. Moerner. Photophysical properties of acene dcdhf fluorophores: long-wavelength single-molecule emitters designed for cellular imaging. *The Journal of Physical Chemistry A*, 111(37):8934–8941, 2007. PMID: 17718454.

[43] Taekjip Ha, Ted A. Laurence, Daniel S. Chemla, and Shimon Weiss. Polarization spectroscopy of single fluorescent molecules. *The Journal of Physical Chemistry B*, 103(33):6839–6850, 1999.

[44] E. A. Riley, C. M. Hess, P. J. Whitham, and P. J. Reid. Beyond power laws: A new approach for analyzing single molecule photoluminescence intermittency. *Journal of Chemical Physics*, 136:184508, 2012.

[45] M. Kuno, D. P. Fromm, H. F. Hamann, A. Gallagher, and D. J. Nesbitt. "on"/"off" fluorescence intermittency of single semiconductor quantum dots. *Journal of Chemical Physics*, 115(2):1028 – 1040, 2001.

[46] Waloddi Weibull et al. A statistical distribution function of wide applicability. *Journal of applied mechanics*, 18(3):293–297, 1951.

[47] Alan K Burnham and Robert L Braun. Global kinetic analysis of complex materials. *Energy & Fuels*, 13(1):1–22, 1999.

[48] Zorica Z Baros and Borivoj K Adnaevic. Weibull cumulative distribution function for modeling the isothermal kinetics of the titanium-oxo-alkoxy cluster growth. *Industrial & Engineering Chemistry Research*, 52(5):1836–1844, 2013.

[49] Rebecca Grollman, Nicole Quist, Alexander Robertson, Jeremy Rath, Balaji Purushothaman, Michael M Haley, John E Anthony, and Oksana Ostroverkhova. Single-molecule level insight into nanoscale environment-

dependent photophysics in blends. *The Journal of Physical Chemistry C*, 121:12483–12494, 2017.

[50] N. Quist, R. Grollman, J. Rath, A. Robertson, M. Haley, J. Anthony, and O. Ostroverkhova. Single molecule-level study of donor-acceptor interactions and nanoscale environment in blends. *Proc. of SPIE*, 10101:101010K, 2017.

[51] Masaaki Mitsui, Aki Unno, and Syun Azechi. Understanding photoinduced charge transfer dynamics of single perylenediimide dyes in a polymer matrix by bin-time dependence of their fluorescence blinking statistics. *The Journal of Physical Chemistry C*, 120(28):15070–15081, 2016.

[52] Erin A Riley, Chelsea M Hess, Jan Rey L Pioquinto, Werner Kaminsky, Bart Kahr, and Philip J Reid. Proton transfer and photoluminescence intermittency of single emitters in dyed crystals. *The Journal of Physical Chemistry B*, 117(16):4313–4324, 2013.

[53] Donald B Siano. The log-normal distribution function. *J. Chem. Educ*, 49(11):755, 1972.

[54] Natalie Z Wong, Alana F Ogata, and Kristin L Wustholz. Dispersive electron-transfer kinetics from single molecules on tio2 nanoparticle films. *The Journal of Physical Chemistry C*, 117(41):21075–21085, 2013.

[55] V. Formenko and D. J. Nesbitt. Solution control of radiative and nonradiative lifetimes: A novel contribution to quantum dot blinking and suppression. *Nano Letters*, 8.

[56] Jacob P. Hoogenboom, Wouter K. den Otter, and Herman L. Offerhaus. Accurate and unbiased estimation of power-law exponents from single-emitter blinking data. *Journal of Chemical Physics*, 125:204713, 2006.

[57] A. Brunger, P. Strop, M. Vrljic, S. Chu, and K. R. Weninger. Three-dimensional molecular modeling with single molecule fret. *Journal of Structural Biology*, 173:497–505, 2011.

[58] Thomas Christ, Florian Kulzer, Patrice Bordat, and Thomas Basché. Watching the photo-oxidation of a single aromatic hydrocarbon molecule. *Angewandte Chemie International Edition*, 40(22):4192–4195, 2001.

[59] Rob Zondervan, Florian Kulzer, Mikhail A Kol'chenk, and Michel Orrit. Photobleaching of rhodamine 6g in poly (vinyl alcohol) at the ensemble and single-molecule levels. *The Journal of Physical Chemistry A*, 108(10):1657–1665, 2004.

[60] Mathias Haase, Christian G Hübner, Fabian Nolde, Klaus Müllen, and Thomas Basché. Photoblinking and photobleaching of rylene diimide dyes. *Physical chemistry chemical physics*, 13(5):1776–1785, 2011.

[61] Balaji Purushothaman, Sean R Parkin, Mark J Kendrick, Daniel David, Jeremy W Ward, Liyang Yu, Natalie Stingelin, Oana D Jurchescu, Oksana Ostroverkhova, and John E Anthony. Synthesis and charge transport studies of stable, soluble hexacenes. *Chemical Communications*, 48(66):8261–8263, 2012.

[62] Simil Thomas, Jack Ly, Lei Zhang, Alejandro L. Briseno, and Jean-Luc Bredas. Improving the stability of organic semiconductors: Distortion energy versus aromaticity in substituted bistetracene. *Chemistry of Materials*, 28(23):8504–8512, 2016.

[63] Paolo Coppo and Stephen G Yeates. Shining light on a pentacene derivative: The role of photoinduced cycloadditions. *Advanced Materials*, 17(24):3001–3005, 2005.

[64] Ashok Maliakal, Krishnan Raghavachari, Howard Katz, Edwin Chandross, and Theo Siegrist. Photochemical stability of pentacene and a substituted pentacene in solution and in thin films. *Chemistry of materials*, 16(24):4980–4986, 2004.

[65] Brian H Northrop, KN Houk, and Ashok Maliakal. Photostability of pentacene and 6, 13-disubstituted pentacene derivatives: a theoretical and experimental mechanistic study. *Photochemical & Photobiological Sciences*, 7(12):1463–1468, 2008.

[66] Laila Abu-Sen, John J Morrison, Andrew B Horn, and Stephen G Yeates. Concentration-and solvent-dependent photochemical instability of 6, 13-bis (triisopropysilylethynyl) pentacene. *Advanced Optical Materials*, 2(7):636–640, 2014.

[67] A Ravikumar Reddy and Michael Bendikov. Diels–alder reaction of acenes with singlet and triplet oxygen–theoretical study of two-state reactivity. *Chemical communications*, (11):1179–1181, 2006.

[68] Werner Fudickar and Torsten Linker. Reversible photooxygenation of alkynylanthracenes: chemical generation of singlet oxygen under very mild conditions. *Chemistry–A European Journal*, 17(49):13661–13664, 2011.

[69] Tsugunosuke Masubuchi, Yoshito Sugawara, and Atsushi Nakajima. Adiabatic electron affinity of pentacene and perfluoropentacene molecules studied by anion photoelectron spectroscopy: Molecular insights into electronic properties. *The Journal of Chemical Physics*, 145(24):244306, 2016.

[70] Jonathan Day, Andrew D. Platt, Oksana Ostroverkhova, Sankar Subramanian, and John E. Anthony. Organic semiconductor composites: Influence of additives on the transient photocurrent. *Applied Physics Letters*, 94(1), 2009.

[71] Laura A Deschenes and David A Vanden Bout. Single molecule photobleaching: increasing photon yield and survival time through suppression of two-step photolysis. *Chemical physics letters*, 365(5):387–395, 2002.

[72] FG Patterson, HWH Lee, William L Wilson, and MD Fayer. Intersystem crossing from singlet states of molecular dimers and monomers in mixed molecular crystals: picosecond stimulated photon echo experiments. *Chemical physics*, 84(1):51–60, 1984.

[73] Hubert Piwonski, Adam Sokołowski, and Jacek Waluk. In search for the best environment for single molecule studies: Photostability of single terrylenediimide molecules in various polymer matrices. *Journal of Physical Chemistry Letters*, 6(13):2477–2482, 2015.

[74] Santi Nonell and Cristina Flors. *Singlet Oxygen: Applications in Biosciences and Nanosciences Volume 1*. Royal Society of Chemistry, 2016.

[75] Alexander P Darmanyan, William S Jenks, and Pierre Jardon. Charge-transfer quenching of singlet oxygen o2 (1δg) by amines and aromatic hydrocarbons. *The Journal of Physical Chemistry A*, 102(38):7420–7426, 1998.

[76] John E. Anthony. Functionalized acenes and heteroacenes for organic electronics. *Chemical Reviews*, 106(12):5028–5048, 2006. PMID: 17165682.

[77] DJ Gundlach, JE Royer, SK Park, S Subramanian, OD Jurchescu, BH Hamadani, AJ Moad, RJ Kline, LC Teague, O Kirillov, et al. Contact-induced crystallinity for high-performance soluble acene-based transistors and circuits. *Nature Materials*, 7(3):216–221, 2008.

[78] John E. Anthony. Small-molecule, nonfullerene acceptors for polymer bulk heterojunction organic photovoltaics. *Chemistry of Materials*, 23(3):583–590, 2011.

[79] K. R. Rajesh, K. Paudel, B. Johnson, R. Hallani, J. E. Anthony, and O. Ostroverkhova. Design of organic ternary blends and small-molecule bulk heterojunctions: photophysical considerations. *Journal of Photonics and Energy*, 5:057208, 2015.

[80] R. Giridharagopal and D.S. Ginger. Characterizing morphology in bulk heterojunction organic photovoltaic systems. *Journal of Physical Chemistry Letters*, 1(7):1160–1169, 2010.

[81] Whitney E. B. Shepherd, Andrew D. Platt, David Hofer, Oksana Ostroverkhova, Marsha Loth, and John E. Anthony. Aggregate formation and its effect on (opto)electronic properties of guest-host organic semiconductors. *Applied Physics Letters*, 97(16), 2010.

[82] W. E. B. Shepherd, A. D. Platt, M. Loth, J. E. Anthony, and O. Ostroverkhova. Optical, photoluminescent, and photoconductive properties of functionalized anthradithiophene and benzothiophene derivatives. *Proc. of SPIE*, 7599:75990R, 2010.

[83] P. Gao, D. Beckmann, H. N. Tsao, X. Feng, V. Enkelmann, M. Baumgarten, W. Pisula, and K. Mullen. Dithieno[2,3-d;2',3'-d']benzo[1,2-b;4,5-b']dithiophene (dtbdt) as semiconductor for high-performance, solution-processed organic field-effect transistors. *Advanced Materials*, 21:213–216, 2009.

[84] A. Y. Amin, K. Reuter, T. Meyer-Friedrichsen, and M. Halik. Interface engineering in high-performance low-voltage organic thin-film transistors based on 2,7-dialkyl-[1]benzothieno[3,2- b][1]benzothiophenes. *Langmuir*, 27:15340–15344, 2011.

[85] H. Minemawari, T. Yamada, H. Matsui, J. Tsutsumi, S. Haas, R. Chiba, R. Kumai, and T Hasegawa. Inkjet printing of single-crystal films. *Nature*, 475:364–367, 2011.

[86] A. D. Platt, M. J. Kendrick, M. Loth, J. E. Anthony, and O. Ostroverkhova. Temperature dependence of exciton and charge carrier dynamics in organic thin films. *Physical Review B*, 84, 2011.

[87] Katherine A. Willets. *Novel fluorophore systems for single-molecule imaging: photophysics, mechanism, and applications*. PhD thesis, Stanford University, 2005.

[88] M.A. Menese-Nava, O. Barbosa-Garcia, L.A. Diaz-Torres, S. Chavez-Cerda, M. Torres-Cisneros, and T.A. King. Effect of pmma impregnation on the fluorescence quantum yield of sol-gel glasses doped with quinine sulfate. *Optical Materials*, 17:415–418, 2001.

[89] Katherine A. Willets, Oksana Ostroverkhova, Meng He, Robert J. Twieg, and W. E. Moerner. Novel fluorophores for single-molecule imaging. *Journal of the American Chemical Society*, 125(5):1174–1175, 2003. PMID: 12553812.

[90] Pavol Hrdlovi, Jozef Krajovi, and Daniel Vgh. Spectral characteristics of bisthiophenes and terthiophenes linked with heterocyclic unit in solution and polymer matrix. *Journal of Photochemistry and Photobiology A: Chemistry*, 144(23):73 – 82, 2001.

[91] J. Schuster, F. Cichos, and C. von Borczyskowski. Blinking of single molecules in various environments. *Optics and Spectroscopy*, 98(5):712–717, 2005.

[92] R.J. Pfab, J. Zimmermann, C. Hettich, I. Gerhardt, A. Renn, and V. Sandoghdar. Aligned terrylene molecules in a spin-coated ultrathin crystalline film of p-terphenyl. *Chemical Physics Letters*, 387(46):490 – 495, 2004.

[93] Bernard Valeur and Mário Nuno Berberan-Santos. *Molecular Fluorescence: Principles and Applications*. Wiley-VCH, Weinheim, 2002.

[94] A. Nicolet, M. A. Kolchenko, B. Kozankiewicz, and M. Orrit. Intermolecular intersystem crossing in single-molecule spectroscopy: Terrylene in anthracene crystal. *The Journal of Chemical Physics*, 124(16):164711, 2006.

[95] O. Ostroverkhova, editor. *Handbook of organic materials for optical and (opto)electronic devices*. Woodhead Publishing, Cambridge, U.K., 2013.

[96] D. G. Grier. A revolution in optical manipulation. *Nature*, 424:810–816, 2003.

[97] K. Kegler, M. Salomo, and F. Kremer. Forces of interaction between dna-grafted colloids: An optical tweezer measurement. *Phys. Rev. Lett.*, 98:058304, Feb 2007.

[98] Carlos Bustamante, Zev Bryant, and Steven B. Smith. Ten years of tension: single-molecule dna mechanics. *Nature*, 421:423 – 427, 2003.

[99] Nils Calander and Magnus Willander. Optical trapping of single fluorescent molecules at the detection spots of nanoprobes. *Phys. Rev. Lett.*, 89:143603, Sep 2002.

[100] A Ashkin and JM Dziedzic. Optical trapping and manipulation of viruses and bacteria. *Science*, 235(4795):1517–1520, 1987.

[101] D. Evanko. Optimizing your optical tweezers. *Nature Methods*, 3:584–585, 2006.

[102] M. J. Kendrick, D. H. McIntyre, and O. Ostroverkhova. Wavelength dependence of optical tweezer trapping forces on dye-doped polystyrene microspheres. *J. Opt. Soc. Am. B*, 26(11):2189–2198, Nov 2009.

[103] John Taylor. *Introduction to error analysis, the study of uncertainties in physical measurements*. 1997.

[104] Sung Kyu Park, Devin A. Mourey, Sankar Subramanian, John E. Anthony, and Thomas N. Jackson. High-mobility spin-cast organic thin film transistors. *Applied Physics Letters*, 93(4), 2008.

[105] J. Day, A. D. Platt, S. Subramanian, J. E. Anthony, and O. Ostroverkhova. Influence of organic semiconductor-metal interfaces on the photoresponse of functionalized anthradithiophene thin films. *Journal of Applied Physics*, 105(10), 2009.

[106] R. Grollman, J. Busche, and O. Ostroverkhova. Optical tweezers-based probe of charge transfer in organic semiconductors at microscopic scales. *Proc. of SPIE*, 9360:936016, 2015.

[107] R. Grollman, K. Peters, and O. Ostroverkhova. Surface charge measurements and (dis)charging dynamics of organic semiconductors in various media using optical tweezers. *Proc. of SPIE*, 8983:89831N, 2014.

[108] Sven H. Behrens and David G. Grier. The charge of glass and silica surfaces. *The Journal of Chemical Physics*, 115(14), 2001.

[109] A. A. Kamel, C. M. Ma, M. S. El-Aasser, F. J. Micale, and J. W. Vanderhoff. Concerning the origin of charge at the polystyrene particle/water interface. *Dispersion Science and Technology*, 263:315–330, 1981.

[110] Logan S. McCarty, Adam Winkleman, and GeorgeM. Whitesides. Electrostatic self-assembly of polystyrene microspheres by using chemically directed contact electrification. *Angewandte Chemie International Edition*, 46(1-2):206–209, 2007.

[111] Norbert Garbow, Martin Evers, Thomas Palberg, and Tsuneo Okubo. On the electrophoretic mobility of isolated colloidal spheres. *Journal of Physics: Condensed Matter*, 16(23):3835, 2004.

[112] M. M. Elmahdy, C. Gutsche, and F. Kremer. Forces within single pairs of charged colloids in aqueous solutions of ionic liquids as studied by optical tweezers. *Journal of Physical Chemistry C*, 114:19452–19458, 2010.

[113] Sudam K. Parida, Sukalyan Dash, Sabita Patel, and B.K. Mishra. Adsorption of organic molecules on silica surface. *Advances in Colloid and Interface Science*, 121(13):77 – 110, 2006.

[114] Richard R. Lunt, Noel C. Giebink, Anna A. Belak, Jay B. Benziger, and Stephen R. Forrest. Exciton diffusion lengths of organic semiconductor thin films measured by spectrally resolved photoluminescence quenching. *Journal of Applied Physics*, 105(5), 2009.

APPENDIX

Chapter A Noise Elimination for Single Molecule Analysis

The following script was used to eliminate noise from time traces and sort fluorophores into the "blinker" or "non-blinker" category.

```
% onOffMake_blinkCounter_cut.m goes through all fluorophores and identifies blinking vs non
% blinking fluorophores. "Cut" ignores last on or off time of trace.
% v3 fixes problem with classifying "nonblinker." Originally, all 2 event
% traces were "nonblinkers." Now only on->off traces are "nonblinkers"

% Written by Rebecca Grollman
% June 30, 2016. Last modified 12/14/16.

% function [blinkersON, blinkersOFF, nonblinkersON, nonblinkersOFF, allON, allOFF, numB, numNB, blinkType] = onOffMaker_blinkCounter_cut(fileExtension, vidNum, sampleName)
```

```
10 function [blinkersON, blinkersOFF, nonblinkersON, numB,
       numNB, blinkType] = onOffMaker_blinkCounter_cut_v3(
       fileExtension, vidNum,sampleName)
11 % Be sure to verify funhistmake using correct frame to s
       conversion.
12
13 % Find all ON, OFF times for all fluorophores. Taken from
       archtauGRAND - allON(OFF) same as histFileON(OFF).
14 allON = [];
15 allOFF = [];
16
17 blinkersON = [];
18 blinkersOFF = [];
19
20 nonblinkersON = [];
21 nonblinkersOFF = [];
22
23 badTrace = [];
24
25 countNB = 0;
26 countB = 0;
27
28 traceNB = [];
```

```
29 traceB = [];
30
31 blinkType = zeros(2,10); % First row starts off, second row
       starts on. Each column represents number of events
     starting with 2 in column 1
32
33 for a = 1:vidNum
34     a
35     fileToRead = [fileExtension,int2str(a),'.mat'];
36     load(fileToRead)
37     [ON,OFF] = funhistmake_cut(HMFf,OnOfff,NumberofFrames);
38     allON(length(allON)+1:length(allON)+length(ON),1) = ON
         (:,1);
39     allOFF(length(allOFF)+1:length(allOFF)+length(OFF),1) =
         OFF(:,1);
40
41     for L = 1:FLUf
42         field = ['chart',int2str(L)];
43         trace = OnOfff.(field);
44
45         % Obvious nonblinker
46         if length(trace) == 2 && trace(1,2) == 1 % must be
             nonblinker
```

```
47              countNB = countNB + 1;
48              fieldNB = ['chart',int2str(countNB)];
49              traceNB.(fieldNB) = OnOfff.(field);
50              blinkType(trace(1,2) + 1, 1) = blinkType(trace
                    (1,2) + 1, 1) + 1;
51          % Type not obvious
52          else
53              c = 0; % placeholder for new trace
54              if sum(trace(:,1) > 570) == 1 % if only one
                    short event happens
55                  sortCheck = sort(trace(:,1));
56                  frameMin = sortCheck(end-1);
57              elseif length(trace) < 20 && length(trace(:,1))
                    > 1 % test if blinker or nonblinker with
                    less than 20 events (less noisy)
58                  frameMin = 20; % 20 is default
59              else % if number of events more than 20, more
                    noisy
60                  frameMin = 30; % 30 is default
61              end
62              for b = length(trace):-1:1
63  %                   if length(trace) == 2 % must be off->on
    trace
```

```
64 %                        b
65                  if trace(b,1) >= frameMin % finds all
                       events longer than frameMin. For events
                       less than frameMin, gets combines with
                       later event
66                      c = c + 1;
67                      traceNew(c,:) = trace(b,:);
68                  elseif b == length(trace) % if the event
                       last event very short
69                      traceNew = -1;
70                      break
71                  else % if event less than frameMin, adds
                       frame length to previous frame
72                      traceNew(c,1) = traceNew(c,1) + trace(b
                           ,1);
73                  end
74              end
75              if traceNew == -1 % For case where last few
                   events are short - makes trace end on a long
                    frame
76                  traceNew = [];
77                  longFrame = find(trace(:,1)>frameMin);
```

```
78              trace(longFrame(end),1) = sum(trace(
                    longFrame(end):length(trace),1));
79              trace(longFrame(end)+1:end,:) = [];
80              for b = length(trace):-1:1 % now goes
                    through same as above now that trace
                    modified
81                  if trace(b,1) >= frameMin % finds all
                        events longer than frameMin. For
                        events less than frameMin, gets
                        combines with later event
82                      c = c + 1;
83                      traceNew(c,:) = trace(b,:);
84                  else
85                      traceNew(c,1) = traceNew(c,1) +
                            trace(b,1);
86                  end
87              end
88          end
89
90          % for traces where on/off times condensed. Now
                some have neighboring on-on or off-off times
91          traceN = flip(traceNew); % Now events are in
                the correct order!
```

```
92          traceNew = [];
93
94          b = 1; % placeholder for stepping through
                OnOffNew
95          if b == length(traceN(:,1)) % if only one on or
                off time >20 or 30 frames respectively
96              badTrace = [badTrace; a, L]     % keep trace
                    of "bad" traces where a = vidNum, L =
                   Fl.
97              OnOffNew = -1;
98          else
99              OnOffNew = traceN;
100             while b <= length(OnOffNew(:,1))
101                 if b == length(OnOffNew(:,1))
102                     break
103                 elseif OnOffNew(b,2) == OnOffNew(b+1,2)
104                     OnOffNew(b,1) = OnOffNew(b,1) +
                            OnOffNew(b+1,1);
105                     OnOffNew(b+1,:) = [];
106                 else
107                     b = b + 1;
108                 end
109             end
```

```
110             end
111             traceN = [];
112
113
114             fieldSave = ['Vid',int2str(a),'Fl',int2str(L)];
115             traceSave.(fieldSave) = OnOffNew;
116
117             % With new trace, test if blinker or nonblinker
                    .
118             if OnOffNew == -1 % skip badTrace fluorophores
119             elseif length(OnOffNew) == 2 && OnOffNew(1,2)
                   == 1 % must be nonblinker
120                 countNB = countNB + 1;
121                 fieldNB = ['chart',int2str(countNB)];
122                 traceNB.(fieldNB) = OnOffNew;
123                 blinkType(OnOffNew(1,2) + 1, 1) = blinkType
                        (OnOffNew(1,2) + 1, 1) + 1;
124             else % must be blinker
125                 countB = countB + 1;
126                 fieldB = ['chart',int2str(countB)];
127                 traceB.(fieldB) = OnOffNew;
128                 blinkType(OnOffNew(1,2)+1,length(OnOffNew)
                        -1) = blinkType(OnOffNew(1,2)+1,length(
```

```
                    OnOffNew)-1) + 1;
129                 end
130             end
131             OnOffNew = [];
132         end
133 end
134
135 % Count number of nonblinkers and blinkers.
136 numNB = countNB;
137 numB = countB;
138
139 % Find On and Off times of nonblinkers and blinkers.
140 if isempty(traceNB) == 1
141 else
142         [ON,OFF] = funhistmake_cut(length(fieldnames(traceNB)),
                traceNB,NumberofFrames);
143         nonblinkersON(length(nonblinkersON)+1:length(
                nonblinkersON)+length(ON),1) = ON(:,1);
144         nonblinkersOFF(length(nonblinkersOFF)+1:length(
                nonblinkersOFF)+length(OFF),1) = OFF(:,1);
145 end
146
147 if isempty(traceB) == 1
```

```
148 else
149     [ON,OFF] = funhistmake_cut(length(fieldnames(traceB)),
            traceB,NumberofFrames);
150     blinkersON(length(blinkersON)+1:length(blinkersON)+
            length(ON),1) = ON(:,1);
151     blinkersOFF(length(blinkersOFF)+1:length(blinkersOFF)+
            length(OFF),1) = OFF(:,1);
152 end
153
154 % save(['onOffCut_', sampleName],'blinkersON', 'blinkersOFF
      ', 'nonblinkersON', 'nonblinkersOFF', 'allON', 'allOFF',
      'numB', 'numNB','traceSave');
155
156 end
```

Chapter B FRET Calculations

B.1 Calculation

The FRET radius R_0 can be calculated with

$$R_0^6 = \frac{9ln(10)}{128\pi^5 N_A}\frac{\kappa^2\Phi_{pl}}{n^4}J, \tag{B.1}$$

where N_A is Avogadro's number, κ is the dipole orientation factor (and for fixed, randomly oriented dipoles, $\kappa = 0.845\sqrt{2/3}$[114]), Φ_{pl} is the PL quantum yield of the donor, n is the index of refraction of the host matrix (ie n of PMMA or BTBTB), and the J is the overlap integral where

$$J = \int_0^\infty F_d(\lambda)\epsilon_a(\lambda)\lambda^4\,\mathrm{d}x. \tag{B.2}$$

To calculate J, the normalized fluorescence spectra of the donor $F_d(\lambda)$ (ie $\int F_d(\lambda), \mathrm{d}\lambda = 1$) and extinction coefficient of the acceptor $\epsilon_a(\lambda)$ are needed. The extinction coefficient of the acceptor as a function of wavelength can be found if the extinction coefficient at the peak of the absorption spectrum is known where

$$\epsilon_a(\lambda) = \frac{abs(\lambda)}{OD_{max}}\epsilon_{a,max}. \tag{B.3}$$

and $OD_{max} = 1$ and $abs(\lambda)$ is the normalized absorption spectrum.

B.2 Example Calculation: FRET radius between Pn-TCHS-F8 and IF-TIPS in PMMA

The following is a MATLAB script I wrote to calculate any FRET radius:

```
% FRETradiusIF.m
% May 5, 2015 by Rebecca Grollman
% modified Feb 2, 2016 by Rebecca Grollman for IF-TIPS/Pn-TCHS-F8
% Calculate FRET radius based on PL of donor, donor emission, acceptor
% extinction coeff, index of refraction of host

function  r0 = FRETradiusIF

% Import files and extract needed info (ie transmission from 380 to 850 nm)

```

```
11 load('IF_absorption.mat')
12 load('Pn_TCHS_F8_March212015_PL.mat')
13
14 % Keep from 501 to 900 nm and normalize.
15 spectPL = Pn_TCHS_F8_560dclp_537lp_sig(351:1522,:);
16 maxPL = max(spectPL(:,2));
17 minPL = min(spectPL(:,2));
18 normPL(:,2) = (spectPL(:,2) - minPL)./(maxPL-minPL);
19 normPL(:,1) = spectPL(:,1);
20
21 % Keep from 501 to 634 nm
22 spectAbs = IF_absorption(160:541,:);
23
24 % Check abs and PL spectra
25 hold on
26 plot(normPL(:,1),normPL(:,2))
27 plot(spectAbs(:,1),spectAbs(:,2))
28
29 % Normalize integral of PL to 1
30 interpArea = trapz(normPL(:,1),normPL(:,2));
31 normPL(:,2) = normPL(:,2)./interpArea;
32 normCheck = trapz(normPL(:,1),normPL(:,2))
33
```

```
34 % Trim PL from 500 to 634 nm
35 normPL = normPL(1:371,:);
36
37 % Interpolate PL spectra
38
39 %PLinterp(:,1) = interp(normPL(:,1),19);
40 %PLinterp(:,2) = interp(normPL(:,2),19);
41
42 % Normalize integral of PL to 1
43 PLinterp=normPL;
44 %interpArea = trapz(PLinterp(:,1),PLinterp(:,2))
45 %PLinterp(:,2) = PLinterp(:,2)./interpArea;
46 %normCheck = trapz(PLinterp(:,1),PLinterp(:,2))
47
48 % Interpolate abs spectra
49 %absinterp(:,1) = interp(spectAbs(:,1),11);
50 %absinterp(:,2) = interp(spectAbs(:,2),11);
51 absinterp=spectAbs;
52
53 % Trim absInterp to match lengths with PLinterp
54 absinterp = absinterp(6:376,:);
55
56 %Calculate extinction coefficient
```

```
57 epsilon = 10^(4.7) % M^-1 cm^-1?? Haley, Angew Chem, 2011
58 extCoeff = absinterp.*(epsilon);    % M^-1 cm^-1
59 %plot(absinterp(:,1),extCoeff(:,2))
60 extCoeff = extCoeff.*(100*10^-9).*10^24; % Convert to nm^3/
       mol nm^-1 (L to nm^3!! from mol/L = M)
61
62 % Compare interpolate job
63 plot(PLinterp(:,1),PLinterp(:,2))
64 plot(absinterp(:,1),absinterp(:,2))
65 plot(PLinterp(:,1),absinterp(:,2))
66 %plot(absinterp(:,1),PLinterp(:,2))
67
68 % Calculate J integral
69 J = trapz(PLinterp(:,1),PLinterp(:,2).*extCoeff(:,2).*
       PLinterp(:,1).^4)
70
71 % Calculate r0
72 PLQY_D = 0.82;
73 n_host = 1.49;
74 r0_const = 9*log(10)*0.845*sqrt(2/3)/(128*pi^5*6.022*10^23)
75 r0_6 = r0_const*PLQY_D*J/(n_host^4)
76 r0 = (r0_6)^(1/6)
77 end
```

Chapter C MATLAB Scripts for Charge Analysis with Optical Tweezers

The following two MATLAB scripts were used for all surface charge calculations using optical tweezers. The first script (ZeffCalcMultFolderv3.m) calls upon the second script (ZeffCalcforMFv3.m) when calculating surface charge from one set of data (within one folder).

```
% Rebecca Grollman
% December 3, 2013
% Optical Tweezers - Program to run through called upon folders to
% calculate Z and Z trim using ZeffCalc (Roberts method). Use .csv file for
% inputing parameters for each run.

function [ZeffTable,ZeffIndivTable,freq] = ZeffCalcMultFolderv3(minFolder,maxFolder,Date,numDataRuns)
%function [ZeffTable,freq,m,n] = ZeffCalcMultFolder(minFolder,maxFolder,Date,numDataRuns)
```

```
9  %minFolder = starting folder, ex: '00', '10', etc
10 %maxFolder = last folder, ex: '96', '12', etc
11 %Date = 'Dec012013'
12 %numDataRuns = typically 3 or 4. Number of runs per data
       set.
13
14 ZeffTable = zeros(str2num(maxFolder)-str2num(minFolder),9);
15
16 inputTable = csvread('Data Run Summary 2.csv');
17 % Column 1 = Sphere number
18 % Column 2 = Run number
19 % Column 3 = f sampling (kHz)
20 % Column 4 = f chopper (Hz)
21 % Column 5 = fac (Hz)
22 % Column 6 = Applied voltage on FG (Vpp), low gain
23 % Column 7 = offset (mV)
24
25 sphereTable = csvread('Sphere.csv');
26 % Column 1 = sphere number
27 % Column 2 = Depth (um)
28 % Column 3 = Position (um)
29 % Column 4 = IR Power (mW)
30 % Column 5 = Verdi Power (mW)
```

```
% Column 6 = d (um) distance between electrodes

% Get files from run directories - outputx, Fdata

r = 1;

for p = str2num(minFolder):str2num(maxFolder)

    sphereNum = inputTable(p+1,1);
    d = sphereTable(sphereNum,6);
    Vpp = inputTable(p+1,6);

    fac = inputTable(p+1,5);

    runNum = p;
    if runNum < 10
        runNum = strcat('0',num2str(runNum));
    else
        runNum = num2str(runNum);
    end

    % Extract data from MATLAB trap stiffness script
    cd(['Z:\Optical_Tweezers\Data\',Date,'\',runNum])
```

```
54      load(['output-',runNum,'.mat'])
55      cd ..
56
57      Fdata = [Fdataf,Fdata];
58
59      [PacAvg,PacTrimAvg,Zeff,ZeffTrim,ZeffIndiv,
            ZeffTrimIndiv,gamma,gammaTrim,gammaAvg,gammaTrimAvg,
            E,fac,ZeffEp,ZeffTrimEp,ZeffEpIndiv,ZeffTrimEpIndiv,
            EEp,freq,expData] = ZeffCalcforMFv3(numDataRuns,
            runNum,d,Vpp,fac,output,Fdata);
60
61
62      ZeffTable(r,1) = str2num(runNum);
63      ZeffTable(r,2) = PacAvg;
64      ZeffTable(r,3) = PacTrimAvg;
65      ZeffTable(r,4) = gammaAvg;
66      ZeffTable(r,5) = gammaTrimAvg;
67      ZeffTable(r,6) = Zeff;
68      ZeffTable(r,7) = ZeffTrim;
69      ZeffTable(r,8) = E;
70      ZeffTable(r,9) = ZeffEp;
71      ZeffTable(r,10) = ZeffTrimEp;
72      ZeffTable(r,11) = EEp;
```

```
73      ZeffTable(r,12) = fac;
74
75      numColStart = (r-1).*(numDataRuns + 2)+1;
76      numColEnd = r.*(numDataRuns + 2);
77      ZeffIndivTable(numColStart:numColEnd,1) = str2num(
            runNum);
78      ZeffIndivTable(numColStart:numColEnd,2) = gamma;
79      ZeffIndivTable(numColStart:numColEnd,3) = gammaTrim;
80      ZeffIndivTable(numColStart:numColEnd,4) = ZeffIndiv;
81      ZeffIndivTable(numColStart:numColEnd,5) = ZeffTrimIndiv
            ;
82      ZeffIndivTable(numColStart:numColEnd,6) = ZeffEpIndiv;
83      ZeffIndivTable(numColStart:numColEnd,7) =
            ZeffTrimEpIndiv;
84
85      r = r + 1;
86
87      clear outputx
88      clear Fdata
89  end
```

```
1  % Rebecca Grollman
2  % April 26, 2013
```

```
3 % Optical Tweezers - Program to calculate effective charge
      on sphere from
4 % data runs.
5
6 function [PacAvg,PacTrimAvg,Zeff,ZeffTrim,ZeffIndiv,
      ZeffTrimIndiv,gamma,gammaTrim,gammaAvg,gammaTrimAvg,E,
      fac,ZeffEp,ZeffTrimEp,ZeffEpIndiv,ZeffTrimEpIndiv,EEp,
      freq,expData] = ZeffCalcforMFv3(numDataRuns,RunNum,d,Vpp
      ,fac,outputx,Fdata)
7 % numDataRuns = number of runs, usually 4
8 % RunNum = run number, ex: '01', '02', '03', ...
9 % d = distance between electrodes (um)
10 % Voltage = V peak to peak (V) if on low gain for amp and
      read on function
11 % generator
12 % fac = frequency of driving force (Hz)
13
14 %% All k values and fitting parameters
15 %  outputx = dlmread(strcat('outputx-',RunNum,'.txt'));
16  f0all = outputx(:,4);
17  Sall = outputx(:,3)*(10^(-9))^2; % convert from nm^2/Hz to
       m^2/Hz
18
```

```
19  beta = 1*10^(-3); % visc for water
20  epsilon = 80; % dielectric constant for water
21  kT = 295*1.38*10^(-23); %k_BT
22  e = 1.6*10^(-19); % C
23
24 % Calculate fit data
25 for i=1:numDataRuns
26     S = Sall(i);
27     f0 = f0all(i);
28     freq = Fdata(:,1);
29     fitData(:,i) = (S.*f0.^2)./((freq.^2)+(f0.^2));
30 end
31
32 % Extract experimental data and (Experimental - Fit data)
33 for i=1:numDataRuns
34     FdataCell = Fdata(:,i+1);
35     expData(:,i) = (10^-9)^2.*Fdata(:,i+1);
36     newData(:,i) = expData(:,i) - fitData(:,i);
37 end
38
39 %Find frequency limits for PacTrim
40   minfreq = floor((32768*fac + 39375)/80000);
41   maxfreq = ceil((32768*fac + 39375)/80000);
```

```
42    m = minfreq-2       % normally -2 and +2
43    n = maxfreq+2

44
45  % Integrate newData to get Pac
46  for i=1:numDataRuns
47      Pac(i) = trapz(freq(:),newData(:,i));
48      PacTrim(i) = trapz(freq(m:n),newData(m:n,i));
49  end

50
51  % k values for all data runs
52  for i=1:numDataRuns
53      k_x(i) = mean(outputx(i,6))*10^(-6);
54      k_h(i) = mean(outputx(i,7))*10^(-6);
55      k_s(i) = mean(outputx(i,8))*10^(-6);
56      k_w(i) = mean(outputx(i,9))*10^(-6);
57  end

58
59  % Average k values (converted to N/m) and Pac

60
61      k_xAvg = mean(outputx(:,6))*10^(-6);
62      k_hAvg = mean(outputx(:,7))*10^(-6);
63      k_sAvg = mean(outputx(:,8))*10^(-6);
64      k_wAvg = mean(outputx(:,9))*10^(-6);
```

```
65        PacAvg = mean(Pac(:));
66        PacTrimAvg = mean(PacTrim(:));
67
68  % Plot PSDs from above
69  loglog(freq(:),expData(:,1).*10^18,freq(:),fitData(:,1)
        .*10^18,freq(:),newData(:,1).*10^18)
70
71  legend('experimental','fit','exp-fit')
72  xlabel('Frequency (Hz)')
73  ylabel('PSD (nm^2/Hz)')
74
75  % Calculate Z with Mark's method with average Pac and k
        values
76  a = .5*10^(-6);
77  V = Vpp/2;    % *5 if amplifier on low gain and Vpp read
        from FG
78  EEp = (V)/(epsilon*d*10^(-6)); % V/m
79  E = (V)/(d*10^(-6)); % V/m
80  gammaAvg = sqrt(PacAvg*k_sAvg/kT);
81  gammaTrimAvg = sqrt(PacTrimAvg*k_sAvg/kT);
82  ksi = 6*pi*beta*a;
83
84  Zeff = (ksi*gammaAvg/E)*sqrt(2*kT*((2*pi*fac)^2+(2*pi*mean(
```

```
    f0(:)))^2)/k_sAvg)/e;
85  ZeffTrim = (ksi*gammaTrimAvg/E)*sqrt(2*kT*((2*pi*fac)^2+(2*
    pi*mean(f0(:)))^2)/k_sAvg)/e;
86
87  ZeffEp = (ksi*gammaAvg/EEp)*sqrt(2*kT*((2*pi*fac)^2+(2*pi*
    mean(f0(:)))^2)/k_sAvg)/e;
88  ZeffTrimEp = (ksi*gammaTrimAvg/EEp)*sqrt(2*kT*((2*pi*fac)
    ^2+(2*pi*mean(f0(:)))^2)/k_sAvg)/e;
89
90  % Calculate Z with Mark's method for each individual run
    per data set.
91  % NOTE: a, V, EEp, E, ksi all same from above.
92  for i=1:numDataRuns
93      gamma(i) = sqrt(Pac(i)*k_s(i)/kT);
94      gammaTrim(i) = sqrt(PacTrim(i)*k_s(i)/kT);
95
96      ZeffIndiv(i) = (ksi*gamma(i)/E)*sqrt(2*kT*((2*pi*fac)
        ^2+(2*pi*f0all(i))^2)/k_s(i))/e;
97      ZeffTrimIndiv(i) = (ksi*gammaTrim(i)/E)*sqrt(2*kT*((2*
        pi*fac)^2+(2*pi*f0all(i))^2)/k_s(i))/e;
98
99      ZeffEpIndiv(i) = (ksi*gamma(i)/EEp)*sqrt(2*kT*((2*pi*
        fac)^2+(2*pi*f0all(i))^2)/k_s(i))/e;
```

```
100         ZeffTrimEpIndiv(i) = (ksi*gammaTrim(i)/EEp)*sqrt(2*kT
                *((2*pi*fac)^2+(2*pi*f0all(i))^2)/k_s(i))/e;
101     end
102
103     % Put averages of Zeffs at end of individual columns.
104     colNum = numDataRuns + 1;
105     gamma(colNum) = gammaAvg;
106     gammaTrim(colNum) = gammaTrimAvg;
107     ZeffIndiv(colNum) = Zeff;
108     ZeffTrimIndiv(colNum) = ZeffTrim;
109     ZeffEpIndiv(colNum) = ZeffEp;
110     ZeffTrimEpIndiv(colNum) = ZeffTrimEp;
111
112     % Put std deviations at end of individual columns.
113     colNum = colNum + 1;
114     gamma(colNum) = std(gamma(1:numDataRuns));
115     gammaTrim(colNum) = std(gammaTrim(1:numDataRuns));
116     ZeffIndiv(colNum) = std(ZeffIndiv(1:numDataRuns));
117     ZeffTrimIndiv(colNum) = std(ZeffTrimIndiv(1:numDataRuns));
118     ZeffEpIndiv(colNum) = std(ZeffEpIndiv(1:numDataRuns));
119     ZeffTrimEpIndiv(colNum) = std(ZeffTrimEpIndiv(1:numDataRuns
            ));
120     end
```